N88-15130

THE OHIO STATE UNIVERSITY

Electromagnetic Fields Backscattered from an S-Shaped Inlet Cavity with an Absorber Coating on its Inner Walls

by

R.J. Burkholder
C.W. Chuang
P.H. Pathak

The Ohio State University

ElectroScience Laboratory

Department of Electrical Engineering
Columbus, Ohio 43212

Final Report No. 715723-2
Grant NAG 3-476
July 30, 1987

NASA – Lewis Research Center
21000 Brookpark Rd.
Cleveland, Ohio 44135

NOTICES

When Government drawings, specifications, or other data are used for any purpose other than in connection with a definitely related Government procurement operation, the United States Government thereby incurs no responsibility nor any obligation whatsoever, and the fact that the Government may have formulated, furnished, or in any way supplied the said drawings, specifications, or other data, is not to be regarded by implication or otherwise as in any manner licensing the holder or any other person or corporation, or conveying any rights or permission to manufacture, use, or sell any patented invention that may in any way be related thereto.

50272-101

REPORT DOCUMENTATION PAGE	1. REPORT NO.	2.	3. Recipient's Accession No.

4. Title and Subtitle

ELECTROMAGNETIC FIELDS BACKSCATTERED FROM AN S-SHAPED INLET CAVITY WITH AN ABSORBER COATING ON ITS INNER WALLS

5. Report Date July 1987

6.

7. Author(s)

R.J. Burkholder, C.W. Chuang, P.H. Pathak

8. Performing Organization Rept. No. 715723-2

9. Performing Organization Name and Address

The Ohio State University
ElectroScience Laboratory
1320 Kinnear Rd.
Columbus, OHio 43212

10. Project/Task/Work Unit No.

11. Contract(C) or Grant(G) No.

(C)

(G) NAG 3-476

12. Sponsoring Organization Name and Address

NASA/Lewis Research Center
21000 Brookpark Rd.
Cleveland, OHio 44135

13. Type of Report & Period Covered Final

14.

15. Supplementary Notes

16. Abstract (Limit: 200 words)

The EM backscatter from a two-dimensional S-shaped inlet cavity is analysed using three different techniques, namely a hybrid combination of asymptotic high frequency and modal methods, an integral equation method, and the geometrical optics ray method, respectively. This inlet has a thin absorber coating on its perfectly conducting inner walls and the planar interior termination is made perfectly conducting. The effect of the absorber on the inner wall is treated via a perturbation scheme in the hybrid approach where it is assumed that the loss is sufficiently small for the method to be valid. The results are compared with the backscatter from a straight inlet cavity to evaluate the effect of offsetting the termination in the S-bend configuration such that it is not visible from the open end of the inlet. The envelope of the backscatter pattern for the straight inlet is always seen to peak around the forward axis due to the large return from the directly visible termination, and the pattern envelope tapers off away from the forward axis. Offsetting the termination causes the envelope of the backscatter pattern to flatten out, thereby reducing the return near the forward axis by several dB. The absorber coating reduces the pattern level of the straight inlet in directions away from the forward axis but has little effect on the peak near the axis, furthermore, the absorber coating is seen to consistently reduce the backscatter from the S-bend inlet for almost all incidence angles. It is observed that the hybrid method gives excellent agreement with experimental data and with the integral equation solution, whereas, the geometrical optics ray tracing method is able to generally predict the average of the backscatter pattern but not the pattern details.

17. Document Analysis a. Descriptors

b. Identifiers/Open-Ended Terms

c. COSATI Field/Group

18. Availability Statement	19. Security Class (This Report) Unclassified	21. No. of Pages 128
	20. Security Class (This Page) Unclassified	22. Price

(See ANSI-Z39.18) See Instructions on Reverse OPTIONAL FORM 272 (4-77) (Formerly NTIS-35) Department of Commerce

Contents

List of Figures

1. Introduction

This report describes an analysis of the electromagnetic (EM) fields which are backscattered from a two dimensional S-shaped inlet cavity. Figure 1.1 shows the geometry of this problem along with all the variable parameters. The interior walls of the S-shaped cavity are perfectly conducting with a thin absorber coating. The planar interior termination is made perfectly conducting. The S-shaped inlet is assumed here to be modeled by joining appropriate sections of parallel plate waveguides and uniform annular waveguides as is evident from Figure 1.1.

The two basic scattering mechanisms of the inlet cavity of Figure 1.1 are the scattering from just the edges at the open end, and the scattering from the interior termination within the inlet cavity. A plane wave is assumed to be incident on the inlet at some aspect angle (θ) and encounters the edges at the open end of the inlet. The two leading edges thus scatter part of this incident energy by diffraction at those edges to give the direct contribution from the opening by itself. The scattering from the interior cavity region is due to the incident energy which couples into the natural modes of the piecewise uniform waveguide sections of the S-shaped inlet, and propagates to the end termination to be then reflected back into the aperture at the open end from which it radiates into the exterior region. In addition to these primary scattering mechanisms, there are higher order effects which need to be considered. These include the small reflections due to the discontinuities at junctions between sections, the slightly larger internal reflection of the energy by the aperture, and the multiple wave interactions between all these scattering centers.

Chapters 2 and 3 describe an efficient hybrid combination of asymptotic high frequency (HF) methods with the modal technique that is used to analyze the scattering from a perfectly conducting inlet [1,10]. The fields in the guide are expanded into the natural waveguide modes of each uniform section. The relative strengths of these modes are represented with coefficients which can be expressed

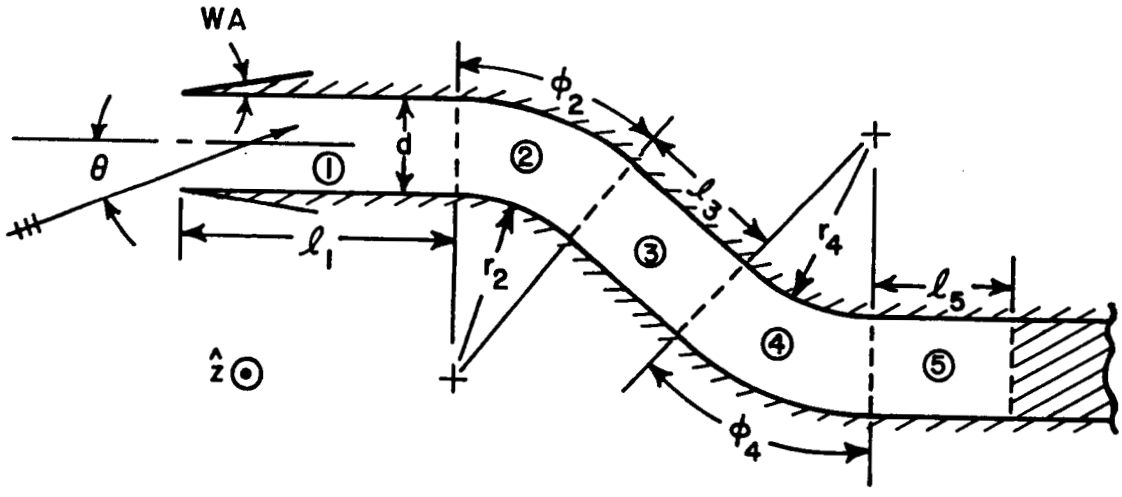

Figure 1.1: Geometry of the S-shaped inlet cavity.

in column matrix form. Reflection at a junction, transmission through a junction and propagation through a section are all represented as rectangular matrices which operate on the column matrices for the coefficients of the modes incident on the junction. The elements of these matrices are found using high frequency techniques such as the Kirchhoff approximation, the equivalent current approach, and modal ray-optics. The multiple interactions are accounted for using the self-consistent Multiple Scattering Matrix (MSM) formulation. The latter is essentially the same as the Generalized Scattering Matrix formulation [2].

Chapter 4 extends the method of chapters 2 and 3 to include inlets with thin absorber coatings on the inner walls using a small perturbation to the propagation constants of the waveguide sections. This method is limited to relatively small values of absorber thickness and loss.

Chapter 5 describes a numerical method of finding the modal reflection coefficient for the reflection from the first junction of the inlet geometry. Refering to Figure 1.1, this is the reflection of a waveguide mode of section 1 incident at the junction between sections 1 and 2. The method expands the fields in each waveguide section into modes and solves for the unknown coefficients by matching the fields at the junctions. It is not very efficient but it can handle arbitrary impedance boundary conditions on the waveguide walls. This solution is included to test the modal reflection obtained from the perturbational approach of Chapter 4.

Chapter 6 describes a purely ray-optical method of analyzing cavity scattering. The geometrical optics (GO) incident field which enters the inlet from the aperture is then tracked via rays through the inlet as they undergo multiple reflections from the inlet walls to reach the termination and then bounce back again to the aperture. An aperture integration (AI) is subsequently performed on this GO field scattered back into the aperture to obtain the exterior far field radiation from the aperture. The advantage of the GO/AI method is that it can handle arbitrary inlet geometries

other than inlets made up of uniform waveguide sections. Also, it can handle any type of absorbing wall material which can be characterized locally by plane wave reflection coefficients. However, this approach which ignores diffracted rays becomes less accurate for electrically small inlets and/or long inlets. It is included in this report mainly for comparison purposes and to supply an alternative analysis method. Also, this GO/AI technique, which ignores diffraction effects at the open end that also propagate into the inlet, is found to provide a reasonable estimate of the average of the backscattered field but not the details in the field pattern.

A few numerical examples along with some measurements are included in chapters 4, 5 and 6. Throughout the report an $e^{j\omega t}$ convention is assumed and suppressed. "TE" (Transverse Electric) means that the E-field is transverse to the direction of propagation, or equivalently, the E-field has only a component perpendicular to the plane of incidence. Similarly, "TM" (Transverse Magnetic) means the H-field is perpendicular to the plane of incidence. Here, the plane of incidence is defined by the incident ray and the axis of the first parallel plate waveguide section of the S-shaped inlet.

2. Self-Consistent Multiple Scattering Matrix Formulation

The inlet considered in this report is made up of interconnected piecewise sections of parallel plate waveguides and circularly curved or "annular" waveguides. The fields inside these guides can be expressed as an expansion of only the propagating ortho-normal waveguide modes. [1] Ortho-normal simply means that each mode is normalized to carry unit power and carries it independently of all the other modes in the guide. The modes themselves satisfy the wave equation and boundary conditions of the corresponding uniform guide which extends to infinity in both directions. For the annular guide, this would mean an infinitely extended angular space. To account for the finite lengths of the various guide sections and the multiple interactions between all the junctions and the open end, the Multiple Scattering Matrix (MSM) formulation is used [2].

A junction between two dissimilar waveguide sections can be characterized in terms of transmission and reflection matrices associated with the junction which relate the coefficients of the waveguide modes on either side of the junction. Figure 2.1 shows a typical junction between waveguide sections which are both semi-infinite (in this case, it is the junction between sections 1 and 2). Energy propagates down section 1 from the left and is incident on the junction. In general, a junction is formed by joining a p^{th} waveguide section with a q^{th} waveguide section. Thus, the sections p and q are physically connected together at the junction. Using the symbol U for the $\hat{z}$-directed E-field of the TE case and the H-field of the TM case, respectively, the incident, reflected and transmitted fields at any junction between the p^{th} and q^{th} waveguide sections can be expressed as

$$\vec{U}^{inc} = \sum_{n=1}^{N} A_n \hat{u}_n e^{-j\beta_n x} \tag{2.1}$$

[1] Since the separation between the junctions is sufficiently large, the evanescent modes are ignored as they contribute negligibly. It is noted that evanescent modes cannot be normalized the same way as is done here for the propagating modes.

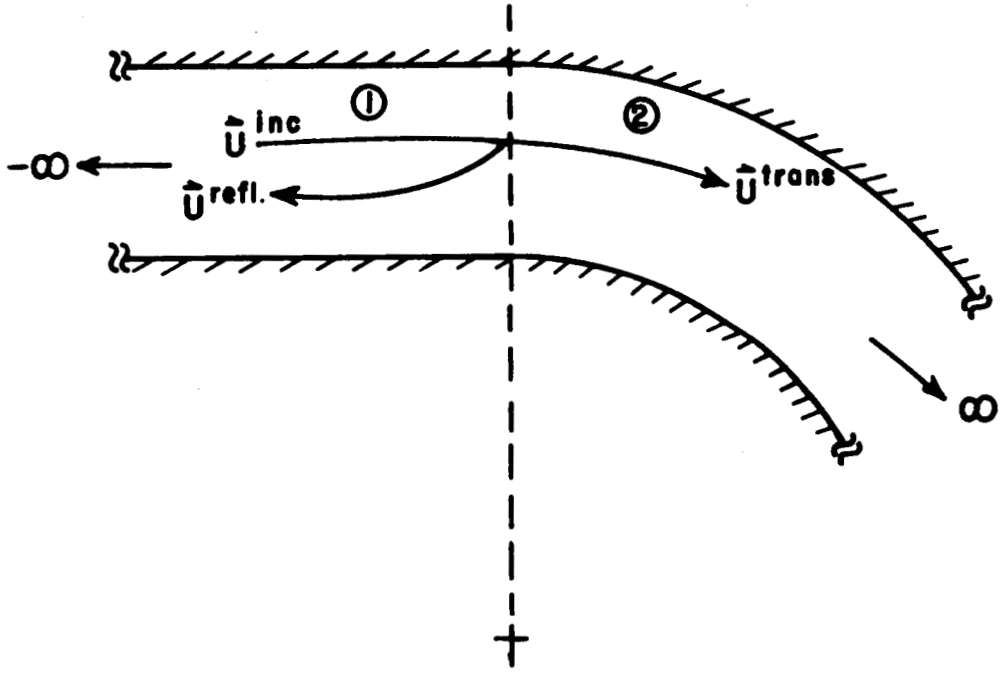

Figure 2.1: Junction between sections 1 and 2.

$$\vec{U}^{refl} = \sum_{n=1}^{N} B_n \hat{u}_n e^{j\beta_n x} \tag{2.2}$$

$$\vec{U}^{trans} = \sum_{m=1}^{M} C_m \hat{u}_m e^{j\nu_m \phi} \tag{2.3}$$

where $\hat{u}_n$ represents the n^{th} transverse ortho-normal modal field of section p at the junction and $\hat{u}_m$ likewise represents the m^{th} modal field of section q at the junction. The coefficients A_n, B_n, and C_m can be represented as column vectors

$$[A] = \begin{bmatrix} A_1 \\ \vdots \\ A_N \end{bmatrix} \tag{2.4}$$

$$[B] = \begin{bmatrix} B_1 \\ \vdots \\ B_N \end{bmatrix} \tag{2.5}$$

$$[C] = \begin{bmatrix} C_1 \\ \vdots \\ C_M \end{bmatrix}. \tag{2.6}$$

The reflection and transmission scattering matrices for this junction between the p^{th} and q^{th} waveguide sections are then defined by

$$[B] = [R_{pq}][A] \tag{2.7}$$

$$[C] = [T_{pq}][A] \tag{2.8}$$

$$[R_{pq}] = \begin{bmatrix} R_{pq}^{11} & R_{pq}^{12} & \cdots & R_{pq}^{1N} \\ R_{pq}^{21} & R_{pq}^{22} & \cdots & R_{pq}^{2N} \\ \vdots & \vdots & \ddots & \vdots \\ R_{pq}^{N1} & R_{pq}^{N2} & \cdots & R_{pq}^{NN} \end{bmatrix} \tag{2.9}$$

$$[T_{pq}] = \begin{bmatrix} T_{pq}^{11} & T_{pq}^{12} & \cdots & T_{pq}^{1N} \\ T_{pq}^{21} & T_{pq}^{22} & \cdots & T_{pq}^{2N} \\ \vdots & \vdots & \ddots & \vdots \\ T_{pq}^{M1} & T_{pq}^{M2} & \cdots & T_{pq}^{MN} \end{bmatrix} \tag{2.10}$$

Here, the reflection matrix is associated with the fields reflected back into the p^{th} section when it is joined directly to the q^{th} section. Likewise, the transmission matrix is associated with the fields transmitted into the q^{th} section when the fields

are incident from the adjoining p^{th} section. N and M are the number of propagating modes in the adjoining sections p and q, respectively. Notice that $[R_{pq}]$ is $N \times N$ and $[T_{pq}]$ is $M \times N$.

For the special case of the open end (the junction between waveguide section 1 and the exterior region) the scattering matrices have a slightly different form. For the coupling into the inlet and the scattering from the open end, the fields can be expressed similarly to equations (2.1), (2.2) and (2.3) as

$$\vec{U}^{inc} = \hat{z} U_{inc} e^{-jk(x\cos\theta + y\sin\theta)} \tag{2.11}$$

$$\vec{U}^{refl} = \hat{z} B \frac{e^{-jk\rho}}{\sqrt{\rho}} \tag{2.12}$$

$$\vec{U}^{trans} = \sum_{n=1}^{N} C_n \hat{u}_n e^{-jk\beta_n x} \tag{2.13}$$

where U^{inc} is a scalar representing the magnitude of the incident plane wave and ρ is the distance to the receiver referenced from the lower $(x, y = 0)$ edge. $\vec{U}^{refl}$ represents the field scattered back into the exterior by the edges at the open end, and $\vec{U}^{trans}$ represents the field coupled (or transmitted) into the inlet. B is a scalar for this case and $[C]$ is a column matrix as before. The reflection and transmission matrices can now be defined similarly to equations (2.7) and (2.8) as

$$B = R_{01} U^{inc} \tag{2.14}$$

$$[C] = [T_{01}] U^{inc} \tag{2.15}$$

where the subscript "0" refers to the exterior region. Notice that the reflection matrix has reduced to a scalar for this case and the transmission matrix has reduced to a column matrix (because [C] is a column matrix). The matrices describing the exterior radiation and the interior reflection from the open end when modal fields are incident from inside the guide are defined similarly as follows.

$$\vec{U}^{inc} = \sum_{n=1}^{N} A_n \hat{u}_n e^{jk\beta_n x} \tag{2.16}$$

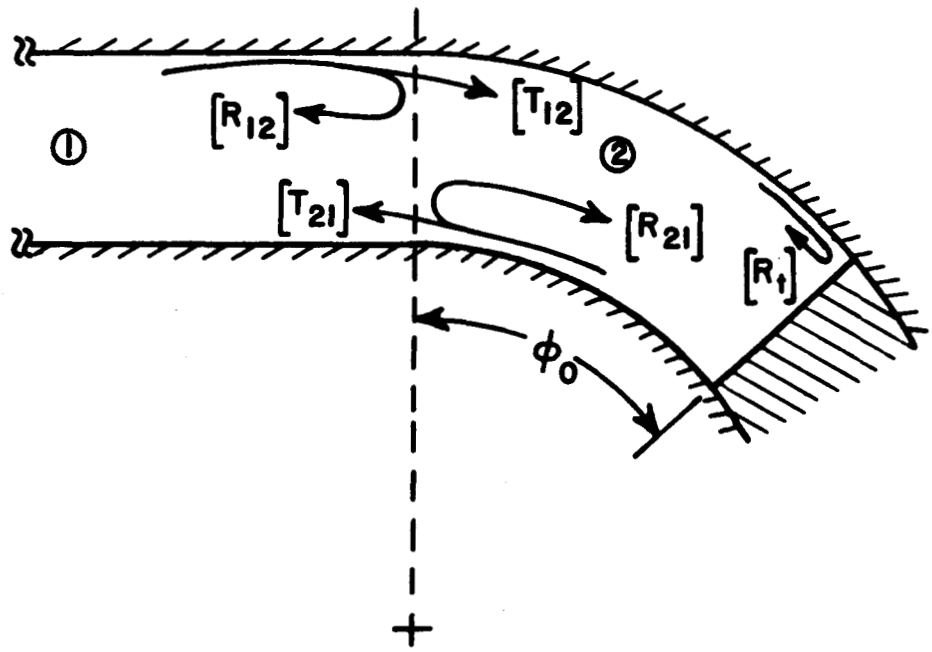

Figure 2.2: The junction of Figure 2.1 with a termination in section 2.

$$\vec{U}^{refl} = \sum_{n=1}^{N} B_n \hat{u}_n e^{-jk\beta_n x} \tag{2.17}$$

$$\vec{U}^{trans} = \hat{z} C \frac{e^{-jk\rho}}{\sqrt{\rho}} \tag{2.18}$$

$$[B] = [R_{10}][A] \tag{2.19}$$

$$C = [T_{10}][A]. \tag{2.20}$$

Notice that $[R_{10}]$ is a square matrix and $[T_{10}]$ is a row matrix (because C is a scalar).

To include the effects of more than one scattering junction, the Multiple Scattering Matrix (MSM) is used [2]. To illustrate its implimentation, consider the simple geometry of figure 2.1 with a termination placed in section 2 as shown in figure 2.2. The total reflection matrix $[R_{12}]$ in region 1 due to the junction between waveguide sections $p = 1$, $q = 2$, as well as the termination is given via the MSM for that

junction as

$$\left[R_{12}^{MSM}\right] = [R_{12}] + [T_{21}][P_2][R_t][P_2]\left([I] - [R_{21}][P_2][R_t][P_2]\right)^{-1}[T_{12}] \tag{2.21}$$

in which

$$[P_2] = \begin{bmatrix} e^{-j\nu_1\phi_0} & 0 & 0 \\ 0 & \ddots & 0 \\ 0 & 0 & e^{-j\nu_M\phi_0} \end{bmatrix} \tag{2.22}$$

where $[I]$ is an identity matrix, $[P_2]$ describes the propagation through section 2, and $[R_t]$ is a reflection matrix describing the termination. As an example, if the termination were a perfect electric conductor, for the TM case $[R_t]$ would equal $[I]$ and for the TE case $[R_t]$ would equal $-[I]$. The above result for $[R_{12}^{MSM}]$ accounts for all the multiple wave interactions between the junction and the termination.

To describe the multiple interactions of more than 2 scattering junctions (such as in the inlet of Figure 1.1), the MSM result of (2.21) is modified by simply replacing $[R_t]$ with the MSM of the next junction [1]. This is repeated until the final junction associated with the termination is reached. For the inlet under consideration (see Figure 1.1) there are four junctions formed by connecting five dissimilar waveguide sections, a termination, and the open end which amount to a total of six different scattering junctions. Modifiying the MSM to include all six junctions, the total scattered field can be expressed as follows.

$$\vec{U}^{scat} = \hat{z}R^{MSM}U^{inc}\frac{e^{-jk\rho}}{\sqrt{\rho}} \tag{2.23}$$

$$R^{MSM} = R_{01} + [T_{10}][P_1][R_{12}^{MSM}][P_1]\cdot \cdot\left([I] - [R_{10}][P_1][R_{12}^{MSM}][P_1]\right)^{-1}[T_{01}] \tag{2.24}$$

$$\left[R_{12}^{MSM}\right] = [R_{12}] + [T_{21}][P_2][R_{23}^{MSM}][P_2]\cdot \cdot\left([I] - [R_{21}][P_2][R_{23}^{MSM}][P_2]\right)^{-1}[T_{12}] \tag{2.25}$$

$$\left[R_{23}^{MSM}\right] = [R_{23}] + [T_{32}][P_3][R_{34}^{MSM}][P_3] \cdot \cdot \left([I] - [R_{32}][P_3][R_{34}^{MSM}][P_3]\right)^{-1} [T_{23}] \quad (2.26)$$

$$\left[R_{34}^{MSM}\right] = [R_{34}] + [T_{43}][P_4][R_{45}^{MSM}][P_4] \cdot \cdot \left([I] - [R_{43}][P_4][R_{45}^{MSM}][P_4]\right)^{-1} [T_{34}] \quad (2.27)$$

$$\left[R_{45}^{MSM}\right] = [R_{45}] + [T_{54}][P_5][R_t][P_5] \cdot \cdot ([I] - [R_{54}][P_5][R_t][P_5])^{-1} [T_{45}] \quad (2.28)$$

where the junction matrices are defined using the "*pq*" convention as before.

It is seen from symmetry considerations that some of the above matrices are equal. Also, as will be shown later, the transmission matrices at a junction are reciprical. Appendix D lists these relations. With these simplifications, only eight of the original eighteen reflection and transmission matrices need to be evaluated. They are $[R_{12}]$, $[R_{21}]$, $[R_{34}]$, $[R_{43}]$, $[R_{10}]$, $[R_t]$, $[T_{12}]$, and $[T_{54}]$. If the radii of curvature of the annular waveguide sections 2 and 4 are equal, i.e., if $r_2 = r_4$ then only $[R_{12}]$, $[R_{21}]$, $[R_{10}]$, $[R_t]$, and $[T_{12}]$ need to be evaluated.

3. Hybrid Asymptotic Modal Analysis for Determining the Elements of the Scattering Matrices

3.1 Modal Field Structure

To determine the elements of the scattering matrices, a knowledge of the modal fields of the two types of uniform waveguides must first be obtained. Figure 3.1 shows a parallel plate guide which extends to infinity in both directions. The total field propagating in the $\pm\hat{x}$-direction inside the parallel plate guide can be expressed as a summation of the orthonormal waveguide modes of the guide:

$$\vec{E}^{\pm}(x,y) = \sum_n A_n^{\pm} \hat{e}_n^{\pm}(y) e^{\mp j\beta_n x} \tag{3.1}$$

$$\vec{H}^{\pm}(x,y) = \sum_n A_n^{\pm} \hat{h}_n^{\pm}(y) e^{\mp j\beta_n x} \tag{3.2}$$

$$\beta_n = \sqrt{k^2 - (\frac{n\pi}{d})^2} \tag{3.3}$$

where the coefficient $A_n^{\pm}$ determines the relative strength of mode n. The orthonormal modes are normalized according to

$$\int_0^d \left[\hat{e}_n^{\pm}(y) \times \hat{h}_n^{\pm}(y)\right] \cdot (\pm\hat{x}) dy = 1.$$

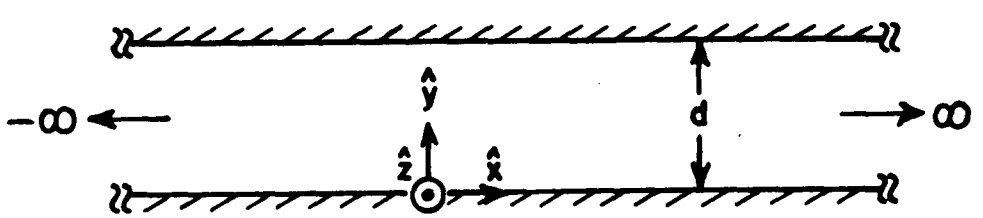

Figure 3.1: Parallel plate waveguide geometry.

In any waveguide there are an infinite number of modes. However, there is always a finite number of propagating modes, the rest being evanescent (they decay exponentially along the axis of the guide). The evanescent modes are ignored in this analysis as they contribute negligibly for the reasons explained in chapter 2. If only the propagating modes are included, the summation is truncated at $N = \text{int}(kd/\pi)$, the integer portion of kd/π. Notice that the number of propagating modes increases linearly with the width of the guide. Therefore, electrically large inlets may support too many waveguide modes to allow an efficient modal analysis. Chapter 6 discusses an alternative ray method useful for large guide widths, however, the latter is not as accurate because it ignores diffraction effects at the open end which propagate into the guide and can eventually dominate over the reflection effects over long paths.

For the TE case

$$\begin{aligned}
\hat{e}_n^{\pm}(y) &= \hat{e}_n(y) \\
&= \hat{z} P_n \sin(\frac{n\pi}{d} y) && (3.4) \\
\hat{h}_n^{\pm}(y) &= \pm \hat{h}_{nt}(y) + \hat{h}_{na}(y) \\
&= P_n Y_0 \left[\mp \hat{y} \frac{\beta_n}{k} \sin(\frac{n\pi}{d} y) - \hat{x} \frac{n\pi}{jkd} \cos(\frac{n\pi}{d} y) \right] && (3.5) \\
P_n &= \sqrt{\frac{2kZ_0}{d\beta_n}} && (3.6)
\end{aligned}$$

and for the TM case

$$\begin{aligned}
\hat{h}_n^{\pm}(y) &= \hat{h}_n(y) \\
&= \hat{z} P_n \cos(\frac{n\pi}{d} y) && (3.7) \\
\hat{e}_n^{\pm}(y) &= \pm \hat{e}_{nt}(y) + \hat{e}_{na}(y) \\
&= P_n Z_0 \left[\pm \hat{y} \frac{\beta_n}{k} \cos(\frac{n\pi}{d} y) - \hat{x} \frac{n\pi}{jkd} \sin(\frac{n\pi}{d} y) \right] && (3.8) \\
P_n &= \sqrt{\frac{2kY_0}{d\beta_n \varepsilon_n}} && (3.9)
\end{aligned}$$

$$\varepsilon_n = \begin{cases} 2 & \text{if } n = 0 \\ 1 & \text{otherwise} \end{cases} \tag{3.10}$$

where Z_0 is free space impedance, Y_0 is free space admittance and k is the free space wave number, $2\pi/\lambda$. The subscripts "t" and "a" signify the transverse and axial components, respectively, of the fields which lie in the plane of incidence (in this case, the $\hat{y}$ and $\hat{x}$ components, respectively). Notice that for the TE case there is only a $\hat{z}$-component of the E-field. Similarly, there is only a $\hat{z}$-component of the H-field for the TM case. This helps simplify the analysis of two dimensional structures. The derivation of these modes is given in Appendix A.

These modal fields can be physically interpreted in terms of an equivalent set of modal ray fields by expressing the sine and cosine terms in their Euler form and combining their exponential arguments as shown in Appendix A. For the TE case

$$\hat{e}_n(y)e^{\mp j\beta_n x} = \hat{z}\frac{P_n}{2j}\left[e^{jk(y\sin\theta_n \mp x\cos\theta_n)} - e^{jk(-y\sin\theta_n \mp x\cos\theta_n)}\right] \tag{3.11}$$

and for the TM case

$$\hat{h}_n(y)e^{\mp j\beta_n x} = \hat{z}\frac{P_n}{2}\left[e^{jk(y\sin\theta_n \mp x\cos\theta_n)} + e^{jk(-y\sin\theta_n \mp x\cos\theta_n)}\right] \tag{3.12}$$

where

$$\theta_n = \sin^{-1}\left(\frac{n\pi}{kd}\right). \tag{3.13}$$

As figure 3.2 shows, the above alternative expressions for $\hat{e}_n(y)e^{\pm j\beta_n x}$ and $\hat{h}_n(y)e^{\pm j\beta_n x}$ represent oppositely traveling plane waves within the guide which make a characteristic modal ray angle of θ_n with the walls. This ray-optic interpretation will be important when the reflection from a junction is calculated later.

Figure 3.3 shows an annular guide which extends to infinity in the $\pm\phi$-directions. This, of course, is physically impossible because it would just connect up with itself to form a closed ring. However, this is allowable mathematically, and is neccesary to avoid the periodic ϕ boundary condition of an annular guide of 360 degrees because

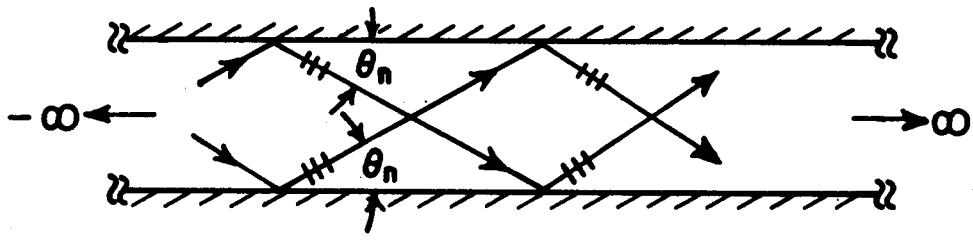

Figure 3.2: Modal rays of the parallel plate waveguide.

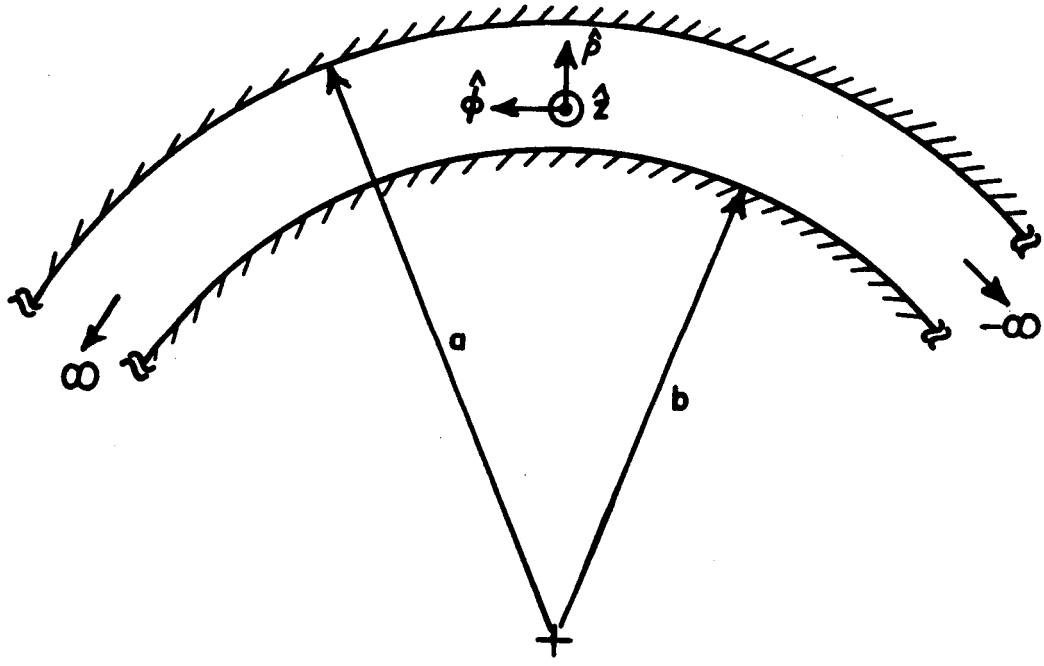

Figure 3.3: Annular waveguide geometry

the bent portions of the inlet are made up of sections of annular guides which are fractions of this. The total field propagating in the $\pm\hat{\phi}$-direction can be expressed as (see Appendix B)

$$\vec{E}^{\pm}(\rho,\phi) = \sum_{n=1}^{N} B_n^{\pm}\hat{e}_n^{\pm}(\rho)e^{\mp j\nu_n\phi} \tag{3.14}$$

$$\vec{H}^{\pm}(\rho,\phi) = \sum_{n=1}^{N} B_n^{\pm}\hat{h}_n^{\pm}(\rho)e^{\mp j\nu_n\phi}. \tag{3.15}$$

For the TE case

$$\begin{aligned}
\hat{e}_n^{\pm}(\rho) &= \hat{e}_n(\rho) \\
&= \hat{z}A_nR_n(k\rho) && (3.16)\\
\hat{h}_n^{\pm}(\rho) &= \pm h_{nt}(\rho) + \hat{h}_{na}(\rho) \\
&= A_nY_0\left[\pm\hat{\rho}\frac{\nu_n}{k\rho}R_n(k\rho) - \hat{\phi}jR_n'(k\rho)\right] && (3.17)\\
R_n(k\rho) &= \frac{1}{2j}\left[H_{\nu_n}^{(2)}(kb)H_{\nu_n}^{(1)}(k\rho) - H_{\nu_n}^{(1)}(kb)H_{\nu_n}^{(2)}(k\rho)\right] && (3.18)\\
A_n &= \left[\frac{\nu_n}{kZ_0}\int_{kb}^{ka} R_n^2(u)\frac{du}{u}\right]^{-\frac{1}{2}} && (3.19)\\
R_n(ka) &= 0 && (3.20)
\end{aligned}$$

where the transcendental equation (3.20) is solved for the eigenvalues ν_n. For the TM case

$$\begin{aligned}
\hat{h}_n^{\pm}(\rho) &= \hat{h}_n(\rho) \\
&= \hat{z}A_nR_n(k\rho) && (3.21)\\
\hat{e}_n^{\pm}(\rho) &= \pm e_{nt}(\rho) + \hat{e}_{na}(\rho) \\
&= A_nZ_0\left[\mp\hat{\rho}\frac{\nu_n}{k\rho}R_n(k\rho) + \hat{\phi}jR_n'(k\rho)\right] && (3.22)\\
R_n(k\rho) &= \frac{1}{2j}\left[H_{\nu_n}^{(2)\prime}(kb)H_{\nu_n}^{(1)}(k\rho) - H_{\nu_n}^{(1)\prime}(kb)H_{\nu_n}^{(2)}(k\rho)\right] && (3.23)\\
A_n &= \left[\frac{\nu_n}{kY_0}\int_{kb}^{ka} R_n^2(u)\frac{du}{u}\right]^{-\frac{1}{2}} && (3.24)
\end{aligned}$$

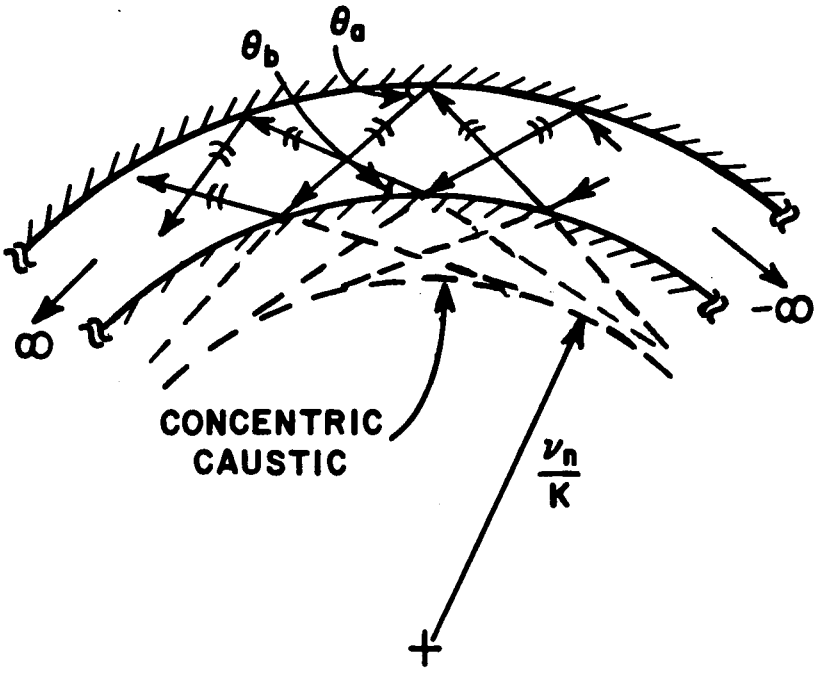

Figure 3.4: Modal rays of the annular waveguide.

$$R_n'(ka) = 0 \tag{3.25}$$

where the transcendental equation (3.25) is solved for the eigenvalues ν_n. $H_{\nu_n}^{(1)}$, $H_{\nu_n}^{(2)}$, $H_{\nu_n}^{(1)\prime}$, and $H_{\nu_n}^{(2)\prime}$ are the Hankel functions of the first and second kinds of order ν_n and their derivatives with respect to argument, respectively. For this case $\hat{\rho}$ is the transverse direction and $\hat{\phi}$ is the axial direction.

The modal ray form of the modal fields in the annular guide are obtained using the Debye Tangent approximation for the Hankel functions. This is done in Appendix B. The geometrical interpretation is shown in figures 3.4 and 3.5. It consists of oppositely crossing cylindrical waves that form a circular modal caustic which is concentric with the walls of the guide with radius ν_n/k. The angles these

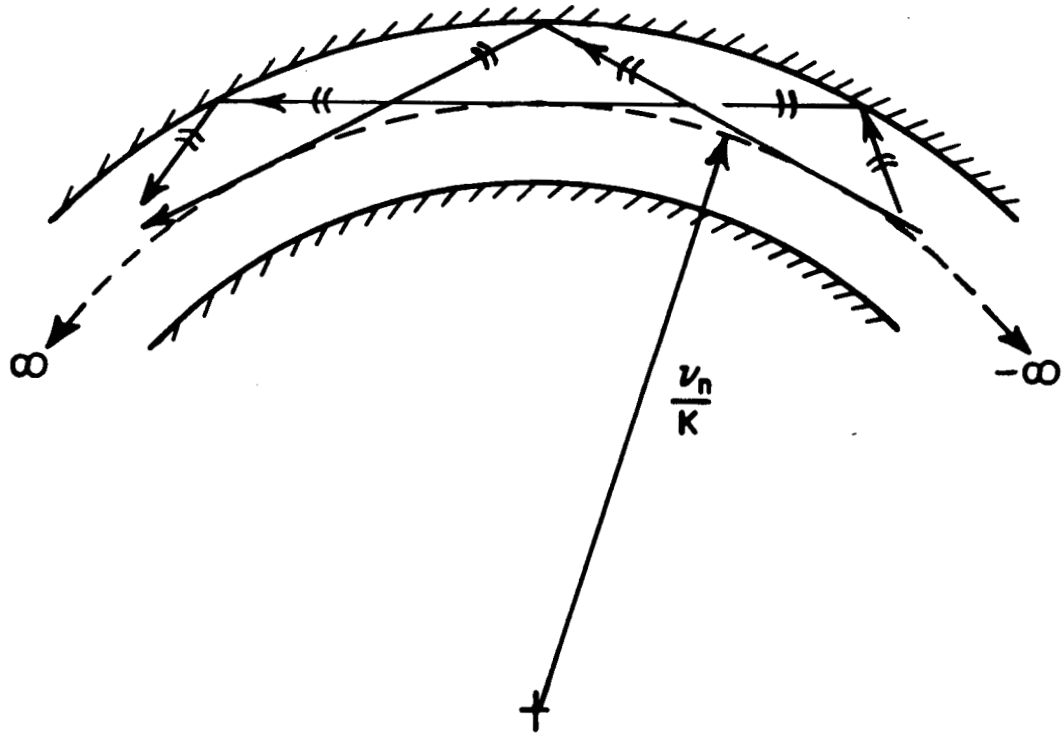

Figure 3.5: Whispering gallery type modal rays of the annular waveguide.

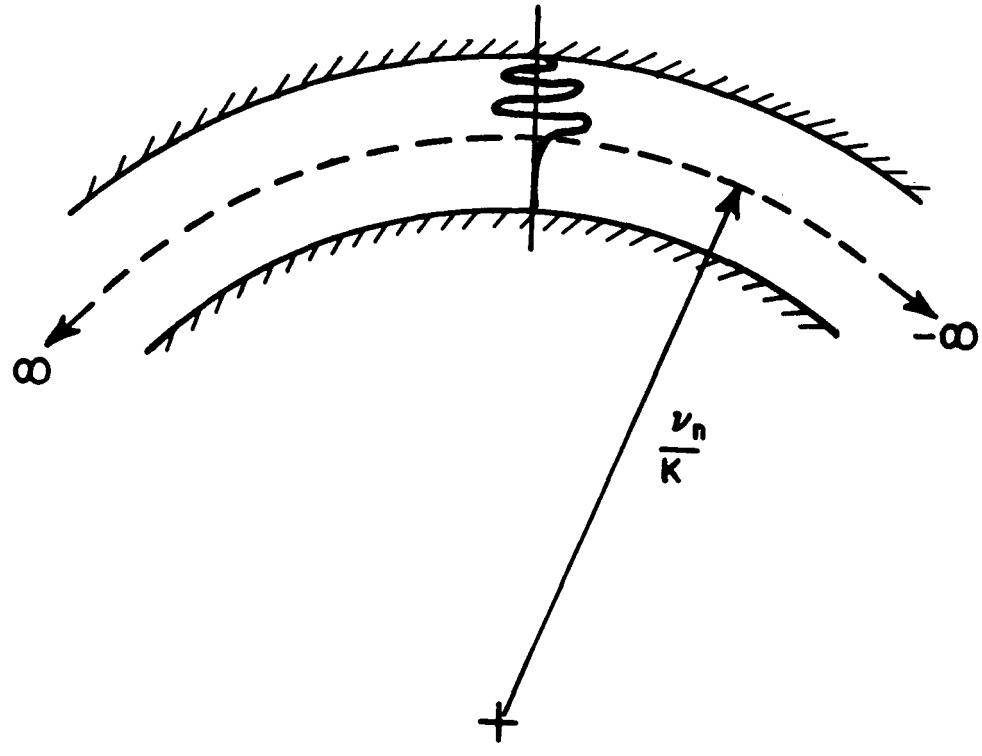

Figure 3.6: Field of a whispering gallery type mode.

modal rays (with cylindrical spreading) make with the guide walls are given by

$$\theta_{an} = \cos^{-1}(\frac{\nu_n}{ka}) \tag{3.26}$$

$$\theta_{bn} = \cos^{-1}(\frac{\nu_n}{kb}). \tag{3.27}$$

As shown in figure 3.5, the caustic contour can lie inside the guide. This special case is called a "Whispering Gallery" (WG) mode and is encountered in most concave surface guided wave problems. This particular type of waveguide mode confines most of its power in between the caustic contour and the outer wall, as shown in figure 3.6. So, ray-optically, the propagating part of a WG mode never

"sees" the inner wall even though its eigenvalue is dependent on the existance of the inner wall.

It is seen from the ray-optical forms that the waveguide modes of the parallel plate guide and the annular guide are closely analogous. In fact, the number of propagating modes are almost always the same for the two types of guides if they are of the same width. Furthermore, it is straightforward to show that the modes of the annular guide approach those of the parallel plate guide as the radius approaches infinity.

3.2 Evaluation of the Elements of the Scattering Matrices

The elements of all the scattering matrices are calculated by first replacing the discontinuities in the guide with equivalent currents which simulate the effects of the discontinuity [1]. The reflection and transmission type matrix elements are then simply the excitation coefficients due to these currents radiating in a uniform guide of infinite extent when a mode of unit amplitude is incident on the junction in question. For example, to find the elements of $[R_{12}]$ the junction would be replaced by a uniform parallel plate guide with equivalent currents where the junction used to be (see Figures 3.7 and 3.8). It is then important to find these equivalent currents accurately. The excitation coefficient of the n^{th} mode due to current sources in a uniform guide (see Figure 3.9) is given by [1]

$$C_n^{\pm} = -\frac{1}{2}\int_{\vec{J},\vec{M}} \left[\hat{e}_n \cdot \vec{J} - (\mp\hat{h}_{nt} + \hat{h}_{na}) \cdot \vec{M}\right] ds \tag{3.28}$$

$$C_n^{\pm} = -\frac{1}{2}\int_{\vec{J},\vec{M}} \left[(\pm\hat{e}_{nt} - \hat{e}_{na}) \cdot \vec{J} + \hat{h}_n \cdot \vec{M}\right] ds \tag{3.29}$$

for the TE and TM cases, respectively, in the $\pm\hat{a}$ directions. $\vec{J}$ and $\vec{M}$ are the equivalent electric and magnetic current sources and $\hat{a}$ is the unit vector in the axial direction. The subscripts "t" and "a" again mean "the component in the transverse direction (to $\hat{a}$)" and "the component in the axial direction". It is noted

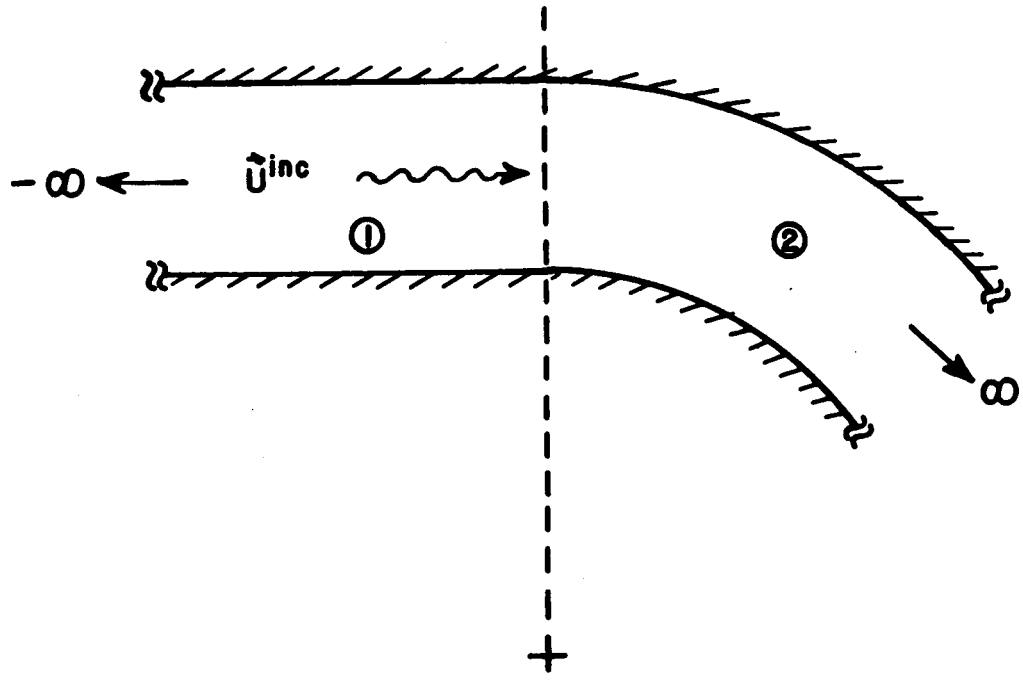

Figure 3.7: Mode incident on junction between waveguide sections 1 and 2.

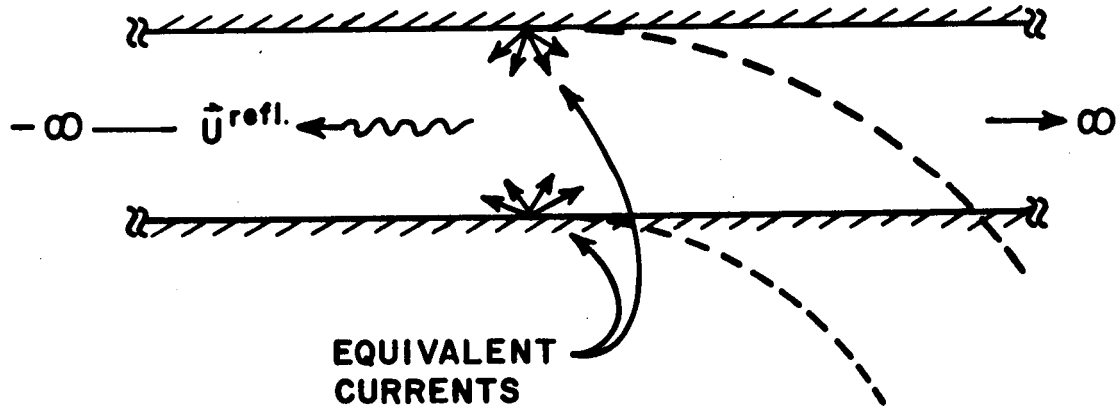

Figure 3.8: Junction replaced by parallel plate waveguide with equivalent currents.

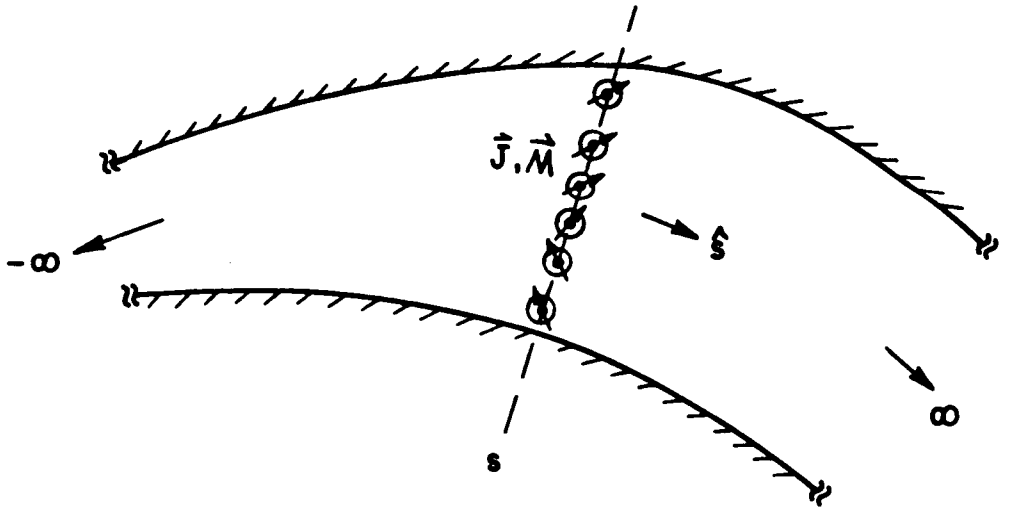

Figure 3.9: Current sources in a cross section of a uniform guide of infinite extent.

that (3.28) and (3.29) apply to both transmission and reflection calculations where the integrations are performed over the appropriate source regions which must lie in a cross section of the guide.

3.2.1 Junction Transmission Matrices

The transmission matrix elements T_{pq}^{mn} are found by replacing the incident modal field with equivalent incident electric and magnetic surface currents in the aperture formed by the junction and then evaluating the excitation of the transmitted modes by these currents using (3.28) and (3.29). To illustrate the procedure, $[T_{12}]$ will be derived for the TE case. $[T_{12}]$ describes the transmission of energy from section 1 across the junction to section 2. T_{12}^{mn} is the transmission matrix element which is the excitation coefficient of the m^{th} transmitted mode in section 2 when the n^{th} mode of section 1 is incident on the junction. Using equation (3.28), it is given by

$$T_{12}^{mn} = -\frac{1}{2}\int_b^a \left\{\hat{e}_m(\rho)\cdot\vec{J}_n - [\hat{h}_{mt}(\rho)+\hat{h}_{ma}(\rho)]\cdot\vec{M}_n\right\} d\rho \tag{3.30}$$

where $\hat{a}$ is $\hat{\phi}$ and

$$\hat{e}_m(\rho) = \hat{z}A_m R_m(k\rho) \tag{3.31}$$

$$\hat{h}_{mt}(\rho) = \hat{\rho}A_m Y_0 \frac{\nu_m}{k\rho} R_m(k\rho) \tag{3.32}$$

$$\hat{h}_{ma}(\rho) = -\hat{\phi}jA_m Y_0 R'_m(k\rho). \tag{3.33}$$

The equivalent currents, $\vec{J} = \hat{n}\times\vec{H}$ and $\vec{M} = \vec{E}\times\hat{n}$ are given by

$$\begin{aligned}\vec{J}_n &= \hat{x}\times\hat{h}_n^+(y)\\ &= -\hat{z}P_n Y_0 \frac{\beta_n}{k}\sin(\frac{n\pi}{d}y)\end{aligned} \tag{3.34}$$

$$\begin{aligned}\vec{M}_n &= \hat{e}_n^+(y)\times\hat{x}\\ &= \hat{y}P_n \sin(\frac{n\pi}{d}y).\end{aligned} \tag{3.35}$$

Substituting back into equation (3.30) gives

$$T_{12}^{mn} = \frac{1}{2}A_m P_n Y_0 \int_b^a \left(\frac{\beta_n}{k} + \frac{\nu_m}{k\rho}\right) \sin(\frac{n\pi}{d}y) R_m(k\rho) d\rho. \tag{3.36}$$

Using $y = \rho - b$ and changing variables to $u = k\rho$ results in

$$T_{12}^{mn} = \frac{1}{2}A_m P_n \frac{Y_0}{k} \int_{kb}^{ka} \left(\frac{\beta_n}{k} + \frac{\nu_m}{u}\right) \sin\left[\frac{n\pi}{kd}(u - kb)\right] R_m(u) du. \tag{3.37}$$

The integration is done numerically or possibly through the use of asymptotics if the guide is large enough. T_{12}^{mn} is found similarly for the TM case

$$T_{12}^{mn} = \frac{1}{2}A_m P_n \frac{Z_0}{k} \int_{kb}^{ka} \left(\frac{\beta_n}{k} + \frac{\nu_m}{u}\right) \cos\left[\frac{n\pi}{kd}(u - kb)\right] R_m(u) du. \tag{3.38}$$

If T_{21}^{mn} is derived using the same procedure, it is found that $T_{21}^{mn} = T_{12}^{nm}$, as mentioned earlier in Chapter 2. T_{54}^{mn} is the same as T_{12}^{mn} with the appropriate changes in radii a and b.

The equivalent sources $\vec{J}_n$ and $\vec{M}_n$ are based on the modes incident on the junction. This approximation should generally provide the dominant contribution to T_{12}^{mn}. A correction to this approximation can be deduced via a modification of Ufimtsev's Physical Theory of Diffraction in which equivalent currents based on the fringe wave diffraction by the junction are used to obtain this correction [3]. The latter correction is usually weak and is therefore neglected here.

3.2.2 Transmission Matrices of the Open End

The coupling of the incident plane wave into the first section is described by the column matrix $[T_{01}]$, as defined in chapter 2. The elements of $[T_{01}]$ are found using, once again, equivalent currents and the excitation coefficient equation very similarly to the manner in which the junction transmission matrices were derived above. The element T_{01}^n is the excitation coefficient of the n^{th} mode of section 1 due to the plane wave of unit amplitude incident at angle θ. For the TE case

$$T_{01}^n = -\frac{1}{2}\int_0^d \left\{\hat{e}_n(y) \cdot \vec{J} - [-\hat{h}_{nt}(y) + \hat{h}_{na}(y)] \cdot \vec{M}\right\} dy. \tag{3.39}$$

The equivalent currents $\vec{J}$ and $\vec{M}$ are found as before using the Kirchhoff approximation indicated previously in section 3.2.1, namely

$$\begin{aligned}
\vec{M} &= \vec{E}^{inc} \times \hat{x} \\
&= \hat{z} e^{-jky\sin\theta} \times \hat{x} \\
&= \hat{y} e^{-jky\sin\theta} \qquad (3.40) \\
\vec{J} &= \hat{x} \times \vec{H}^{inc} \\
&= \hat{x} \times Y_0 e^{-jky\sin\theta}(\hat{x}\sin\theta - \hat{y}\cos\theta) \\
&= -\hat{z} Y_0 e^{-jky\sin\theta}\cos\theta \qquad (3.41) \\
\hat{e}_n(y) &= \hat{z} P_n \sin(\frac{n\pi}{d}y) \qquad (3.42) \\
\hat{h}_{nt}(y) &= -\hat{y} P_n Y_0 \frac{\beta_n}{k}\sin(\frac{n\pi}{d}y). \qquad (3.43)
\end{aligned}$$

Substituting back into equation (3.39) and integrating gives

$$\begin{aligned}
T_{01}^n &= \frac{1}{4} Y_0 P_n d e^{-j\frac{1}{2}kd\sin\theta} j^{n-1}\left(\cos\theta + \frac{\beta_n}{k}\right) \\
&\quad \cdot \left\{ \text{sinc}\left[\frac{1}{2}kd(\sin\theta_n - \sin\theta)\right]\right. \\
&\quad \left. -(-1)^n \text{sinc}\left[\frac{1}{2}kd(\sin\theta_n + \sin\theta)\right]\right\} \qquad (3.44)
\end{aligned}$$

where

$$\text{sinc}x = \frac{\sin x}{x}. \qquad (3.45)$$

Notice that the sinc function peaks when $\theta = \pm\theta_n$, which is understandable physically when the modal ray form of the modes is considered. The coupling is maximum when the incident plane wave lies along a modal ray angle.

The TM case is found similarly as

$$\begin{aligned}
T_{01}^n &= \frac{1}{4} Z_0 P_n d e^{-j\frac{1}{2}kd\sin\theta} j^{n}\left(\cos\theta + \frac{\beta_n}{k}\right) \\
&\quad \cdot \left\{ \text{sinc}\left[\frac{1}{2}kd(\sin\theta_n - \sin\theta)\right]\right.
\end{aligned}$$

$$+(-1)^n \text{sinc}\left[\frac{1}{2}kd(\sin\theta_n + \sin\theta)\right]\Big\}. \tag{3.46}$$

The elements of the matrix $[T_{10}]$ are found using the aperture integration (AI) technique. The element T_{10}^n is the coefficient of the radiated field due to the n^{th} mode of section 1 being incident on the open end. For the TE case, it is defined by

$$T_{10}^n \frac{e^{-jk\rho}}{\sqrt{\rho}} = \sqrt{\frac{jk}{8\pi}} \frac{e^{-jk\rho}}{\sqrt{\rho}} \int_0^d \left[\cos\theta E_z^{ap}(y) + Z_0 H_y^{ap}(y)\right] e^{-jky\sin\theta} dy \tag{3.47}$$

where ρ is the distance to the receiver referenced from the lower edge $(x, y = 0)$ of the inlet. This integral is derived in Appendix E. The aperture field is the n^{th} modal field,

$$\begin{aligned} E_z^{ap}(y) &= \hat{z} \cdot \hat{e}_n(y) \\ &= P_n \sin(\frac{n\pi}{d} y) \\ H_y^{ap}(y) &= \hat{y} \cdot \hat{h}_n^-(y) \\ &= P_n Y_0 \frac{\beta_n}{k} \sin(\frac{n\pi}{d} y). \end{aligned} \tag{3.48}$$

Substituting for the aperture field, integrating and removing the cylindrical wave term gives the matrix element as

$$\begin{aligned} T_{10}^n = \frac{1}{4}\sqrt{\frac{jk}{2\pi}} P_n d e^{-j\frac{1}{2}kd\sin\theta} j^{n-1} \left(\cos\theta + \frac{\beta_n}{k}\right) \\ \cdot \Big\{ \text{sinc}\left[\frac{1}{2}kd(\sin\theta_n - \sin\theta)\right] \\ -(-1)^n \text{sinc}\left[\frac{1}{2}kd(\sin\theta_n + \sin\theta)\right]\Big\}. \end{aligned} \tag{3.49}$$

Notice again that due to the sinc functions, the radiation is maximum along the direction of the modal ray angles. Also notice the close similarity between the expressions for T_{01}^n and T_{10}^n. This is due to reciprocity.

The TM case is found similarly and is given by

$$T_{10}^n = \frac{1}{4}\sqrt{\frac{jk}{2\pi}} P_n d e^{-j\frac{1}{2}kd\sin\theta} j^n \left(\cos\theta + \frac{\beta_n}{k}\right)$$

$$\cdot\left\{\text{sinc}\left[\frac{1}{2}kd(\sin\theta_n-\sin\theta)\right]\right.$$
$$\left.+(-1)^n\text{sinc}\left[\frac{1}{2}kd(\sin\theta_n+\sin\theta)\right]\right\}. \tag{3.50}$$

3.2.3 Reflection Matrix Elements for a Junction

The reflection matrix elements are found by replacing the discontinuity of a junction with equivalent line currents placed on the walls at the junction and then finding the excitation of the reflected modes by these currents [1]. The equivalent line currents are found using the Geometrical Theory of Diffraction (GTD). First, the modal ray form of the incident mode is used to find the modal ray field incident on the discontinuity. That incident modal ray field undergoes diffraction at the discontinuity. Then the line current which radiates in the presence of the waveguide walls is found using the diffraction coefficient for the discontinuity. The method will be illustrated by deriving $[R_{10}]$ and $[R_{12}]$.

The geometry relevant to $[R_{10}]$ is shown in Figure 3.10 and the equivalent geometry with the discontinuity replaced is shown in figure 3.11. R_{10}^{mn} is the reflection matrix element which is the excitation coefficient of the m^{th} mode reflected from the open end of section 1 when the n^{th} mode is incident from section 1. For the TE case, using equation (3.28)

$$R_{10}^{mn} = -\frac{1}{2}\int_0^d \left\{\hat{e}_m(y)\cdot\vec{J}_n-[-\hat{h}_{mt}(y)+\hat{h}_{ma}(y)]\cdot\vec{M}_n\right\}dy \tag{3.51}$$

where $\hat{a}=\hat{x}$ and

$$\hat{e}_m(y) = \hat{z}P_m\sin(\frac{m\pi}{d}y) \tag{3.52}$$
$$\hat{h}_{mt}(y) = -\hat{y}P_mY_0\frac{\beta_m}{k}\sin(\frac{m\pi}{d}y) \tag{3.53}$$
$$\hat{h}_{ma}(y) = -\hat{x}P_mY_0\frac{m\pi}{jkd}\cos(\frac{m\pi}{d}y). \tag{3.54}$$

Since the line sources are located at the junction on a conducting plane, the electric source is shorted out leaving only magnetic currents. For the TE case these magnetic

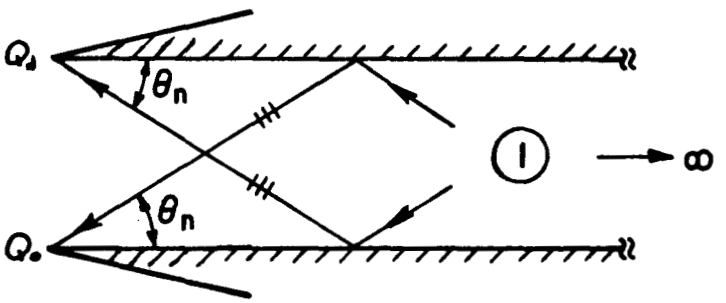

Figure 3.10: Geometry relevant for finding $[R_{10}]$.

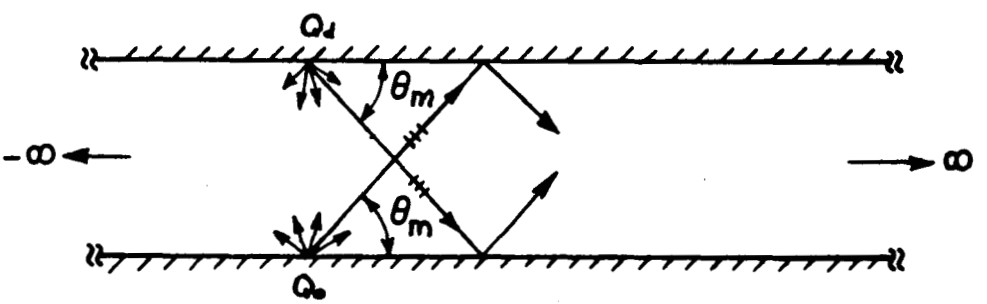

Figure 3.11: Aperture replaced by equivalent currents.

sources are a line of $\hat{x}$-directed infinitesimal dipoles located at Q_0 and Q_d. The equivalent sources are therefore

$$\vec{J}_n = 0 \tag{3.55}$$

$$\vec{M}_n = \hat{x}M_n^{dip}(Q_0)\delta(y) + \hat{x}M_n^{dip}(Q_d)\delta(y-d) \tag{3.56}$$

where $\delta(y)$ is the Dirac delta function. Substituting back into equation (3.51) gives

$$R_{10}^{mn} = \frac{1}{2}P_m Y_0 \frac{m\pi}{jkd}\left[M_n^{dip}(Q_0) + (-1)^m M_n^{dip}(Q_d)\right]. \tag{3.57}$$

It remains only to find the scalars $M_n^{dip}(Q_0)$ and $M_n^{dip}(Q_d)$, which are the strengths of the line dipoles. This is done by finding the modal ray form of mode n incident on the discontinuities and using the appropriate diffraction coefficient [1] which is presented in Appendix C. The line source strengths are then given by [4]

$$M_n^{dip}(Q_0) = -\sqrt{\frac{2\pi}{jk}}\frac{D_s(\theta_m,\theta_n)}{\sin\theta_m}\hat{e}_n^{opt}(Q_0)\cdot\hat{z} \tag{3.58}$$

$$M_n^{dip}(Q_d) = \sqrt{\frac{2\pi}{jk}}\frac{D_s(\theta_m,\theta_n)}{\sin\theta_m}\hat{e}_n^{opt}(Q_d)\cdot\hat{z} \tag{3.59}$$

where θ_m and θ_n are the modal ray mode angles of the reflected and incident modes and, using equation (3.11),

$$\hat{e}_n^{opt}(Q_0)\cdot\hat{z} = \frac{P_n}{2j} \tag{3.60}$$

$$\hat{e}_n^{opt}(Q_d)\cdot\hat{z} = -(-1)^n\frac{P_n}{2j}. \tag{3.61}$$

Substituting equations (3.58), (3.59), (3.60) and (3.61) back into equation (3.57) gives the final expression

$$R_{10}^{mn} = \begin{cases} -P_m P_n Y_0\sqrt{\frac{\pi}{j2k}}D_s(\theta_m,\theta_n) & \text{if } m+n \text{ even} \\ 0 & \text{otherwise} \end{cases}. \tag{3.62}$$

$[R_{10}]$ for the TM case is found similarly, except that magnetic line sources are used rather than magnetic line dipole sources [4],

$$\vec{M}_n = \hat{z}M_n^{lin}(Q_0)\delta(y) + \hat{z}M_n^{lin}(Q_d)\delta(y-d) \tag{3.63}$$

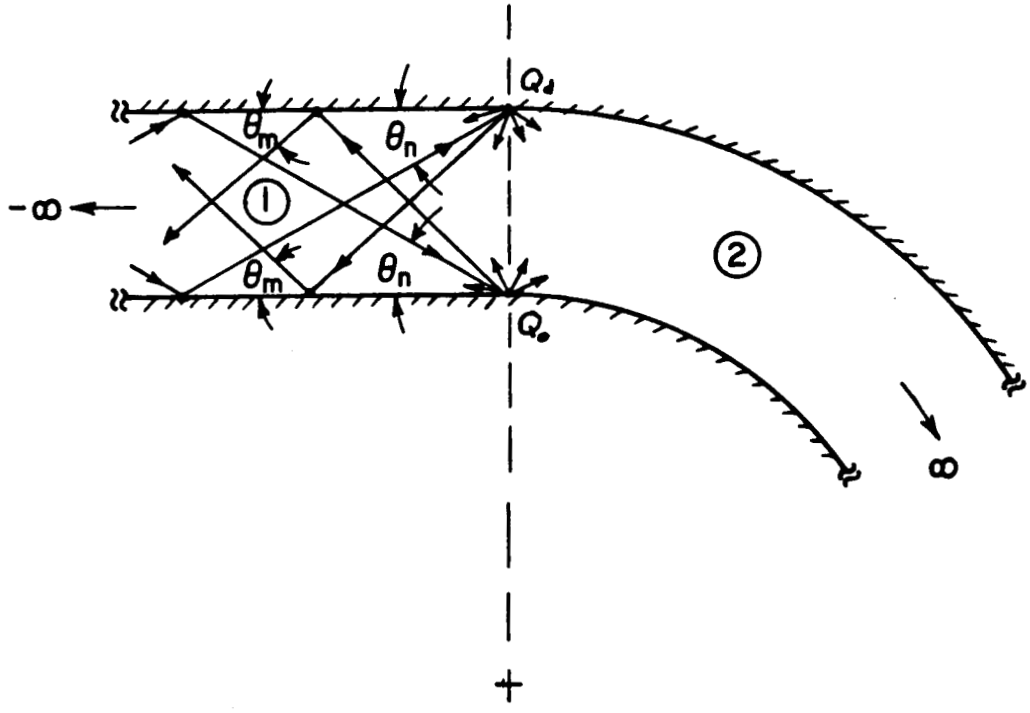

Figure 3.12: Geometry relevant for finding $[R_{12}]$.

$$M_n^{lin}(Q_0) = -Z_0\sqrt{\frac{2\pi}{jk}}D_h(\theta_m,\theta_n)\hat{h}_n^{opt}(Q_0)\cdot\hat{z} \tag{3.64}$$

$$M_n^{lin}(Q_d) = -Z_0\sqrt{\frac{2\pi}{jk}}D_h(\theta_m,\theta_n)\hat{h}_n^{opt}(Q_d)\cdot\hat{z}. \tag{3.65}$$

The final expression is then

$$R_{10}^{mn} = \begin{cases} P_m P_n Z_0\sqrt{\frac{\pi}{j2k}}D_h(\theta_m,\theta_n) & m+n \text{ even} \\ 0 & \text{otherwise} \end{cases}. \tag{3.66}$$

Notice that since the diffraction coefficient is reciprical, $[R_{10}]$ is symmetric. This reduces the number of computations considerably.

Figure 3.12 shows the relevant geometry for finding $[R_{12}]$. The matrix $[R_{12}]$ relates the modes reflected back into section 1 from the junction between sections 1 and 2 when a mode is incident also from section 1. It is found exactly the same as $[R_{10}]$ except that now the diffraction coefficients are for discontinuities in curvature.

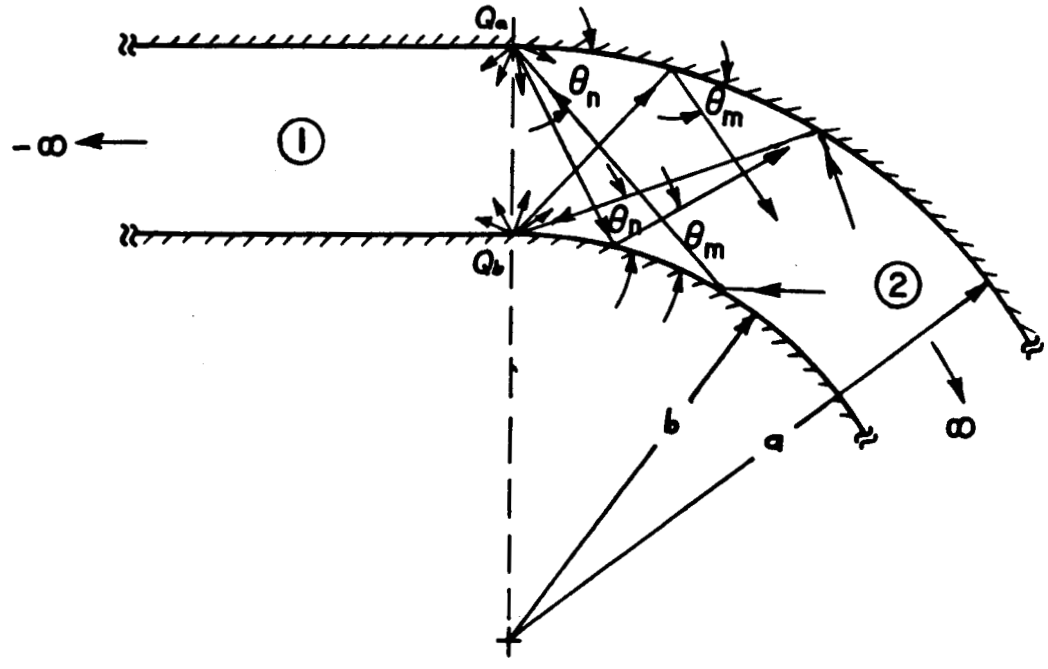

Figure 3.13: Geometry relevant for finding $[R_{21}]$.

For the TE case the matrix elements are given by

$$R_{12}^{mn} = -\frac{1}{2}P_m P_n Y_0 \sqrt{\frac{\pi}{j2k}} \cdot \left[D_s^c(\theta_m,\theta_n)|_{Q_0} + (-1)^{m+n} D_s^c(\theta_m,\theta_n)|_{Q_d}\right] \tag{3.67}$$

and for the TM case by

$$R_{12}^{mn} = \frac{1}{2}P_m P_n Z_0 \sqrt{\frac{\pi}{j2k}} \cdot \left[D_h^c(\theta_m,\theta_n)|_{Q_0} + (-1)^{m+n} D_h^c(\theta_m,\theta_n)|_{Q_d}\right]. \tag{3.68}$$

The diffraction coefficients $D_{s,h}^c$ for a discontinuity in curvature are given in Appendix C. Notice again that due to the diffraction coefficients being reciprical, $[R_{12}]$ is also symmetric.

Figure 3.13 shows the relevant geometry for finding $[R_{21}]$. The matrix $[R_{21}]$

relates the modes reflected back into section 2 from the junction $p = 2$, $q = 1$ when a mode is also incident from section 2. The derivation is the same as above, except that now we are dealing with the modal fields of section 2. It yields the following for the TE case,

$$R_{21}^{mn} = -\frac{1}{2}\int_b^a \left\{\hat{e}_m(\rho)\cdot\vec{J}_n - [\hat{h}_{mt}(\rho)+\hat{h}_{ma}(\rho)]\cdot\vec{M}_n\right\}d\rho \tag{3.69}$$

$$\vec{J}_n = 0 \tag{3.70}$$

$$\vec{M}_n = -\hat{\phi}M_n^{dip}(Q_b)\delta(\rho-b) - \hat{\phi}M_n^{dip}(Q_a)\delta(\rho-a) \tag{3.71}$$

$$\hat{h}_{ma}(\rho) = -\hat{\phi}jA_mY_0R_m'(k\rho) \tag{3.72}$$

$$M_n^{dip}(Q_b) = -\sqrt{\frac{2\pi}{jk}}\frac{D_s(\theta_{bm},\theta_{bn})|_{Q_b}}{\sin\theta_{bm}}\hat{e}_n^{opt}(Q_b)\cdot\hat{z} \tag{3.73}$$

$$\hat{e}_n^{opt}(Q_b)\cdot\hat{z} = \frac{A_n}{2j}H_{\nu_n}^{(2)}(kb)H_{\nu_n}^{(1)}(kb) \tag{3.74}$$

$$M_n^{dip}(Q_a) = \sqrt{\frac{2\pi}{jk}}\frac{D_s(\theta_{am},\theta_{an})|_{Q_a}}{\sin\theta_{am}}\hat{e}_n^{opt}(Q_a)\cdot\hat{z} \tag{3.75}$$

$$\hat{e}_n^{opt}(Q_a)\cdot\hat{z} = -\frac{A_n}{2j}H_{\nu_n}^{(1)}(kb)H_{\nu_n}^{(2)}(ka) \tag{3.76}$$

$$\begin{aligned} R_{21}^{mn} = & -\frac{1}{2}\sqrt{\frac{\pi}{j2k}}A_mA_nY_0 \\ & \cdot\left[\frac{D_s(\theta_{am},\theta_{an})|_{Q_a}}{\sin\theta_{am}}R_m'(ka)H_{\nu_n}^{(1)}(kb)H_{\nu_n}^{(2)}(ka)\right. \\ & \left.+\frac{D_s(\theta_{bm},\theta_{bn})|_{Q_b}}{\sin\theta_{bm}}R_m'(kb)H_{\nu n}^{(2)}(kb)H_{\nu_n}^{(1)}(kb)\right] \end{aligned} \tag{3.77}$$

where the diffraction coefficients are again for a discontinuity in curvature. If either of the modes are of the whispering gallery type, one must neglect the second term of

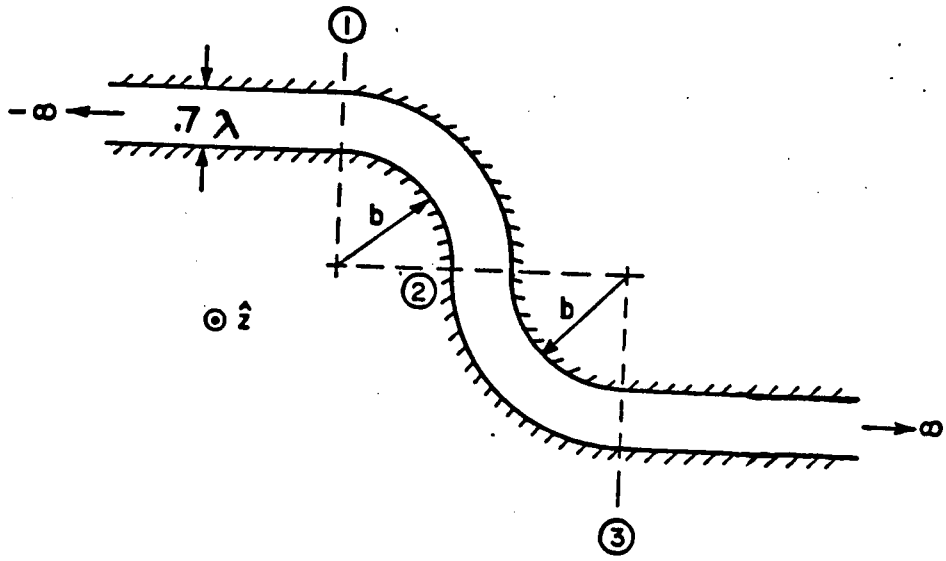

Figure 3.14: Double bend geometry in a parallel plate waveguide of infinite extent.

equation (3.77) which involves the discontinuity at Q_b since there is no whispering gallery modal ray incident at Q_b.

R_{21}^{mn} for the TM case is found similarly and is given by

$$R_{21}^{mn} = \frac{1}{2}\sqrt{\frac{\pi}{j2k}} A_m A_n Z_0 \left[D_h(\theta_{bm}, \theta_{bn})|_{Q_b} R_m(kb) H_{\nu_n}^{(2)\prime}(kb) H_{\nu_n}^{(1)}(kb) + \right.$$
$$\left. + D_h(\theta_{am}, \theta_{an})|_{Q_a} R_m(ka) H_{\nu n}^{(1)\prime}(kb) H_{\nu_n}^{(2)}(ka) \right] \qquad (3.78)$$

with the same condition on whispering gallerly modes as before.

As a numerical example of the reflection from a junction, consider the waveguide of Figure 3.14. For the TE case, this guide allows only one propagating mode in each section. Therefore, the matrices all have just a single element, so they are replaced by scalars. Figure 3.15 plots the magnitude of the component reflection coefficients R_{12}, R_{21}, and R_{24}. Figure 3.16 plots the combined reflection from the

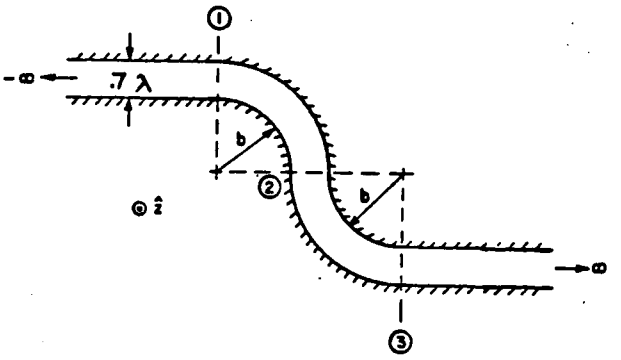

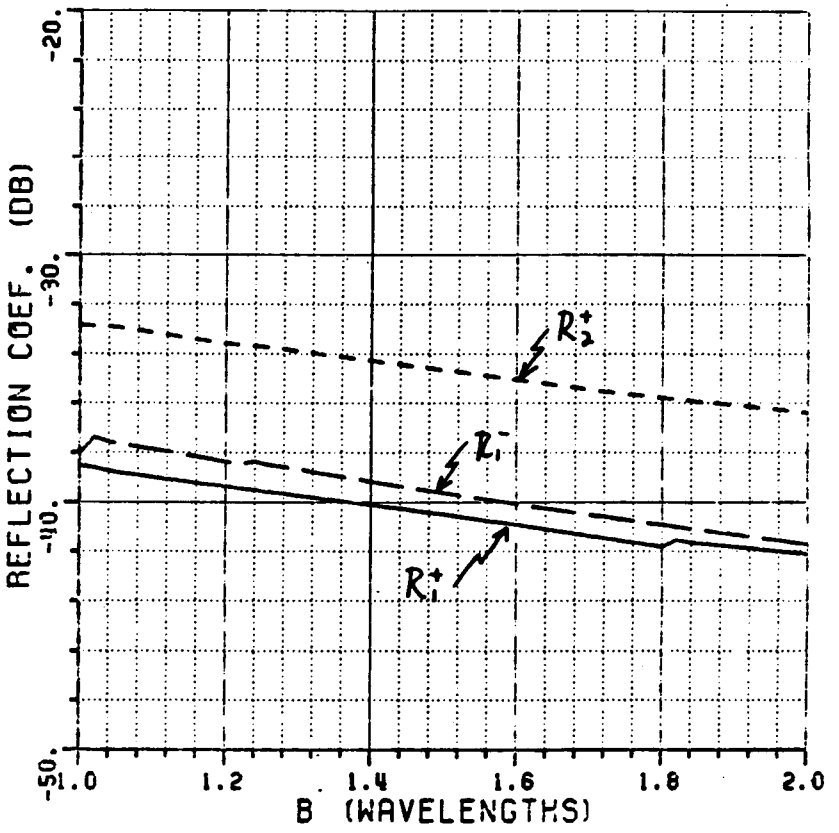

Figure 3.15: Reflection coefficients of the three junctions of the double-bend guide vs. bend radius.

three junctions R_{12}^{MSM}. It is given by

$$R_{12}^{MSM} = R_{12} + \frac{T_{12}T_{21}R_{24}^{MSM}P_2^2}{1 - R_{24}^{MSM}R_{21}P_2^2} \tag{3.79}$$

$$R_{24}^{MSM} = R_{24} + \frac{T_{24}^2 R_{21}P_4^2}{1 - R_{21}R_{24}P_4^2} \tag{3.80}$$

where

$$T_{12} = \sqrt{1 - |R_{12}|^2} \tag{3.81}$$

$$T_{21} = \sqrt{1 - |R_{21}|^2} \tag{3.82}$$

$$T_{24} = \sqrt{1 - |R_{24}|^2} \tag{3.83}$$

$$P_2 = P_4 = e^{-j\nu_1 \frac{\pi}{2}}. \tag{3.84}$$

The transmission coefficients were found by conserving power flow across a junction.

As the plots show, these junction reflections are extremely small so that the reflection from the termination of an inlet, such as the one in Figure 1.1, would completely dominate the total reflection. If the termination is perfectly absorbing, the field scattered by just the edges at the open end would dominate total scattering. For these reasons, the reflections from the smooth junctions between waveguide sections are usually neglected. The amount of energy reflected internally from the open end is of the same order as the external scattering by the open end so that this scattering mechanism should be included.

3.2.4 Reflection Matrix Elements for an Impedance Termination

As an example of a termination reflection matrix, the case of a semi-infinite planar dielectic termination is derived in this section. However, the numerical results shown later use a perfectly conducting termination because this is a worst case where all the energy reaching the termination is reflected back. The reflection matrix $[R_t]$ for a planar surface impedance termination is diagonal with the elements being the appropriate reflection coefficients for plane waves incident on

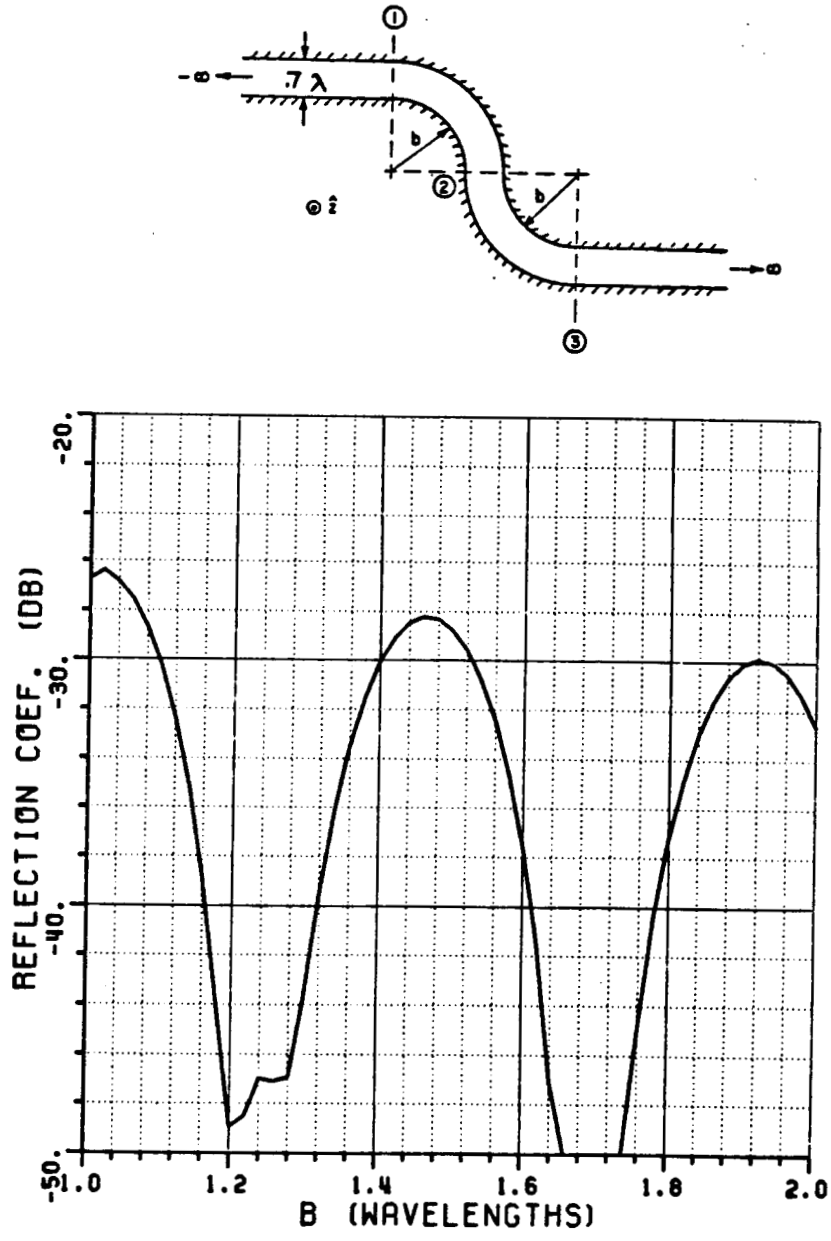

Figure 3.16: MSM reflection coefficient of the double bend vs. bend radius.

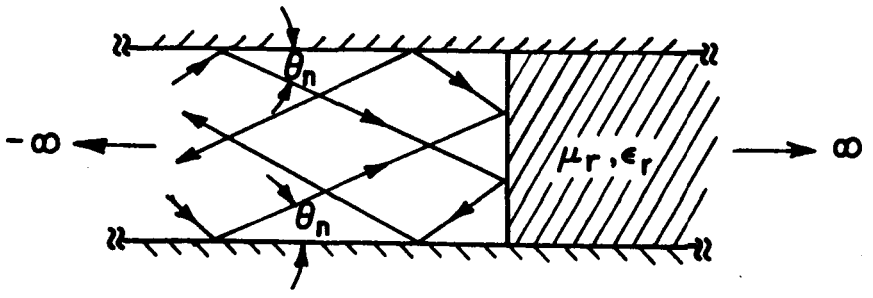

Figure 3.17: Geometry relevant to finding $[R_t]$.

an impedance space. Such an impedance boundary can be created by employing a semi-infinite dielectric termination within the waveguide section 5 as shown in Figure 1.1. Figure 3.17 shows the geometry relevant to $[R_t]$. For the TE case the diagonal elements are given by

$$R_t^{nn} = \frac{\cos\theta_n - \frac{1}{\mu_r}\sqrt{\mu_r\epsilon_r - \sin^2\theta_n}}{\cos\theta_n + \frac{1}{\mu_r}\sqrt{\mu_r\epsilon_r - \sin^2\theta_n}} \tag{3.85}$$

where μ_r and ϵ_r are the relative permeability and permittivity, respectively, of the termination impedance. For the TM case, the diagonal elements are given by

$$R_t^{nn} = \frac{\cos\theta_n - \frac{1}{\epsilon_r}\sqrt{\mu_r\epsilon_r - \sin^2\theta_n}}{\cos\theta_n + \frac{1}{\epsilon_r}\sqrt{\mu_r\epsilon_r - \sin^2\theta_n}}. \tag{3.86}$$

It is noted that the surface impedance referred to above is simply that which is associated with the above reflection coefficients for the dielectric interface shown in Figure 3.17. It is further noted that the expressions for the reflection coefficient (and hence the associated impedance) depends on the mode number through θ_n. The case of the perfectly conducting planar termination is obtained by letting ϵ_r in equations (3.85) and (3.86) go to infinity which makes R_t^{nn} equal -1 and 1 for the TE and TM cases, respectively.

3.2.5 Scattering from the Open End

R_{01} describes the scattering from the open end as defined in chapter 2. It is found by considering the diffraction of the incident plane wave by the two edges of the open end of a semi-infinite parallel plate waveguide. The scattered field, including only first order diffractions, can be written as

$$\begin{aligned} \vec{U}^{edge} &= \hat{z}\,[D_{s,h}(\pi+\theta,\pi+\theta)+ \\ &\quad +D_{s,h}(\pi-\theta,\pi-\theta)e^{-j2kd\sin\theta}]\,\frac{e^{-jk\rho}}{\sqrt{\rho}} \end{aligned} \tag{3.87}$$

where $D_{s,h}$ is the appropriate soft or hard wedge diffraction coefficient as given in Appendix C. Using equations (2.12) and (2.14), the junction reflection coefficient can be identified as

$$R_{01} = D_{s,h}(\pi+\theta,\pi+\theta) + D_{s,h}(\pi-\theta,\pi-\theta)e^{-j2kd\sin\theta}. \tag{3.88}$$

4. Modal Perturbation Technique

In this chapter, the hybrid modal analysis method will be extended to inlet cavities which have a thin absorber coating on their inner walls. The perturbational method which will be used changes only the modal propagation constants β_n and ν_n and leaves the transverse orthonormal modal field structure unchanged. Therefore, the analysis is exactly the same as in the perfectly conducting case of the previous chapter, except for small perturbations to the propagation matrices $[P_q]$ due to the presence of loss on the inlet walls. Also, the diffraction coefficients for the scattering from the open end must be adjusted to handle wedges with one perfectly conducting face and one impedance face.

It will be shown for the parallel plate waveguide that the perturbation of the propagation constants β_n can be obtained using only the plane wave reflection coefficients of the impedance surface and the modal ray angle. Extending this idea to the annular waveguide makes it easy to obtain the perturbation of the propagation constants ν_n which would otherwise be very complicated both analytically and numerically. It is then shown that a thin absorber coating can be represented by an equivalent surface impedance.

4.1 Perturbation of the Modal Propagation Constants in a Parallel Plate Waveguide Due to Nearly Perfectly Conducting Impedance Walls

Figure 4.1 shows the geometry of a parallel plate waveguide of infinite extent with impedance boundary conditions on the walls. Z_s is the normalized (to free space impedance) surface impedance and $Y_s = 1/Z_s$ is the normalized surface admittance. Starting with the TE case, the n^{th} orthonormal modal E-field propagating in the $\pm\hat{x}$-direction can be written in the form

$$\hat{e}_n(x,y) = \hat{z}P_n e_n(y)e^{\mp j\beta_n x} \tag{4.1}$$

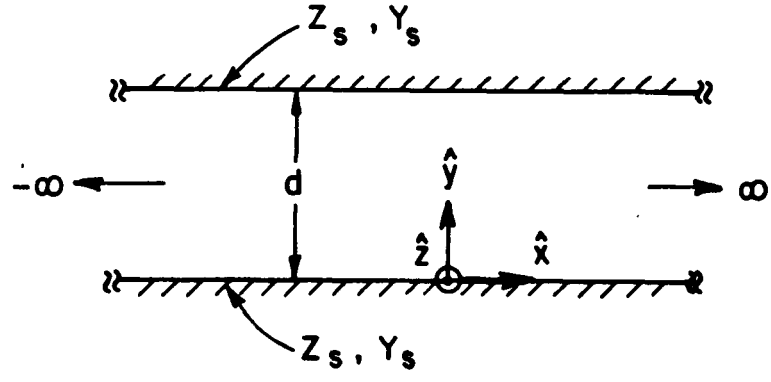

Figure 4.1: Parallel plate waveguide geometry with impedance walls.

where P_n is a normalization constant. Substituting this into the wave equation (A.4), introducing the separation constant k_n and solving the resulting differential equation for the y variable gives the general solution for the transverse modal field as

$$e_n(y) = e^{jk_n y} + Be^{-jk_n y} \tag{4.2}$$

$$\beta_n = \sqrt{k^2 - k_n^2}. \tag{4.3}$$

B and k_n remain to be evaluated using the impedance boundary conditions on the walls. The E-field must satisfy the equations

$$e_n'(0) - jkY_s e_n(0) = 0 \tag{4.4}$$

$$e_n'(d) + jkY_s e_n(d) = 0. \tag{4.5}$$

Substituting (4.2) into these boundary requirements gives the solution for B and the transcendental equation for finding k_n as

$$B = \frac{k_n - kY_s}{k_n + kY_s} \tag{4.6}$$

$$Y_s^2 - 2Y_s(\frac{k_n}{k}) + (\frac{k_n}{k})^2 = \left[Y_s^2 + 2Y_s(\frac{k_n}{k}) + (\frac{k_n}{k})^2\right] e^{j2k_n d}. \tag{4.7}$$

The perturbation requirement is that the surface impedance is nearly perfectly conducting, or $|Y_s| \gg 1$. Using this approximation, the $(k_n/k)^2$ term of (4.7) can

be neglected and (4.2) can be rewritten as

$$Y_s - 2(\frac{k_n}{k}) = \left[Y_s + 2(\frac{k_n}{k})\right] e^{j2k_n d}. \tag{4.8}$$

For the perfectly conducting case $Y_s = \infty$, the solution for k_n is $k_n = n\pi/d$. Therefore, the perturbed form of k_n will be written as

$$k_n = \frac{n\pi}{d} + k'_n \tag{4.9}$$

where the perturbation k'_n is expected to be small for large values of Y_s. Substituting this form into (4.8) and rearranging gives

$$\frac{Y_s - 2(k_n/k)}{Y_s + 2(k_n/k)} = e^{j2k'_n d}. \tag{4.10}$$

Because Y_s is large, the terms on both sides of (4.10) must be close to unity. Therefore, the exponential term can be approximated by the first two terms of its Taylor series expansion:

$$e^{j2k'_n d} \approx 1 + j2k'_n d. \tag{4.11}$$

(4.10) also shows that k'_n is small for large Y_s, as expected. Using this form in (4.10) after some algebra gives

$$(j4d/k)k'^2_n + (4/k + j2dY_s + j4n\pi/k)k'_n + 4n\pi/kd = 0. \tag{4.12}$$

Again, because Y_s is large, all the terms in (4.12) can be neglected except the Y_s term and the constant term. Solving for k'_n gives the perturbation of k_n for the TE case as

$$k'_n = \frac{j2}{dY_s}\left(\frac{n\pi}{kd}\right). \tag{4.13}$$

As expected, k'_n is small for large values of Y_s (it is known from the previous chapter that $n\pi/kd$ is less than one for propagating modes).

The desired result is the perturbation of the propagation constant β_n. This is obtained by substituting (4.9) and (4.13) into (4.3) which gives

$$\beta_n = \sqrt{k^2 - (\frac{n\pi}{d})^2 - \frac{j4}{kdY_s}(\frac{n\pi}{d})^2} \tag{4.14}$$

where the $(1/Y_s)^2$ term is neglected. Because Y_s is large, the square root in (4.14) can be approximated by the first two terms of its binomial expansion which gives

$$\beta_n = \sqrt{k^2 - (\frac{n\pi}{d})^2} - \frac{j2}{dY_s}\frac{(\frac{n\pi}{kd})^2}{\sqrt{1-(\frac{n\pi}{kd})^2}} \tag{4.15}$$

from which the perturbation to the propagation constant can be identified as

$$\beta_n' = -j\frac{2}{dY_s}\frac{(\frac{n\pi}{kd})^2}{\sqrt{1-(\frac{n\pi}{kd})^2}}. \tag{4.16}$$

Using the modal ray angle expression (A.17), β_n' can be rewritten as

$$\beta_n' = -j\frac{2}{dY_s}\frac{\sin^2\theta_n}{\cos\theta_n} \tag{4.17}$$

for the TE case.

The TM case is handled similarly, with the n^{th} orthonormal modal H-field, boundary conditions and transcendental equation for k_n represented as follows:

$$\hat{h}_n(x,y) = \hat{z}P_n h_n(y)e^{\mp j\beta_n x} \tag{4.18}$$

$$h_n(y) = e^{jk_n y} + Be^{-jk_n y} \tag{4.19}$$

$$\beta_n = \sqrt{k^2 - k_n^2} \tag{4.20}$$

$$h_n'(0) - jkZ_s h_n(0) = 0 \tag{4.21}$$

$$h_n'(d) + jkZ_s h_n(d) = 0 \tag{4.22}$$

$$B = \frac{k_n - kZ_s}{k_n + kZ_s} \tag{4.23}$$

$$Z_s^2 - 2Z_s(\frac{k_n}{k}) + (\frac{k_n}{k})^2 = \left[Z_s^2 + 2Z_s(\frac{k_n}{k}) + (\frac{k_n}{k})^2\right]e^{j2k_n d}. \tag{4.24}$$

The perturbation requirement for this polarization is that the surface impedance is nearly perfectly conducting, or Z_s is very small. From (4.24) it is seen that Z_s

should be much less than k_n/k. The smallest value of k_n is $k_1 = \pi/d$ (for the perfectly conducting case), so the TM perturbation requirement is $|Z_s| \ll \pi/kd$. This is a more difficult requirement to meet because the inlet width d is usually fairly large in terms of wavelength. Using this approximation, the Z_s^2 term of (4.24) can be neglected and (4.24) can be rewritten as

$$(\frac{k_n}{k}) - 2Z_s = \left[(\frac{k_n}{k}) + 2Z_s\right] e^{j2k_n d}. \tag{4.25}$$

For the perfectly conducting case $Z_s = 0$, the solution for k_n is again $k_n = n\pi/d$ and the perturbed form of k_n can be written as in (4.9) where the perturbation k_n' is expected to be small for small values of Z_s. It should be mentioned here that this perturbation requirement should be heeded much more closely than in the TE case because k_n can be fairly small. Therefore, Z_s should be much smaller than k_1. Substituting this form into (4.25) and rearranging gives

$$\frac{(k_n/k) - 2Z_s}{(k_n/k) + 2Z_s} = e^{j2k_n' d}. \tag{4.26}$$

Because Z_s is small, the terms on both sides of (4.26) must be close to unity, so (4.11) can again be used to approximate the exponential term. This also shows that k_n' is small, as expected. Using (4.11) in (4.26) after some algebra gives

$$(j2/k)k_n'^2 + (j2n\pi/kd + j4Z_s)k_n' + 4Z_s/d = 0. \tag{4.27}$$

Because Z_s and k_n' are small, the $k_n'^2$ and $Z_s k_n'$ terms of (4.27) can be neglected. Doing this and solving for k_n' gives

$$k_n' = \frac{j2Z_s}{d}\left(\frac{kd}{n\pi}\right). \tag{4.28}$$

The perturbation to β_n is found by substituting (4.28) and (4.9) into (4.20) and using the binomial approximation to the square root function as before, giving

$$\beta_n' = -\frac{j2Z_s}{d}\frac{1}{\sqrt{1 - (\frac{n\pi}{kd})^2}}. \tag{4.29}$$

Using the modal ray expression (A.17), β_n' can be rewritten as

$$\beta_n' = -j\frac{2Z_s}{d\cos\theta_n} \tag{4.30}$$

for the TM case.

4.2 Perturbation of the Modal Propagation Constants in a Waveguide Using the Plane Wave Reflection Coefficient for an Impedance Surface

In this section it will be shown that the perturbation to the propagation constants can be obtained using only the modal ray angles and plane wave reflection coefficients. This will be derived rigorously for the parallel plate waveguide and then extended to the more complicated annular waveguide. For this derivation, it is again neccessary to assume that the surface impedance is nearly perfectly conducting, i.e., $|Y_s| \gg 1$ for the TE case and $|Z_s| \ll \pi/kd$ for the TM case.

4.2.1 Parallel Plate Waveguide

Starting with the TE case, the x-propagating term due to the perturbed propagation constant $e^{-j\beta_n' x}$ will be transformed into a term involving only a reflection coefficient and the modal ray angle θ_n. The propagating term is first rewritten using (4.17) as follows:

$$\begin{aligned} e^{-j\beta_n' x} &= e^{-\frac{2x}{dY_s}\frac{\sin^2\theta_n}{\cos\theta_n}} \\ &= e^{-\frac{2x}{dY_s}\sin\theta_n\tan\theta_n} \\ &= \left(e^{-\frac{2}{Y_s}\sin\theta_n}\right)^{\frac{x}{d}\tan\theta_n}. \end{aligned} \tag{4.31}$$

Because Y_s is large, the term in parenthesis in (4.31) can be approximated with the first two terms of its Taylor expansion giving

$$e^{-j\beta_n' x} \approx \left(1 - \frac{2}{Y_s}\sin\theta_n\right)^{\frac{x}{d}\tan\theta_n}$$

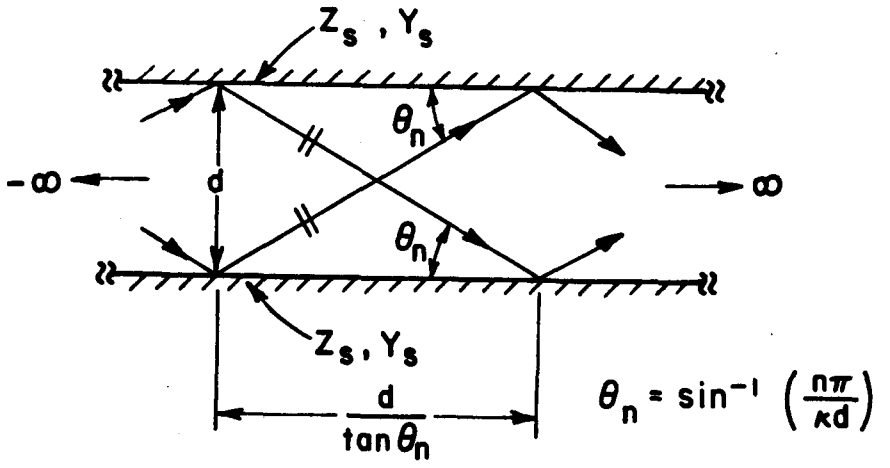

Figure 4.2: Modal ray form of the waveguide modes in a parallel plate waveguide.

$$\begin{aligned} &= \left(\frac{-\sin\theta_n + Y_s - \frac{2}{Y_s}\sin^2\theta_n}{\sin\theta_n + Y_s}\right)^{\frac{x}{d}\tan\theta_n} \\ &\approx \left(-\frac{\sin\theta_n - Y_s}{\sin\theta_n + Y_s}\right)^{\frac{x}{d}\tan\theta_n} \\ &= [-R_s(\theta_n)]^{\frac{x}{d}\tan\theta_n} \end{aligned} \tag{4.32}$$

where $R_s(\theta_n)$ is the soft reflection coefficient for a plane wave incident on a surface admittance Y_s making an angle θ_n with the plane of the surface. The geometrical significance of this form is illustrated in Figure 4.2 which shows the crossing plane waves of the modal ray form of the waveguide modes of a parallel plate waveguide. As the modal field propagates a distance $d/\tan\theta_n$ in the x-direction, the plane waves of the modal ray representation undergo one reflection from the waveguide walls. This is how the perturbation to the propagation constant of a mode is obtained using only a plane wave reflection coefficient and the distance a mode propagates along the axis of the guide between consecutive reflections. Using (4.32), this perturbation is solved in terms of the reflection coefficient for the TE case as

$$\beta_n' = j\frac{\tan\theta_n}{d}\log[-R_s(\theta_n)] \tag{4.33}$$

$$R_s(\theta_n) = \frac{\sin\theta_n - Y_s}{\sin\theta_n + Y_s}. \tag{4.34}$$

The TM case is done similarly as follows

$$\begin{aligned}
e^{-j\beta_n' x} &= e^{-\frac{2Z_s x}{d\cos\theta_n}} \\
&= e^{-\frac{2Z_s x}{d}\frac{\tan\theta_n}{\sin\theta_n}} \\
&= \left(e^{-\frac{2Z_s}{\sin\theta_n}}\right)^{\frac{x}{d}\tan\theta_n} \\
&\approx \left(1 - \frac{2Z_s}{\sin\theta_n}\right)^{\frac{x}{d}\tan\theta_n} \\
&= \left(\frac{\sin\theta_n - Z_s - \frac{2Z_s^2}{\sin\theta_n}}{\sin\theta_n + Z_s}\right)^{\frac{x}{d}\tan\theta_n} \\
&\approx \left(\frac{\sin\theta_n - Z_s}{\sin\theta_n + Z_s}\right)^{\frac{x}{d}\tan\theta_n} \\
&= [R_h(\theta_n)]^{\frac{x}{d}\tan\theta_n} \qquad (4.35)
\end{aligned}$$

$$\beta_n' = j\frac{\tan\theta_n}{d}\log[R_h(\theta_n)] \tag{4.36}$$

$$R_h(\theta_n) = \frac{\sin\theta_n - Z_s}{\sin\theta_n + Z_s} \tag{4.37}$$

where $R_h(\theta_n)$ is the hard reflection coefficient.

It is mentioned again that the expressions derived in this section for β_n' are valid only for the nearly perfectly conducting guide in which $|Y_s| \gg 1$ for the TE case and $|Z_s| \ll \pi/kd$ for the TM case.

4.2.2 Annular Waveguide

The method derived in the previous section for finding the perturbation to the propagation constants using the modal ray angles and reflection coefficients is now extended to the annular waveguide. Starting with the whispering gallery type mode, Figure 4.3 shows the geometry relevant to finding the perturbation ν_n'. Considering the modal ray form of the modes in this guide, it is seen that the crossing cylindrical waves reflect from the outer wall once every angular distance $2\theta_{an}$. Therefore, the

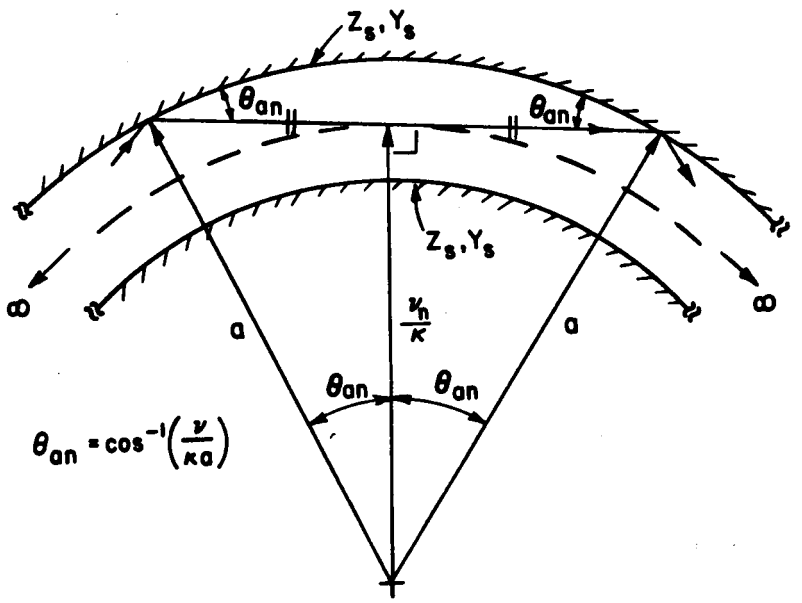

Figure 4.3: Geometry for finding the perturbation to the propagation constants in the annular waveguide, whispering gallery case.

perturbed ϕ-propagation term can be written for the TE case as

$$e^{-j\nu_n'\phi} = [-R_s(\theta_{an})]^{\frac{\phi}{2\theta_{an}}}. \tag{4.38}$$

Solving for ν_n' gives

$$\nu_n' = j\frac{1}{2\theta_{an}}\log[-R_s(\theta_{an})] \tag{4.39}$$

where the soft reflection coefficient R_s is given by (4.34). The TM case is found similarly as

$$\nu_n' = j\frac{1}{2\theta_{an}}\log[R_h(\theta_{an})] \tag{4.40}$$

where the hard reflection coefficient R_h is given by (4.37).

Figure 4.4 shows the geometry relevant for finding ν_n' for the non-whispering gallery type mode of the annular waveguide. It is seen that a modal ray undergoes one reflection each from the inner and outer walls for every angular distance $2(\theta_{an} - \theta_{bn})$. Therefore, the perturbed modal propagation in the ϕ-direction can be written for the TE case as

$$e^{-j\nu_n'\phi} = [R_s(\theta_{an})R_s(\theta_{bn})]^{\frac{\phi}{2(\theta_{an}-\theta_{bn})}}. \tag{4.41}$$

Solving for ν_n' gives for the TE case

$$\nu_n' = j\frac{1}{2(\theta_{an} - \theta_{bn})}\log[R_s(\theta_{an})R_s(\theta_{bn})] \tag{4.42}$$

and for the TM case

$$\nu_n' = j\frac{1}{2(\theta_{an} - \theta_{bn})}\log[R_h(\theta_{an})R_h(\theta_{bn})]. \tag{4.43}$$

Once again, it is emphasized that this derivation is valid only for nearly perfectly conducting waveguides with $|Y_s| \gg 1$ for the TE case and $|Z_s| \ll \pi/kd$ for the TM case.

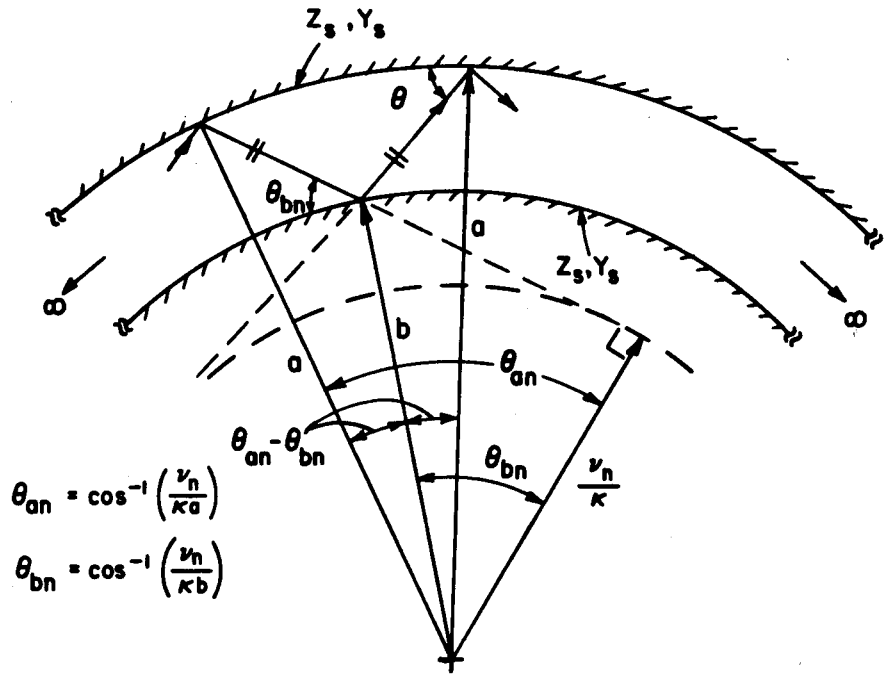

Figure 4.4: Geometry for finding the perturbation to the propagation constants of the annular waveguide, non-whispering gallery case.

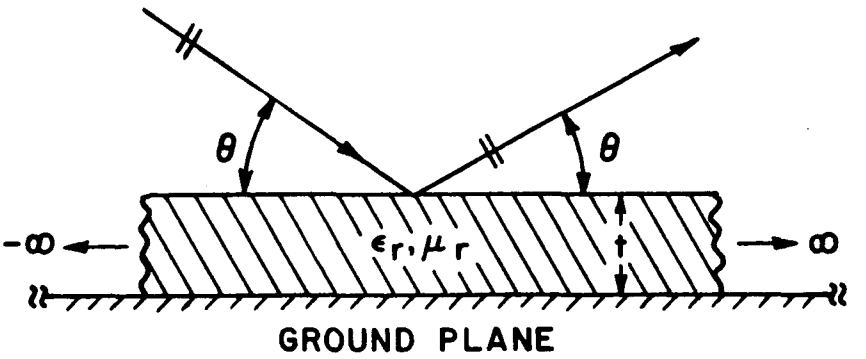

Figure 4.5: Plane wave reflection from a dieletric layer covering a perfectly conducting ground plane.

4.3 Equivalent Surface Impedance for a Thin Absorber Coating on a Perfectly Conducting Ground Plane

It will be shown in this section that a dielectric layer covering a perfectly conducting ground plane can be replaced by an equivalent surface impedance using the plane wave reflection coefficients for the two types of surfaces [8]. The equivalent surface impedance will in general be dependent on the incidence angle.

Figure 4.5 shows the geometry for this type of configuration with a plane wave incident at an angle θ. The soft (TE) reflection coefficient for the coated ground plane is given by

$$\Gamma_s(\theta) = \frac{\sin\theta - \frac{1}{j\mu_r}\sqrt{\epsilon_r\mu_r - \cos^2\theta}\cot(kt\sqrt{\epsilon_r\mu_r - \cos^2\theta})}{\sin\theta + \frac{1}{j\mu_r}\sqrt{\epsilon_r\mu_r - \cos^2\theta}\cot(kt\sqrt{\epsilon_r\mu_r - \cos^2\theta})} \tag{4.44}$$

where ϵ_r and μ_r are the relative (complex) permittivity and permeability, respectively, of the dielectric layer. The corresponding reflection coefficient for a surface

impedance is given as in (4.34) as

$$R_s(\theta) = \frac{\sin\theta - Y_s}{\sin\theta + Y_s} \tag{4.45}$$

where $Y_s = 1/Z_s$ is the surface admittance. Equating these two types of reflection coefficients it is seen that the equivalent surface admittance Y_s can be expressed as a function of ϵ_r, μ_r, θ, and kt:

$$Y_s = \frac{1}{j\mu_r}\sqrt{\epsilon_r\mu_r - \cos^2\theta}\cot(kt\sqrt{\epsilon_r\mu_r - \cos^2\theta}). \tag{4.46}$$

The "thin absorber coating" criterion is $kt|\sqrt{\epsilon_r\mu_r}| \ll 1$. This allows the small argument form of the cotangent function to be used which for the TE case gives

$$Y_s \approx \frac{1}{jkt\mu_r} \tag{4.47}$$

which eliminates the angular dependence of the equivalent surface admittance. It is seen that for small values of $kt\mu_r$, the surface admittance Y_s is large, satisfying the perturbational requirement of section 4.1.

For the TM case, the hard reflection coefficients of the dielectric layer covering the ground plane and a surface impedance are given by

$$\Gamma_h(\theta) = \frac{\sin\theta - \frac{j}{\epsilon_r}\sqrt{\epsilon_r\mu_r - \cos^2\theta}\tan(kt\sqrt{\epsilon_r\mu_r - \cos^2\theta})}{\sin\theta + \frac{j}{\epsilon_r}\sqrt{\epsilon_r\mu_r - \cos^2\theta}\tan(kt\sqrt{\epsilon_r\mu_r - \cos^2\theta})} \tag{4.48}$$

$$R_h(\theta) = \frac{\sin\theta - Z_s}{\sin\theta + Z_s}, \tag{4.49}$$

respectively, from which it is seen that the equivalent surface impedance can be expressed as

$$Z_s = \frac{j}{\epsilon_r}\sqrt{\epsilon_r\mu_r - \cos^2\theta}\tan(kt\sqrt{\epsilon_r\mu_r - \cos^2\theta}). \tag{4.50}$$

Again using the thin absorber coating criterion, the small argument form of the tangent function can be used which gives

$$Z_s \approx jkt(\mu_r - \frac{1}{\epsilon_r}\cos^2\theta). \tag{4.51}$$

It is seen again that the perturbation requirement of section 4.1 is met if $kt\mu_r$ is small enough to make Z_s small.

For the TM case, Z_s is not independent of incidence angle for the thin absorber coating case unless ϵ_r is large enough to make the second term of (4.51) negligable, but still small enough to satisfy the thin absorber coating criterion. If this additional approximation is made, then (4.51) is the same as (4.47) because $Y_s = 1/Z_s$.

4.4 Numerical Results Using the Hybrid Asymptotic Modal/Modal Perturbation Method

In this section backscatter results obtained using the hybrid modal technique with the perturbed propagation matrices will be presented in the form of backscatter vs. aspect angle plots for various inlet configurations. Emphasis will be placed on seeing the effects of offsetting the termination of a straight inlet with an S-bend. The parameters which will be varied are frequency, polarization, amount of loss in the absorber coating and the amount of offset. All of the cases in this section have a thin layer of absorber coating on the inner walls of the guide, except for the termination which is perfectly conducting.

Figure 4.6 shows the first two inlet geometries. Notice that the S-bend geometry has the same dimensions as the straight inlet with its termination offset one inlet width. The inlets will be analyzed at 10 and 35 GHz. At 10 GHz there are 6 propagating modes in the waveguide sections of these inlets and at 35 GHz there are 23. Figures 4.7 and 4.8 compare the calculated backscatter vs. aspect angle for the lossless straight inlet with measurements taken on a 3-dimensional rectangular inlet of the same planar dimensions. The 3-D inlet model was shaped so that scattering from the exterior termination was minimized. This scattering mechanism was not included in the calculation. The results agree quite well, considering one is in two

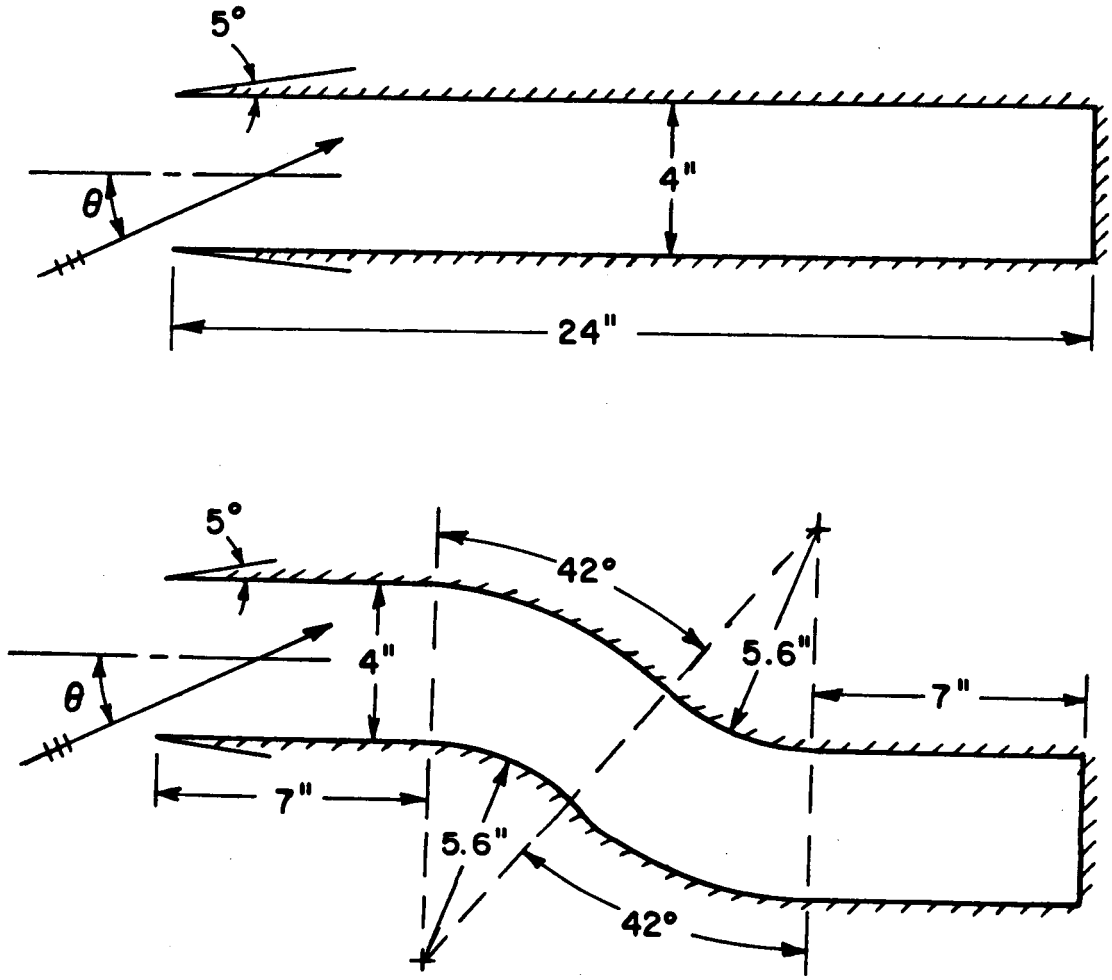

Figure 4.6: Straight and S-bend inlet geometries for numerical backscatter results.

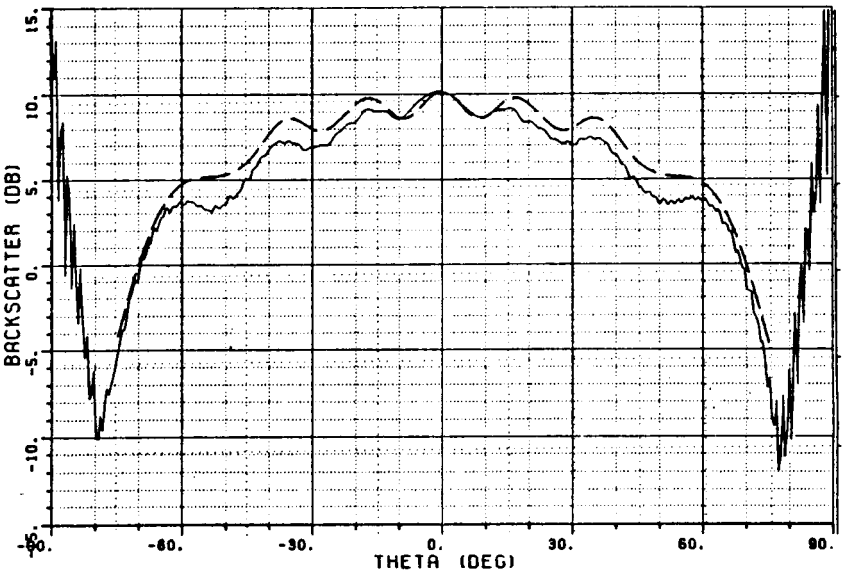

Figure 4.7: TE backscatter vs. aspect angle for the straight inlet at 10 GHz. — Measured, - - Calculated.

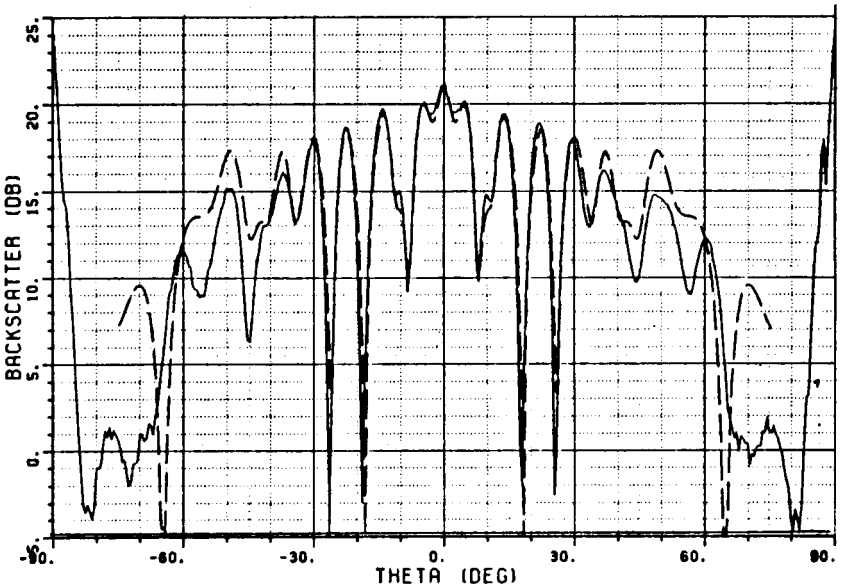

Figure 4.8: TE backscatter vs. angle for the straight inlet at 35 GHz. — Measured, - - Calculated.

dimensions and the other is in three.

In the remaining backscatter plots of this section, the perfectly conducting result (no absorber coating) will be plotted along with the lossy result and the backscatter due to only the open end. The amount of loss due to the absorber coating used is approximately 1 dB per reflection at normal incidence. In other words, the power density of a plane wave incident on a ground plane coated with this absorber is reduced by about 1 dB after reflection. The exact values of the coating parameters used here are as follows: At 10 GHz

$$t = .001 \text{ inches} \tag{4.52}$$

$$\epsilon_r = 10 - j5 \tag{4.53}$$

$$\mu_r = 5 - j10 \tag{4.54}$$

and at 35 GHz,

$$t = .001 \text{ inches} \tag{4.55}$$

$$\epsilon_r = 3 - j3 \tag{4.56}$$

$$\mu_r = 1 - j3. \tag{4.57}$$

These values give an equivalent surface admittance of $|Y_s| \approx 17$ for the TE case. Therefore, the perturbation requirement $|Y_s| \gg 1$ is fairly well satisfied for these absorber parameters. For the TM case, the equivalent surface impedance is $|Z_s| \approx .06$. π/kd is .148 at 10 GHz and .042 at 35 GHz. These values do not satisfiy the perturbation requirement $Z_s \ll \pi/kd$ very well for this case so the TM backscatter results for absorber coated ducts in this chapter are not expected to be very accurate.

Figures 4.9-4.16 show the backscatter vs. aspect angle results for the inlets of Figure 4.6 for the two frequencies and polarizations used. The plots show the general trend that the effect of the offset is to flatten out the backscatter pattern, removing the peak near the axis of the inlet where the termination would be directly

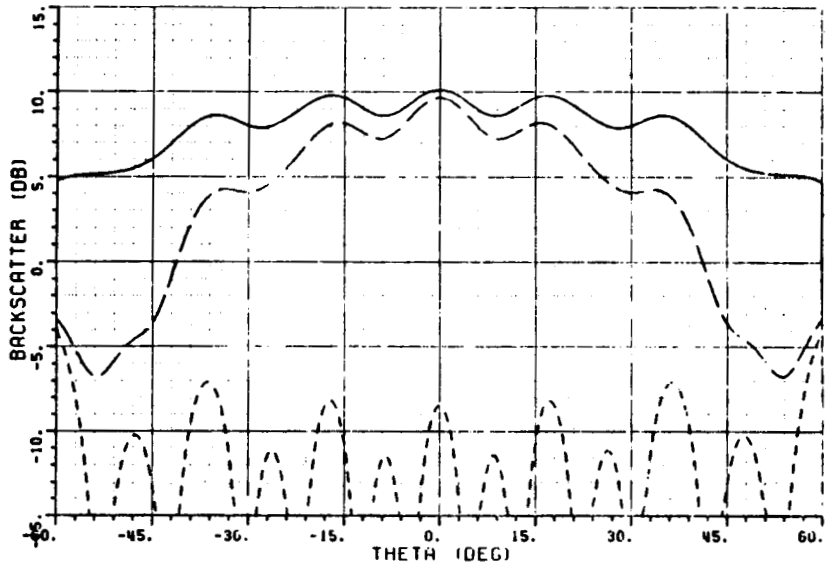

Figure 4.9: TE Backscatter vs. aspect angle for the straight inlet at 10 GHz. —- Lossless, – – 1 dB loss/refl., - - - Rim diffracted.

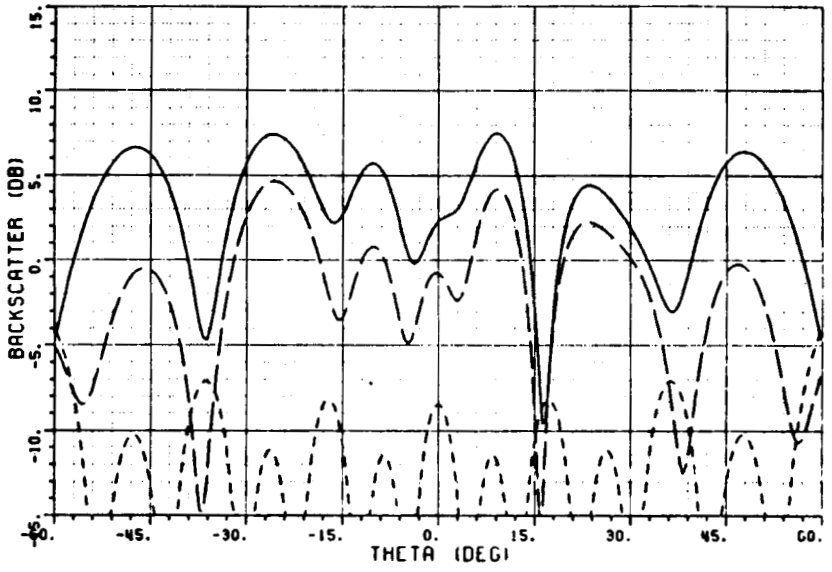

Figure 4.10: TE Backscatter vs. aspect angle for the S-bend inlet at 10 GHz. —- Lossless, – – 1 dB loss/refl., - - - Rim diffracted.

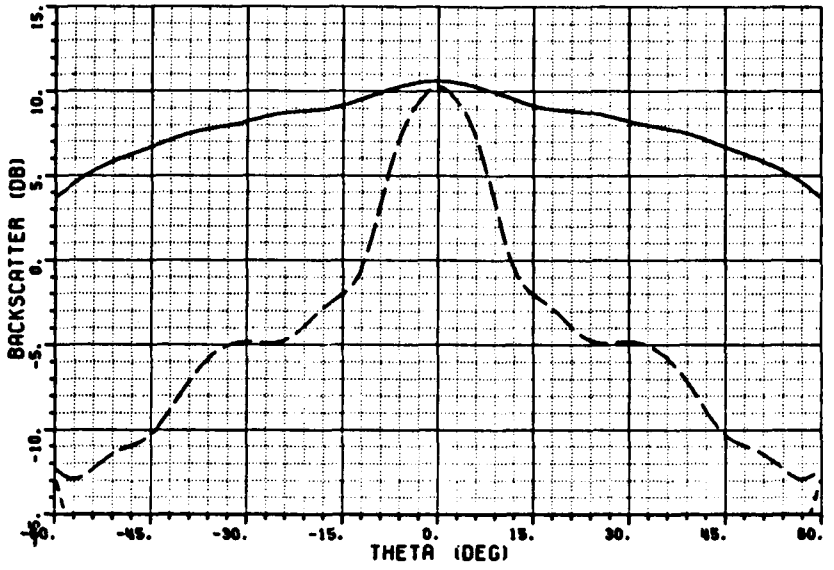

Figure 4.11: TM Backscatter vs. aspect angle for the straight inlet at 10 GHz. —- Lossless, – – 1 dB loss/refl., - - - Rim diffracted.

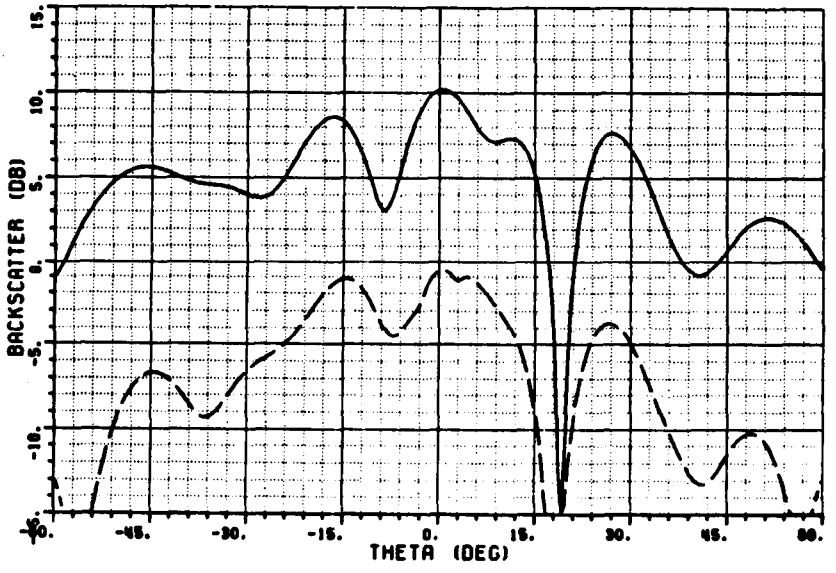

Figure 4.12: TM Backscatter vs. aspect angle for the S-bend inlet at 10 GHz. —- Lossless, – – 1 dB loss/refl., - - - Rim diffracted.

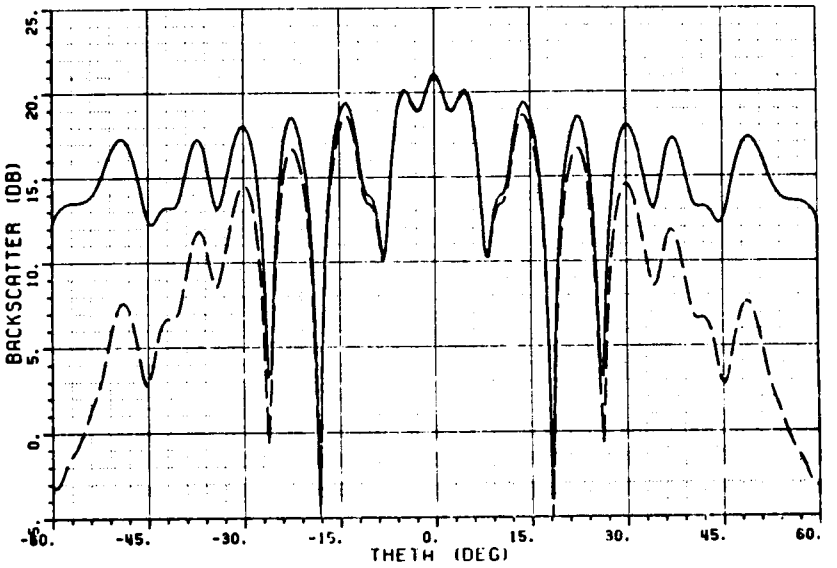

Figure 4.13: TE Backscatter vs. aspect angle for the straight inlet at 35 GHz. — Lossless, – – 1 dB loss/refl., - - - Rim diffracted.

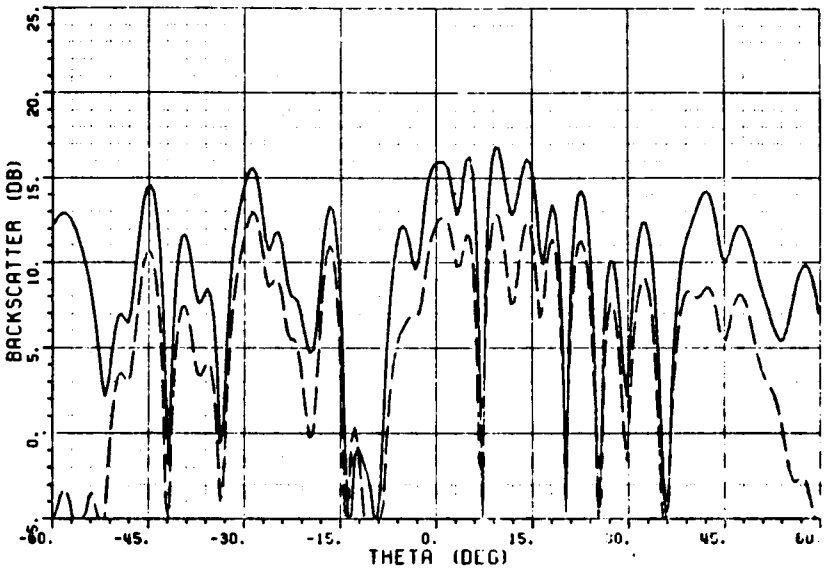

Figure 4.14: TE Backscatter vs. aspect angle for the S-bend inlet at 35 GHz. — Lossless, – – 1 dB loss/refl., - - - Rim diffracted.

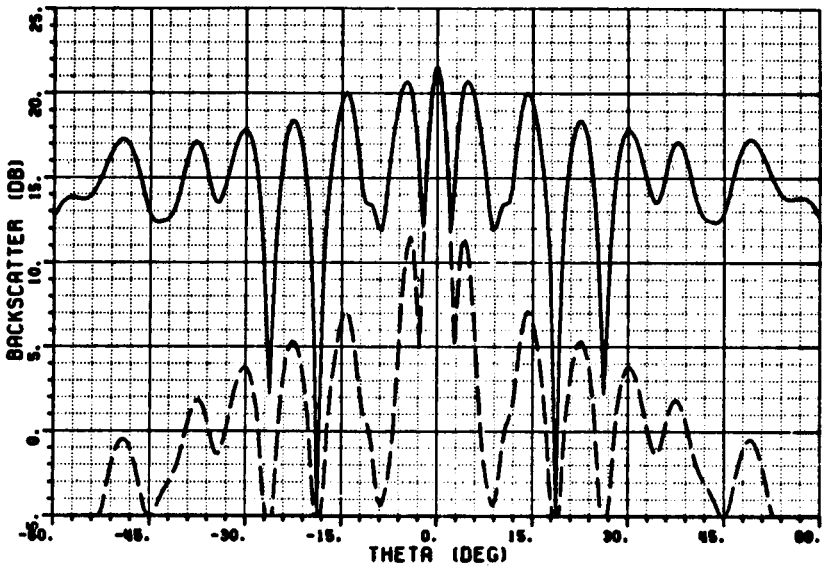

Figure 4.15: TM Backscatter vs. aspect angle for the straight inlet at 35 GHz. — Lossless, – – 1 dB loss/refl., - - - Rim diffracted.

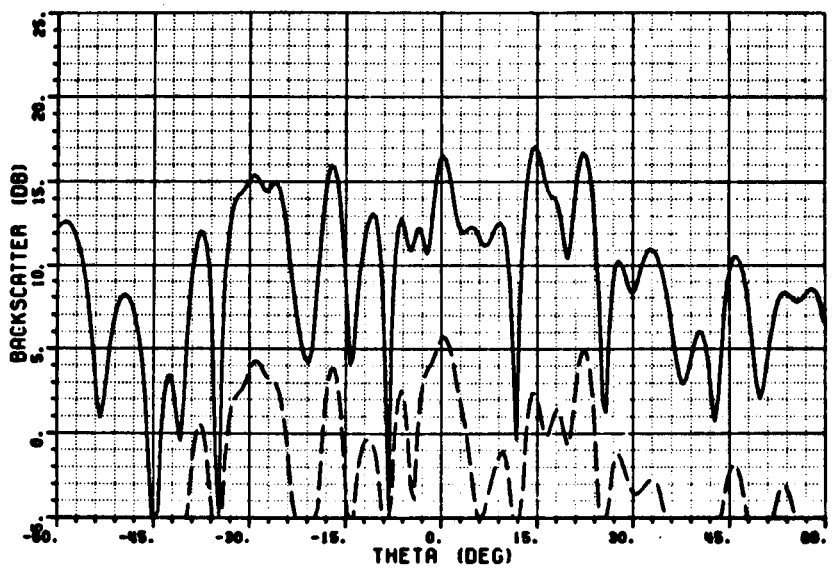

Figure 4.16: TM Backscatter vs. aspect angle for the S-bend inlet at 35 GHz. — Lossless, – – 1 dB loss/refl., - - - Rim diffracted.

visible for the straight inlet. The presence of the absorber coating further reduces the backscatter, however, it does not have much effect in the case of the straight inlet near the axis because the perfectly conducting termination is still directly visible.

It is noticed that for the 10 GHz, TM case, the S-bend does not have much of an effect on reducing the backscatter near the axis. This is because the TM polarization allows the TEM mode (zero mode angle) to propagate in both inlets and is the dominant power carrying mode near axial incidence. The S-bend will have little effect on this type of mode. Also, the aborber coating will have little effect on this mode because the E-field is normal to the guide walls. However, the TEM mode does not exist in more practical three-dimensional inlets, so this is only a two-dimensional effect.

To see if increasing the amount of offset that the S-bend introduces further reduces the backscatter pattern, the annular sections of the S-bend inlet of Figure 4.6 were increased from 42 to 50 degrees in angular extent. The backscatter results for this inlet appear in Figures 4.17-4.21. Comparing these results with those of Figures 4.10, 4.12, 4.14, and 4.16 it can be seen that increasing the amount of offset has little effect on the envelope of the backscatter pattern for the lossless cases but reduces further the pattern envelope for the absorber coated cases. This is expected because the interior coupled energy has to travel a longer distance inside the inlet. For the lossy case this means more attenuation is introduced by the absorber coating. However, for the lossless case this only changes the shape of the backscatter pattern because the coupled energy is redistributed but none is lost.

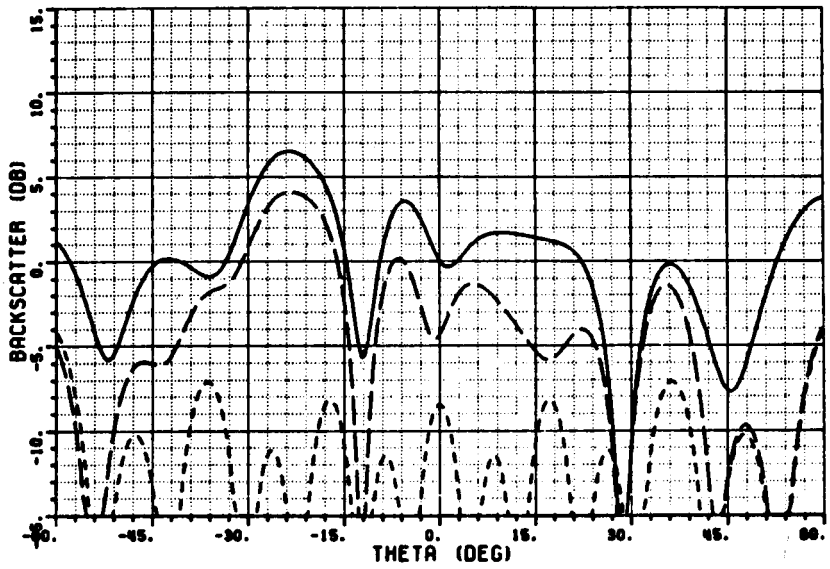

Figure 4.17: TE Backscatter vs. aspect angle for the extended S-bend inlet at 10 GHz. —- Lossless, – – 1 dB loss/refl., - - - Rim diffracted.

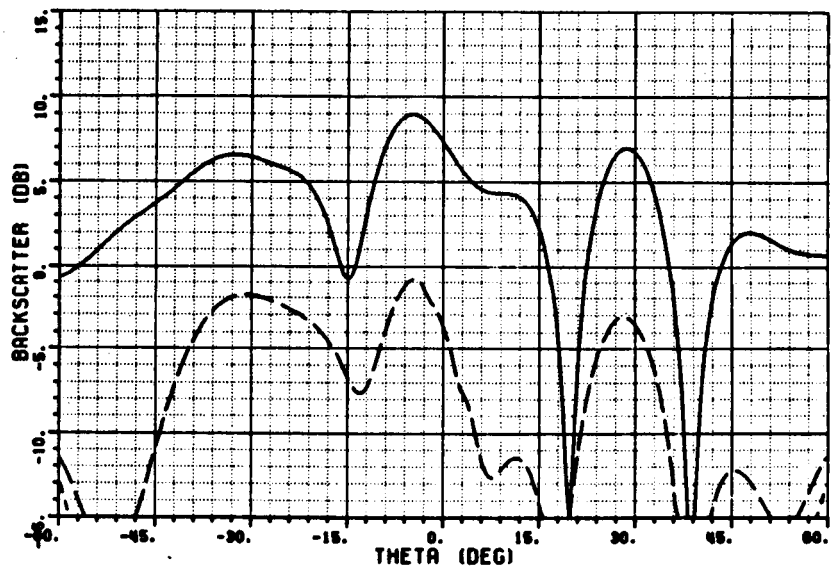

Figure 4.18: TM Backscatter vs. aspect angle for the extended S-bend inlet at 10 GHz. —- Lossless, – – 1 dB loss/refl., - - - Rim diffracted.

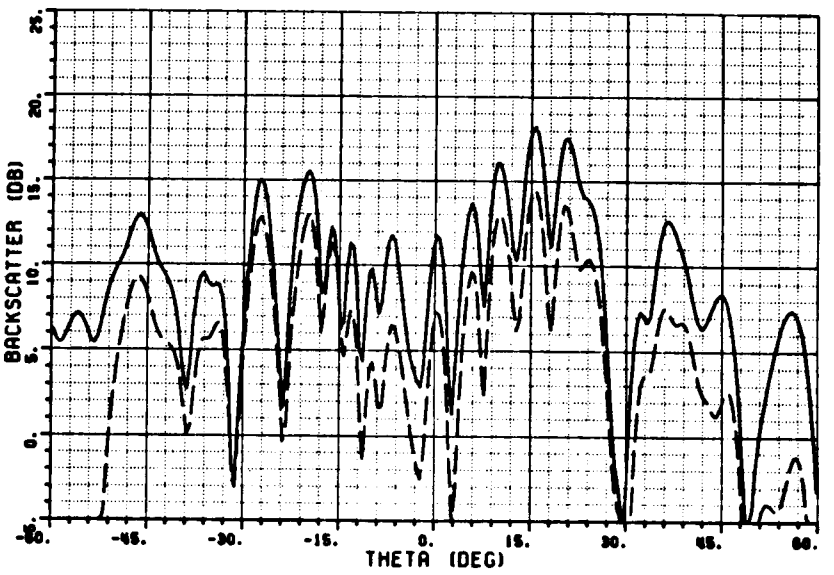

Figure 4.19: TE Backscatter vs. aspect angle for the extended S-bend inlet at 35 GHz. —- Lossless, – – 1 dB loss/refl., - - - Rim diffracted.

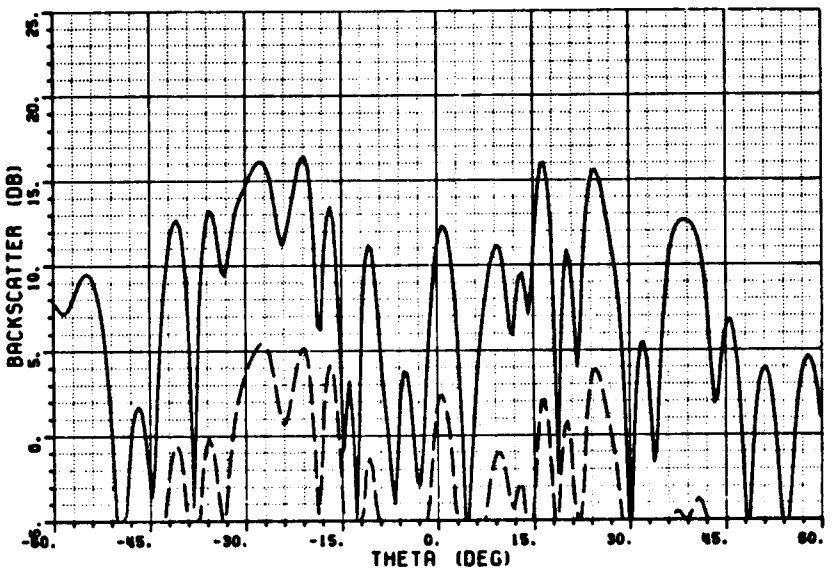

Figure 4.20: TM Backscatter vs. aspect angle for the extended S-bend inlet at 35 GHz. —- Lossless, – – 1 dB loss/refl., - - - Rim diffracted.

5. Integral Equation Solutions of Internal Wave Reflection and Transmission in an S-Shaped Waveguide

In this chapter, the internal wave reflection and transmission in an S-shaped waveguide geometry is solved using an integral equation numerical approach. This technique yields a formally rigorous solution, but is not very efficient in terms of computer time cost. Nevertheless, it provides a valuable check on the accuracy of other approximate and more efficiently obtained solutions such as the one constructed via a hybrid asymptotic modal/modal perturbation approach in Chapters 3 and 4.

Referring to Figure 5.1, the S-shaped waveguide consists of two flat and two circular sections. The waveguide wall has a normalized surface impedance Z. The second flat section may be semi-infinite in length or terminated at a finite distance with a normalized surface impedance Z_r. The waveguide width is a. The inner radius of the circular sections are b_1 and b_2, and their angular spans are Φ_1 and Φ_2. A waveguide mode is incident from the left in the first flat section. Integral equations will be set up for solving the aperture fields at the various junctions between the different sections. Once the aperture fields at the junctions are known, they can be used to calculate the reflected and transmitted modes.

In the following, presentations will be given for the TM case. But the results are also applicable to the TE case, if the impedance Z and Z_r are replaced with the corresponding admittances. The time convention $e^{j\omega t}$ is assumed and omitted in the formulations.

5.1 Field Representations for the Flat Sections

In a parallel-plate waveguide whose wall has a surface impedance Z normalized to the free space impedance, the field of a waveguide mode satisfies the homogeneous

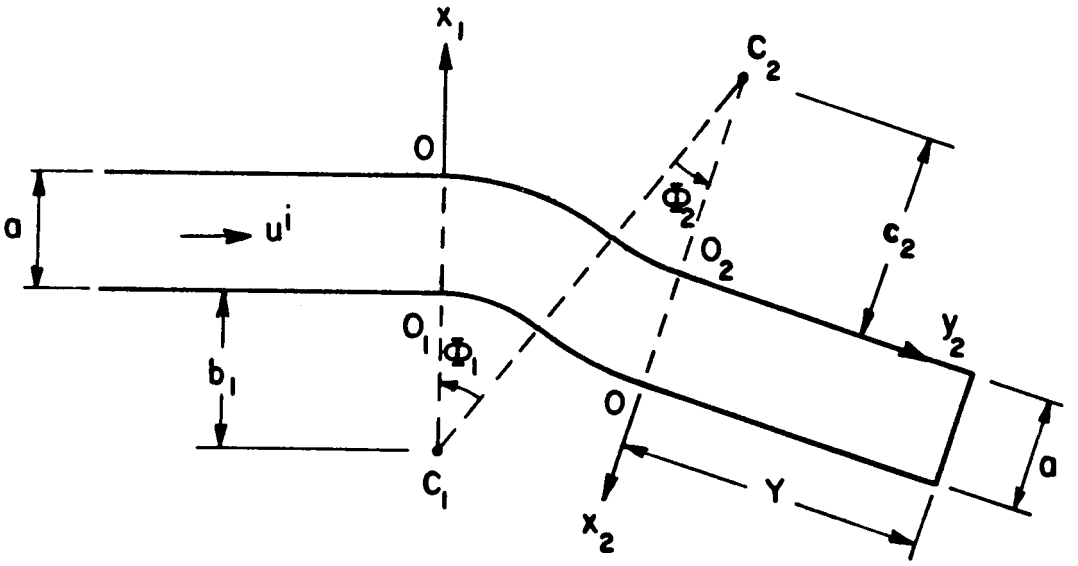

Figure 5.1: Waveguide geometry

wave equation

$$\left(\frac{\partial^2}{\partial x^2}+\frac{\partial^2}{\partial y^2}+k^2\right)G_n \;=\; 0,\; 0\le x\le a,\; -\infty<y<\infty, \tag{5.1}$$

and the boundary conditions

$$\begin{aligned}\frac{\partial G_n}{\partial x} &= jkZG_n,\ \text{at } x=0,\\ \frac{\partial G_n}{\partial x} &= -jkZG_n,\ \text{at } x=a,\end{aligned} \tag{5.2}$$

where k is the free space wavenumber. The solutions to (5.1) and (5.2) can be written in the form

$$G_n \;=\; N_n f_n(x) e^{\pm jk\sqrt{1-\beta_n^2}y}, \tag{5.3}$$

where

$$f_n(x) \;=\; e^{-jk\beta_n x}+\frac{\beta_n+Z}{\beta_n-Z}e^{jk\beta_n x} \tag{5.4}$$

and β_n are roots of the equation

$$\left(\frac{\beta_n + Z}{\beta_n - Z}\right)^2 - e^{-j2k\beta_n a} = 0. \tag{5.5}$$

The waveguide modal field (5.3) is normalized according to

$$\frac{\sqrt{1-\beta_n^2}}{a} N_n^2 \int_0^a [f_n(x)]^2 dx = 1, \tag{5.6}$$

such that

$$N_n = \left\{2\sqrt{1-\beta_n^2}\left[\frac{1-e^{-j2k\beta_n a}}{j2k\beta_n a} + \frac{\beta_n + Z}{\beta_n - Z}\right]\right\}^{-\frac{1}{2}}. \tag{5.7}$$

The functions $f_n(x)$ associated with different β_n are orthogonal, i.e.

$$\int_0^a f_n(x) f_m(x) dx = 0, \text{ if } n \neq m.$$

A waveguide mode of (5.3) is incident from the left in the first flat section of the S-shaped waveguide. The incident wave gives rise to reflected and transmitted waves. Therefore, the total field in the first flat section consists of the incident mode as well as some reflected modes.

Let $u(x_1, y_1)$ denote the total field (magnetic field in the TM case) where the argument (x_1, y_1) indicates the first flat section. $u(x_1, y_1)$ also satisfies (5.1) and (5.2). An expression for $u(x_1, y_1)$ will be derived with the use of Green's second identity. The desired Green's function is a solution to the inhomogeneous wave equation

$$\left(\frac{\partial^2}{\partial x^2} + \frac{\partial^2}{\partial y^2} + k^2\right) G(x, y; x', y') = -\delta(x - x')\delta(y - y'), \quad 0 \leq x \leq a,\ 0 \leq y < \infty, \tag{5.8}$$

satisfying the boundary conditions (5.2) together with $\partial G/\partial y|_{y=0} = 0$, and the radiation condition as $|y - y'| \to \infty$. Specifically,

$$G(x, y; x', y') = \sum_n \frac{N_n^2}{jka} f_n(x') f_n(x)$$

$$\cdot \cos(k\sqrt{1-\beta_n^2}y_<)e^{-jk\sqrt{1-\beta_n^2}y_>}, \tag{5.9}$$

where $y_<$ and $y_>$ denote, respectively, the smaller and larger of y' and y. Applying Green's second identity to $u(x_1, y_1)$ and $G(x_1, y_1; x_1', y_1')$ in the first flat section yields

$$\begin{aligned} u(x_1, y_1) &= 2N_i f_i(x_1)\cos(k\sqrt{1-\beta_i^2}y_1) \\ &\quad - \sum_n \frac{N_n^2}{jka}\left[\int_0^a f_n(x_1')\left.\frac{\partial u(x_1', y_1')}{\partial y_1'}\right|_{y_1'=0} dx_1'\right] \\ &\quad \cdot f_n(x_1)e^{-jk\sqrt{1-\beta_n^2}y_1}, \end{aligned} \tag{5.10}$$

where the subscript i is the index number of the incident mode.

The same procedure can be readily applied to obtain an expression for the total field $u(x_2, y_2)$ in the second flat section,

$$\begin{aligned} u(x_2, y_2) &= -\sum_n \frac{N_n^2}{jka}\frac{1 - R_n e^{j2k\sqrt{1-\beta_n^2}y_2}}{1+R_n} \\ &\quad \cdot \left[\int_0^a f_n(x_2')\left.\frac{\partial u(x_2', y_2')}{\partial y_2'}\right|_{y_2'=0} dx_2'\right] f_n(x_2)e^{-jk\sqrt{1-\beta_n^2}y_2}, \end{aligned} \tag{5.11}$$

where $R_n = 0$ if the second flat section is semi-infinite, and

$$R_n = \frac{Z_r - \sqrt{1-\beta_n^2}}{Z_r + \sqrt{1-\beta_n^2}}e^{-j2k\sqrt{1-\beta_n^2}r},$$

if the second flat section is terminated with a surface impedance Z_r (normalized to the free space impedance) at a distance r from the junction between the second flat and curved sections.

and the boundary conditions

$$\begin{aligned}
\frac{\partial G}{\partial \rho} &= jkZG, \text{ at } \rho = b, \\
\frac{\partial G}{\partial \rho} &= -jkZG, \text{ at } \rho = b + a, \\
\frac{\partial G}{\partial \phi} &= 0, \text{ at } \phi = 0, \text{ and } \phi = \Phi.
\end{aligned} \tag{5.13}$$

The solution for $G(\rho, \phi; \rho', \phi')$ is

$$G(\rho, \phi; \rho', \phi') = \sum_{\nu} \frac{\pi}{\Phi} g_{\nu}(\rho_<, \rho_>) \cos(\nu\phi') \cos(\nu\phi), \tag{5.14}$$

where

$$\begin{aligned}
\nu &= \frac{P\pi}{\Phi}, \; P = \text{an integer}, \\
g_{\nu}(\rho_<, \rho_>) &= \frac{[D_{\nu} J_{\nu}(k\rho_<) - B_{\nu} N_{\nu}(k\rho_<)]\,[C_{\nu} J_{\nu}(k\rho_>) - A_{\nu} N_{\nu}(k\rho_>)]}{\epsilon_{0\nu}(A_{\nu} D_{\nu} - B_{\nu} C_{\nu})} \\
J_{\nu}, N_{\nu} &= \text{Bessel and Neuman functions}, \\
J'_{\nu}, N'_{\nu} &= \text{derivatives of } J_{\nu} \text{ and } N_{\nu} \text{ w.r.t. the argument}, \\
\rho_<, \rho_> &= \text{the smaller and larger of } \rho \text{ and } \rho', \\
A_{\nu} &= J'_{\nu}(kb + ka) + jZJ_{\nu}(kb + ka) \\
B_{\nu} &= J'_{\nu}(kb) - jZJ_{\nu}(kb) \\
C_{\nu} &= N'_{\nu}(kb + ka) + jZJ_{\nu}(kb + ka) \\
D_{\nu} &= N'_{\nu}(kb) - jZN_{\nu}(kb) \\
\epsilon_{0\nu} &= \begin{cases} 2, & \text{if } \nu = 0 \\ 1, & \text{if } \nu > 0 \end{cases}.
\end{aligned}$$

Now, applying Green's second identity to $G(\rho, \phi; \rho', \phi')$ and $u(\rho, \phi)$, which satisfies the homogeneous wave equation

$$\begin{aligned}
\left[\frac{1}{\rho}\frac{\partial}{\partial \rho}\left(\rho\frac{\partial}{\partial \rho}\right) + \frac{1}{\rho^2}\frac{\partial^2}{\partial \phi^2} + k^2\right] u(\rho, \phi) &= 0, \\
0 \le \phi \le \Phi, \; b \le \rho \le b + a,
\end{aligned} \tag{5.15}$$

and the boundary conditions

$$\begin{aligned} \frac{\partial u}{\partial \rho} &= jkZu, \text{ at } \rho = b, \\ \frac{\partial u}{\partial \rho} &= -jkZu, \text{ at } \rho = b + a, \end{aligned} \tag{5.16}$$

yields an expression for $u(\rho, \phi)$,

$$\begin{aligned} u(\rho, \phi) = \sum_{\nu} \frac{\pi}{\Phi} \cos(\nu\phi) \int_b^{b+a} g_\nu(\rho_<, \\ \cdot \rho_>) \left[(-1)^P \left. \frac{\partial u(\rho', \phi')}{\rho' \partial \phi'} \right|_{\phi'=\Phi} - \left. \frac{\partial u(\rho', \phi')}{\rho' \partial \phi'} \right|_{\phi'=0} \right] d\rho'. \end{aligned} \tag{5.17}$$

One may attach a subscript 1 or 2 to the various variables in (5.17) to signify either one of the two circular sections.

5.3 Integral Equations for the Unknown Aperture Fields

One may set up integral equations for solving the unknown aperture field quantities $\partial u/\partial y$ (or $\partial u/\partial \phi$) at the junctions from (5.10), (5.11), and (5.17), by imposing the following boundary conditions

$$\begin{aligned} \left. \frac{\partial u(x_1, y_1)}{\partial y_1} \right|_{y_1=0} &= \left. \frac{\partial u(\rho_1, \phi_1)}{\rho_1 \partial \phi_1} \right|_{\phi_1=\Phi_1} = M_1(x_1) = M_1(\rho_1), \\ \left. \frac{\partial u(x_2, y_2)}{\partial y_2} \right|_{y_2=0} &= \left. \frac{\partial u(\rho_2, \phi_2)}{\rho_2 \partial \phi_2} \right|_{\phi_2=\Phi_2} = -M_2(x_2) = -M_2(\rho_2), \\ \left. \frac{\partial u(\rho_1, \phi_1)}{\rho_1 \partial \phi_1} \right|_{\phi_1=0} &= -\left. \frac{\partial u(\rho_2, \phi_2)}{\rho_2 \partial \phi_2} \right|_{\phi_2=0} = M_3(\rho_1) = M_3(\rho_2), \end{aligned} \tag{5.18}$$

and

$$\begin{aligned} u(x_1, y_1)|_{y_1=0} &= u(\rho_1, \phi_1)|_{\phi_1=\Phi_1}, \\ u(x_2, y_2)|_{y_2=0} &= u(\rho_2, \phi_2)|_{\phi_2=\Phi_2}, \\ u(\rho_1, \phi_1)|_{\phi_1=0} &= u(\rho_2, \phi_2)|_{\phi_2=0}. \end{aligned} \tag{5.19}$$

The integral equations are

$$\sum_n \frac{N_n^2}{jka} f_n(x_1) \int_0^a f_n(x_1) M_1(x_1') dx_1'$$

$$+ \sum_\nu \frac{\pi}{\Phi_1} \int_b^{b+a} g_\nu(\rho_<, \rho_>) \left[M_1(\rho_1') - (-1)^P M_3(\rho_1') \right] d\rho_1' = 2N_i f_i(x_1), \quad (5.20)$$

$$\sum_\nu \frac{\pi}{\Phi_1} \int_b^{b+a} g_\nu(\rho_<, \rho_>) \left[(-1)^P M_1(\rho_1') - M_3(\rho_1') \right] d\rho_1'$$

$$+ \sum_\nu \frac{\pi}{\Phi_2} \int_b^{b+a} g_\nu(\rho_<, \rho_>) \left[(-1)^P M_2(\rho_2') - M_3(\rho_2') \right] d\rho_2' = 0, \quad (5.21)$$

$$\sum_n \frac{N_n^2}{jka} \frac{1 - R_n}{1 + R_n} f_n(x_2) \int_0^a f_n(x_2') M_2(x_2') dx_2'$$

$$+ \sum_\nu \frac{\pi}{\Phi_2} \int_b^{b+a} g_\nu(\rho_<, \rho_>) \left[M_2(\rho_2') - (-1)^P M_3(\rho_2') \right] d\rho_2' = 0. \quad (5.22)$$

Note that for simplicity, the subscripts 1 and 2, which distinguish terms in the two circular sections, are omitted from some of the variables under the summation $\sum_\nu$ in (5.20)-(5.22).

The integral equations (5.20) - (5.22) will be solved by the moment method. Using the substitutions

$$\begin{aligned}
M_1(x_1) &= \sum_n^N U_n k f_n(x_1) \\
M_1(\rho_1) &= \sum_n^N U_n k f_n(\rho_1 - b) \\
M_2(x_2) &= \sum_n^N V_n k f_n(x_2) \\
M_2(\rho_2) &= \sum_n^N V_n k f_n(\rho_2 - b) \\
M_3(\rho_1) &= \sum_n^N W_n k f_n(\rho_1 - b) \\
M_3(\rho_2) &= \sum_n^N W_n k f_n(a + b - \rho_2), \quad (5.23)
\end{aligned}$$

where U_n, V_n and W_n are unknown constants, multiplying (5.20)-(5.22) by $k f_m(x)$,

and integrating the resulting equations from $x = 0$ to $x = a$, one obtains

$$\frac{ka}{j(1-\beta_m^2)N_m^2}U_m + \sum_n^N (U_n Y_{1mn}^e - W_n Y_{1mn}^o) = \frac{2ka}{\sqrt{1-\beta_i^2}N_i}\delta_{mi}, \tag{5.24}$$

$$\sum_n^N (U_n Y_{1mn}^o - W_n Y_{1mn}^e) + \frac{\beta_m + Z}{\beta_m - Z}e^{jk\beta_m a}\sum_n^N (V_n Y_{2mn}^o - W_n Y_{2mn}^e) = 0, \tag{5.25}$$

$$\frac{1-R_m}{1+R_m}\frac{ka}{j(1-\beta_m^2)N_m^2}V_m + \sum_n^N \left(V_n Y_{2mn}^e - W_n Y_{2mn}^o \frac{\beta_n + Z}{\beta_n - Z}e^{jk\beta_n a}\right) = 0, \quad m = 1, 2, ..., N, \tag{5.26}$$

where

$$\begin{aligned} Y_{qmn}^e &= \int_0^a k dx f_m(x) \int_0^a k dx' f_n(x') \sum_\nu \frac{\pi}{\Phi_q} g_\nu(b + x_<, b + x_>), \\ Y_{qmn}^o &= \int_0^a k dx f_m(x) \int_0^a k dx' f_n(x') \sum_\nu \frac{\pi}{\Phi_q}(-1)^P g_\nu(b + x_<, b + x_>), \\ & \quad q = 1, 2. \end{aligned} \tag{5.27}$$

In sum, there are $3N$ linear equations which can be solved for the unknown U_n, V_n and W_n.

Using the substitutions given in (5.23), the reflected waves in the first flat section can now be written as

$$\begin{aligned} u^r(x_1, y_1) &= N_i f_i(x_1) e^{-jk\sqrt{1-\beta_i^2}y_1} \\ &\quad - \sum_n^N \frac{U_n}{j\sqrt{1-\beta_n^2}N_n} N_n f_n(x_1) e^{-jk\sqrt{1-\beta_n^2}y}. \end{aligned} \tag{5.28}$$

Numerical examples of the reflection coefficients associated with (5.28) are given next.

5.4 Numerical Results

The integral equation technique presented in this chapter is not efficient in terms of the computer time cost. The primary reason is due to the fact that the series

in the field representation for the circular section given in (5.17) converges very slowly[1]. For instance, in the following examples, 12 terms are retained in the series representation for the fields in the flat sections given in (5.10) and (5.11), in contrast to about 200 terms retained in the series of (5.17). Nevertheless, as pointed out earlier, this formally exact solution is presented mostly to check the accuracy of the perturbed hybrid approach of Chapter 4.

Table 1 lists the reflection coefficients R_{nm} for the waveguide geometry specifications: $a = 3.386667\lambda$, $b_1 = b_2 = 4.766733\lambda$, $\Phi_1 = \Phi_2 = 45°$, $Y = 5.046133\lambda$, $Z = Z_r = 0$, TM case. MM denotes the moment method solution of this chapter and HM denotes the hybrid solution of chapters 2, 3 and 4.

[1]The computer program for computing Bessel and Neuman functions of fractional orders was supplied by Prof. J.H. Richmond.

TABLE 1

nm		R_{nm} (MM)	R_{nm} (HM)
1	1	0.644 ∠45.8°	0.649 ∠42.9°
1	2	0.253 ∠68.9°	0.246 ∠65.4°
1	3	0.262 ∠-144.4°	0.257 ∠-148.0°
1	4	0.576 ∠-20.4°	0.578 ∠-23.6°
1	5	0.095 ∠-59.6°	0.099 ∠-59.6°
1	6	0.280 ∠-0.6°	0.283 ∠-3.2°
1	7	0.182 ∠-16.0°	0.172 ∠-16.7°
2	2	0.880 ∠-173.6°	0.885 ∠-177.1°
2	3	0.158 ∠-116.0°	0.141 ∠114.9°
2	4	0.218 ∠-117.2°	0.217 ∠-120.6°
2	5	0.054 ∠146.3°	0.056 ∠141.6°
2	6	0.209 ∠-100.0°	0.204 ∠-103.9°
2	7	0.206 ∠-123.9°	0.217 ∠-127.0°
3	3	0.658 ∠175.5°	0.660 ∠172.2°
3	4	0.187 ∠179.1°	0.187 ∠178.3°
3	5	0.571 ∠-3.7°	0.564 ∠-6.9°
3	6	0.342 ∠37.3°	0.347 ∠35.4°
3	7	0.088 ∠-96.3°	0.083 ∠-98.7°
4	4	0.725 ∠92.7°	0.723 ∠90.0°
4	5	0.151 ∠179.7°	0.155 ∠177.0°
4	6	0.150 ∠17.2°	0.158 ∠17.2°
4	7	0.119 ∠-110.1°	0.117 ∠-115.0°
5	5	0.383 ∠37.6°	0.392 ∠34.3°
5	6	0.691 ∠-10.6°	0.684 ∠-12.6°
5	7	0.165 ∠-56.5°	0.153 ∠-59.2°
6	6	0.472 ∠166.3°	0.486 ∠164.7°
6	7	0.197 ∠2.1°	0.182 ∠-0.9°
7	7	0.915 ∠107.1°	0.914 ∠104.3°

The reflection coefficients for the same waveguide geometry but with the TE polarization are listed in Table 2.

TABLE 2

nm		R_{nm} (MM)	R_{nm} (HM)
1	1	0.722 ∠51.8°	0.716 ∠50.6°
1	2	0.296 ∠94.1°	0.288 ∠94.4°
1	3	0.409 ∠96.7°	0.505 ∠92.6°
1	4	0.237 ∠-135.3°	0.248 ∠-138.0°
1	5	0.266 ∠96.9°	0.265 ∠91.7°
1	6	0.127 ∠113.8°	0.130 ∠109.9°
2	2	0.552 ∠-109.4°	0.543∠115.0°
2	3	0.339 ∠-24°	0.355 ∠-29.9°
2	4	0.591 ∠-123.1°	0.586 ∠-126.3°
2	5	0.337 ∠-21.5°	0.349 ∠-25.1°
2	6	0.174 ∠-23.3°	0.171 ∠-27.9°
3	3	0.515 ∠-47.3°	0.489 ∠-52.6°
3	4	0.435 ∠95.9°	0.426 ∠92.4°
3	5	0.368 ∠158.4°	0.372∠155.5°
3	6	0.219 ∠64.9°	0.222 ∠61.8°
4	4	0.477 ∠119.1°	0.501∠118.3°
4	5	0.384 ∠93.1°	0.359 ∠87.2°
4	6	0.177 ∠91.4°	0.179 ∠90.6°
5	5	0.723 ∠-36.3°	0.727∠-40.6°
5	6	0.104 ∠116.5°	0.101∠113.9°
6	6	0.929 ∠-88.1°	0.927∠-90.8°

Two examples of the reflection coefficients for the waveguide geometry with impedance wall are given in Tables 3 and 4. The geometry specifications are: $a = 3.386667\lambda$, $b_1 = b_2 = 4.766733\lambda$, $\Phi_1 = \Phi_2 = 42°$, $Y = 5.842\lambda$, $Z_r = 0$, $Z = 0.0532 + j0.0266$, TM case in Table 3 and TE case in Table 4.

TABLE 3

nm		R_{nm} (MM)	R_{nm} (HM)
1	1	0.324 ∠-19.0°	0.319 ∠-17.4°
1	2	0.113 ∠-35.8°	0.088 ∠-58.2°
1	3	0.064 ∠25.4°	0.044 ∠-72.9°
1	4	0.057 ∠-143.9°	0.058 ∠-119.7°
1	5	0.130 ∠118.6°	0.115 ∠110.6°
1	6	0.020 ∠66.5°	0.029 ∠64.9°
1	7	0.007 ∠-79.9°	0.006∠-62.4°
2	2	0.012 ∠169.7°	0.049∠150.5°
2	3	0.303 ∠44.7°	0.284 ∠43.8°
2	4	0.042 ∠-163.9°	0.041∠119.5°
2	5	0.178 ∠88.2°	0.191 ∠79.3°
2	6	0.067 ∠98.9°	0.076 ∠89.1°
2	7	0.007 ∠102.8°	0.013∠85.9°
3	3	0.249 ∠67.4°	0.267 ∠55.3°
3	4	0.108 ∠-141.1°	0.49∠-153.5°
3	5	0.194 ∠-140.3°	0.179∠-140.6°
3	6	0.019 ∠155.3°	0.041 ∠-166.6°
3	7	0.028 ∠-0.8°	0.026 ∠-2.2°
4	4	0.385 ∠7.8°	0.406 ∠6.0°
4	5	0.104 ∠-172.5°	0.093∠-175.8°
4	6	0.008 ∠130.7°	0.049 ∠-162.0°
4	7	0.004 ∠69.3°	0.013 ∠47.9°
5	5	0.130 ∠64.2°	0.127 ∠79.6°
5	6	0.190 ∠175.2°	0.269∠172.6°
5	7	0.055 ∠89.4°	0.061 ∠84.4°
6	6	0.221 ∠57.6°	0.329 ∠61.9°
6	7	0.012 ∠-71.7°	0.015∠-88.5°
7	7	0.144 ∠13.1°	0.137 ∠11.6°

TABLE 4

nm		R_{nm} (MM)	R_{nm} (HM)
1	1	0.450 ∠39.0°	0.479 ∠42.7°
1	2	0.120 ∠-74.7°	0.149 ∠-68.5°
1	3	0.368 ∠57.4°	0.364 ∠54.6°
1	4	0.120 ∠154.2°	0.105 ∠152.5°
1	5	0.065 ∠-12.3°	0.074 ∠-6.0°
1	6	0.028 ∠-153.7°	0.016∠162.8°
2	2	0.451 ∠-150.4°	0.476∠-146.7°
2	3	0.288 ∠148.2°	0.264 ∠152.7°
2	4	0.370 ∠160.7°	0.386 ∠155.7°
2	5	0.197 ∠-84.0°	0.195 ∠-86.2°
2	6	0.089 ∠-174.3°	0.080∠-172.5°
3	3	0.612 ∠-127.5°	0.584∠-130.4°
3	4	0.234 ∠11.1°	0.243 ∠18.5°
3	5	0.052 ∠-18.4°	0.057∠-36.2°
3	6	0.036 ∠-138.2°	0.030∠-140.2°
4	4	0.569 ∠-72.6°	0.583 ∠-69.1°
4	5	0.153 ∠-42.9°	0.184 ∠-52.4°
4	6	0.078 ∠-85.8°	0.067 ∠-83.9°
5	5	0.705 ∠171.2°	0.707∠171.3°
5	6	0.088 ∠38.6°	0.075 ∠37.4°
6	6	0.249 ∠-165.6°	0.238∠-159.2°

Note that for the TE case, the appropriate corresponding admittance must be substituted for Z and Z_r. As the above comparisons show, the more efficient hybrid asymptotic modal/modal perturbation method closely approximates the formally exact moment method solution.

6. Alternative Solution for the Scattered Field Using the Geometrical Optics Ray Approach

In this chapter the electromagnetic backscatter from the inlet of Figure 1.1 is calculated using the geometrical optics ray technique. The geometrical optics (GO) field incident on the inlet opening is partly scattered in the exterior region by the edges at the open end as $\vec{U}^{edge}$ and the rest is coupled into the inlet. Only the incident rays which directly enter into the inlet are included; the remaining contribution to the fields coupled into the inlet via diffraction of the incident field by the edges at the open end is ignored. The incident rays which enter into the inlet undergo multiple reflections from the interior walls of the inlet. These GO rays which are multiply reflected from the interior walls of the inlet propagate toward the termination at the rear of the inlet and then bounce back via additional reflections at the walls to provide a GO based field representation in the aperture at the open end. Further wave interactions between the open front end and the rear termination are ignored because these are weaker. The field $\vec{U}_{cav}$ which is essentially produced by the radiation into the exterior space from the above mentioned GO based field in the aperture at the open end, is found as usual via the aperture integration (AI) technique [11,12]. This aperture integration is done exactly the same way as in chapter 3 using equation (3.47). The difference is that now $\vec{U}^{ap}$ is based on the GO field in the aperture at the open end rather than the modal field of equation (3.48). The advantage of this method is that although not as accurate as the other methods discussed earlier, it can handle inlets of arbitrary shape and absorber coating, rather than ones that are made up of uniform waveguide sections and have thin absorber coatings. Also, as mentioned breifly in chaper 2, the hybrid asymptotic modal method becomes increasingly cumbersome as the guide width becomes large. The GO/AI method actually improves in accuracy for those cases. On the other hand, the GO/AI method can also become inefficient and cumbersome for inlets because

of the large number of rays to be tracked. The main reason for any inaccuracies in this GO/AI approach is because it does not include any effects of diffraction that enter within the duct and other higher order effects. The latter include the junction and aperture reflections considered in chapter 2. The GO/AI method of analysis is presented here for comparison purposes and to supply an alternative procedure for analyzing the scattering from inlet cavities, especially at higher frequencies where the modal method may become too inefficient and for more lossy absorber coatings for which the modal perturbation technique is not valid. Again, U stands for the $\hat{z}$-component of the E-field for the TE case and the $\hat{z}$-component of the H-field for the TM case.

6.1 Tracking the GO Ray Field

The GO field is found by breaking up the incident plane wave which enters the inlet into N collimated beams of equal width, as shown in Figure 6.1. These smaller columnated beams or ray tubes are traced through the inlet via the rear termination until they are about to exit through the aperture, as shown in Figure 6.2. Actually, only the two rays which form the boundaries of the smaller ray tubes are traced. The contribution of each ray tube to the aperture integral is found by breaking up the AI equation of Appendix E into a summation of sub-apertures formed by each of the exiting ray tubes in the aperture.

$$\vec{U}^{cav} = \sqrt{\frac{jk}{2\pi}}\cos\theta\frac{e^{-jk\rho}}{\sqrt{\rho}}\sum_{n=1}^{N}\int_{y_n}^{y_{n+1}}\vec{U}_n^{ap}(y)e^{-jky\sin\theta}dy \tag{6.1}$$

where each integral in the summation represents the contribution to the field scattered by the interior cavity effects arising from each ray tube. It is easy to show that the two terms of (E.6) and (E.12) are the same for this formulation which is why (6.1) has only one term. Figure 6.3 shows the relevant geometry pertaining to the limits y_n and y_{n+1} which occur in the integrals of this summation. The y_n and y_{n+1} shown are found from ray-tracing. Notice that because the ray tube undergoes

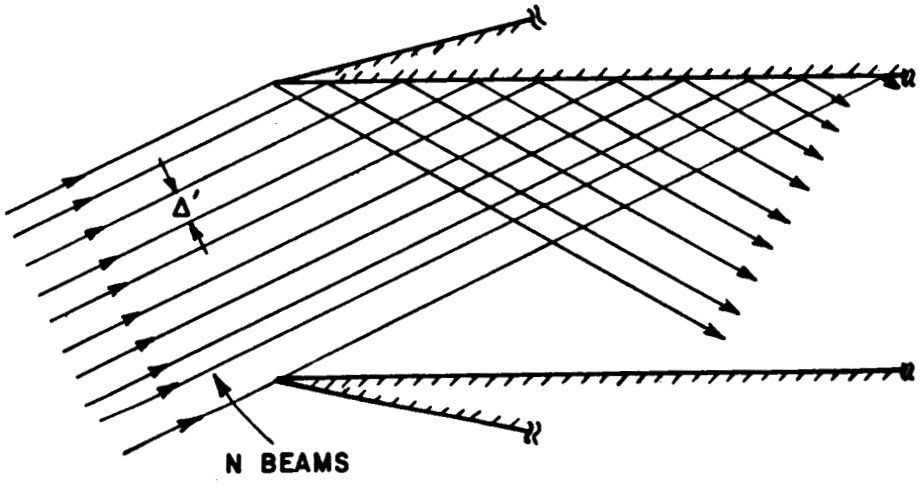

Figure 6.1: Incident plane wave divided into N columnated beams of width Δ'.

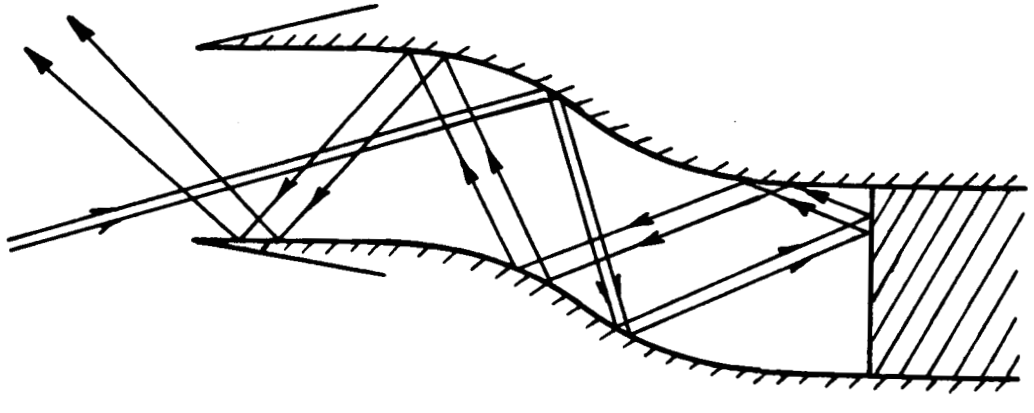

Figure 6.2: Ray tube traced through an inlet.

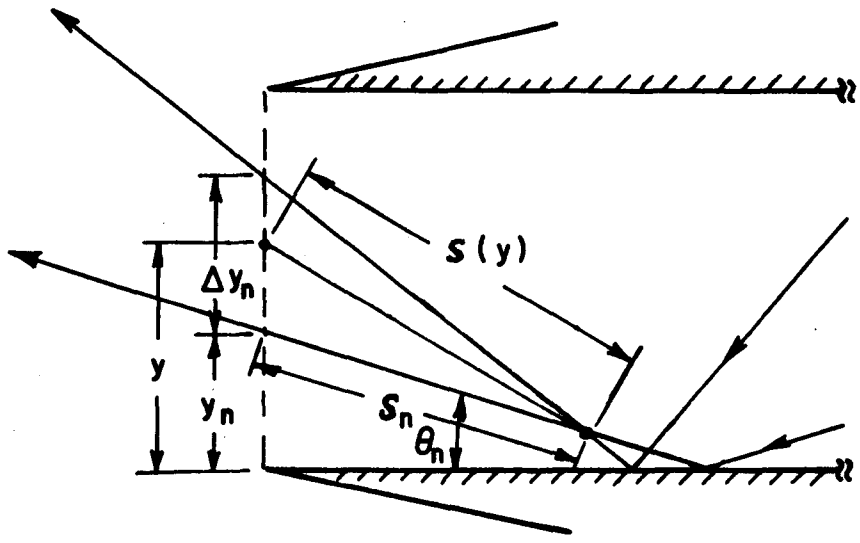

Figure 6.3: Geometry of a ray tube subaperture.

reflections from curved inlet walls, it is no longer columnated and has some spreading (either divergent or convergent). The field in the ray tube will appear to be due to a radiating line source located at some caustic, as shown, with a phase factor representing the propagation path delay of the ray tube up to that point. The magnitude of the field in each subaperture ($y_n < y < y_{n+1}$) is obtained by conserving power in the ray tube which terminates in that subaperture. It is assumed that each ray tube is small enough so that the magnitude of the field in the sub-aperture is approximately constant within that subaperture. To conserve power in each ray tube,

$$(U^{inc})^2 \Delta' = |U_n^{ap}(y)|^2 \Delta_n \tag{6.2}$$

where Δ' is the width of the ray tube when it enters the inlet, and it is given by

$$\Delta' = \frac{d}{N} \cos\theta; \tag{6.3}$$

whereas, Δ_n is the width when it exits, transverse to the direction of propagation. $U_n^{ap}(y)$ is the scalar part of $\vec{U}_n^{ap}(y)$. The (scalar) field in the aperture is then given

via GO by

$$U_n^{ap}(y) = \left|\sqrt{\frac{\Delta'}{\Delta_n}}\right| \Gamma_n j^{c_n} e^{-jk[s(y)+R_n]} \tag{6.4}$$

where R_n is the path length of the n^{th} ray tube inside the inlet up to the last caustic, Γ_n is the product of all the reflection coefficients which describe the reflections encountered each time the ray tube reflected from an inner wall of the inlet, and c_n is the total number of caustics the n^{th} ray tube passed through. The rays are traced according to Snell's law, which requires that ray paths before and after reflections are straight lines, and at reflection points the angle of reflection equals the angle of incidence. Furthermore, the reflected ray, the surface normal and the incident ray at the point of reflection all lie in the same plane which for the two-dimensional case is always in the plane of the paper. The reflection coefficient for a ray reflecting off a semi-infinite dielectric termination inside the inlet cavity is given for the TE case by

$$\Gamma_t = \frac{cos\phi - \frac{1}{\mu_r}\sqrt{\mu_r\epsilon_r - \sin^2\phi}}{cos\phi + \frac{1}{\mu_r}\sqrt{\mu_r\epsilon_r - \sin^2\phi}} \tag{6.5}$$

and for the TM case by

$$\Gamma_t = -\frac{cos\phi - \frac{1}{\epsilon_r}\sqrt{\mu_r\epsilon_r - \sin^2\phi}}{cos\phi + \frac{1}{\epsilon_r}\sqrt{\mu_r\epsilon_r - \sin^2\phi}} \tag{6.6}$$

where μ_r and ϵ_r are the relative permeability and permittivity of the impedance, respectively, and ϕ is the angle the n^{th} ray tube makes with the surface normal when it strikes the dielectric termination. The reflection coefficient for a dielectric coating on a ground plane is given by [8]

$$\Gamma_a = \frac{\sin\theta - \frac{1}{j\mu_r}\sqrt{\epsilon_r\mu_r - \cos^2\theta}\cot(kt\sqrt{\epsilon_r\mu_r - \cos^2\theta})}{\sin\theta + \frac{1}{j\mu_r}\sqrt{\epsilon_r\mu_r - \cos^2\theta}\cot(kt\sqrt{\epsilon_r\mu_r - \cos^2\theta})} \tag{6.7}$$

for the TE case and by

$$\Gamma_a = \frac{\sin\theta - \frac{j}{\epsilon_r}\sqrt{\epsilon_r\mu_r - \cos^2\theta}\tan(kt\sqrt{\epsilon_r\mu_r - \cos^2\theta})}{\sin\theta + \frac{j}{\epsilon_r}\sqrt{\epsilon_r\mu_r - \cos^2\theta}\tan(kt\sqrt{\epsilon_r\mu_r - \cos^2\theta})} \tag{6.8}$$

for the TM case where ϵ_r and μ_r are the relative permittivity and permeability, respectively, of the coating, t is the thickness of the coating, k is the free space wave number and θ is the angle the propagation vector of the incident plane wave makes with the surface.

To find c_n, the total number of caustics a ray passes through, it is necessary to keep a track of the relative caustic position as the ray is traced. Each reflection from a curved surface changes this position. Figure 6.4 shows a typical reflection from such an interior boundary or surface of the inlet and how a new caustic is formed. The new caustic distance ρ_c after that reflection in Figure 6.4 is given in terms of the previous caustic distance ρ_c' before the reflection in that figure by [5]

$$\rho_c = \frac{\rho_c' R\sin\phi}{R\sin\phi + 2\rho_c'}. \tag{6.9}$$

Notice that ρ_c as well as ρ_c' can be negative. R which is the radius of curvature of the surface at the point of reflection is positive for a convex boundary but is negative for a concave boundary. If $\rho_c < 0$ and $|\rho_c|$ is less than the distance from the reflection point to the reciever point ρ, then the caustic lies inside of the inlet and c_n is incremented. This must be checked after each reflection while tracing the ray through the inlet. The caustic of the incident ray tube entering the inlet is at infinity in the direction of the source.

The integral in equation (6.1) can now be written as:

$$\int_{y_n}^{y_{n+1}} U_n^{ap}(y)e^{-jky\sin\theta}dy = \left|\sqrt{\frac{\Delta'}{\Delta_n}}\right|\Gamma_n j^{c_n}e^{-jk(R_n - s_n)} \cdot \int_{y_n}^{y_{n+1}} e^{-jk[s(y)+y\sin\theta]}dy \tag{6.10}$$

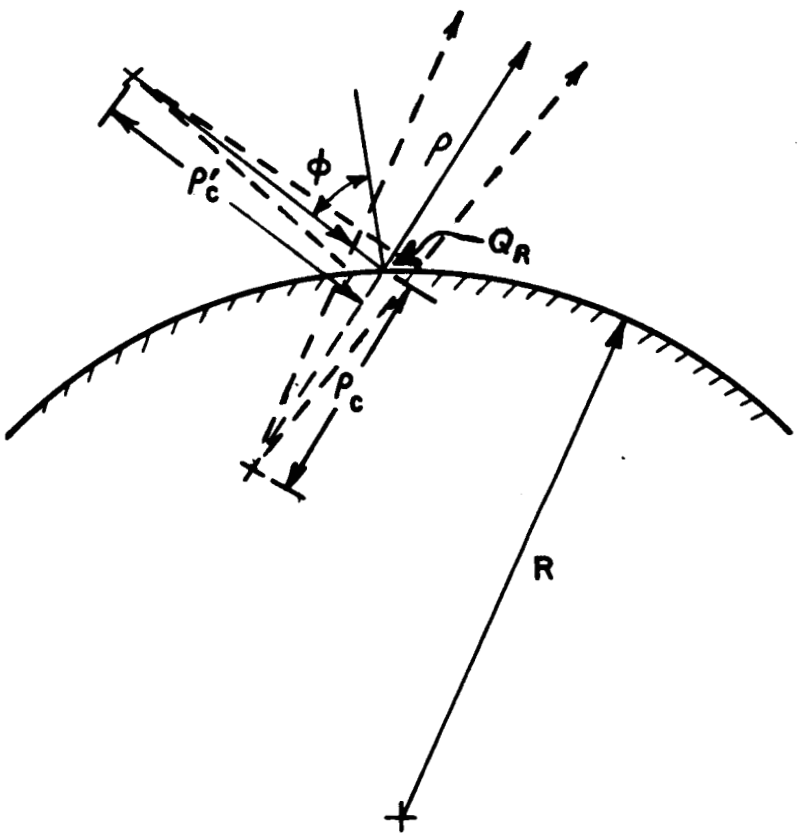

Figure 6.4: Reflection from a curved surface. ρ'_c is the caustic distance before reflection at Q_R and ρ_c is the new caustic distance after reflection.

where

$$s(y) = \sqrt{s_n^2 + (y - y_n)^2 + 2(y - y_n)s_n \sin\theta_n}. \tag{6.11}$$

For $\Delta y_n \ll s_n$, $s(y)$ can be approximated as a linear function of y

$$s(y) \approx s_n + (y - y_n)\sin\theta_n \tag{6.12}$$

so that the integral of equation (6.1) can be evaluated in closed form to give the final result as:

$$\int_{y_n}^{y_{n+1}} U_n^{ap}(y) e^{-jky\sin\theta} dy = \left|\sqrt{\frac{\Delta'}{\Delta_n}}\right| \Gamma_n j^{c_n} e^{-jk\left[R_n + \frac{1}{2}(y_n + y_{n+1})\sin\theta + \frac{1}{2}\Delta y_n \sin\theta_n\right]} \cdot \Delta y_n \mathrm{sinc}\left[\frac{1}{2}k\Delta y_n(\sin\theta_n + \sin\theta)\right]. \tag{6.13}$$

The total scattered field is given as the sum of the cavity scattering and the field scattered by the edges at the open end of the inlet:

$$\vec{U}^{scat} = \vec{U}^{cav} + \vec{U}^{edge} \tag{6.14}$$

$$\vec{U}^{edge} = \hat{z} R_{01} U^{inc} \frac{e^{-jk\rho}}{\sqrt{\rho}} \tag{6.15}$$

where R_{01} is given by equation (3.88).

6.2 Numerical Examples Based on the GO/AI Method

As it turns out, the GO/AI method gives increasingly less accurate results as the inlets become longer. This is due to the fact that the method does not include the diffracted fields inside the inlet which generally become dominant as the wave propagation distance inside the inlet increases. The reflected beam that is initially collimated usually becomes diffused at larger distances inside the inlet because of the presence of fields diffracted by edges at the open end which enter into the inlet. Also, the method becomes less accurate at lower frequencies because fewer inlet waveguide modes propagate. For these reasons, the sample inlets used in this

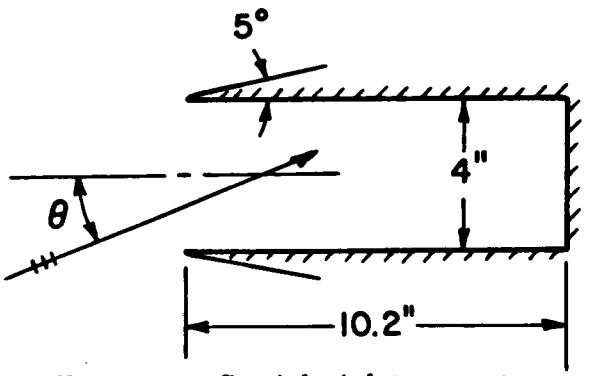

Figure 6.5: Straight inlet geometry.

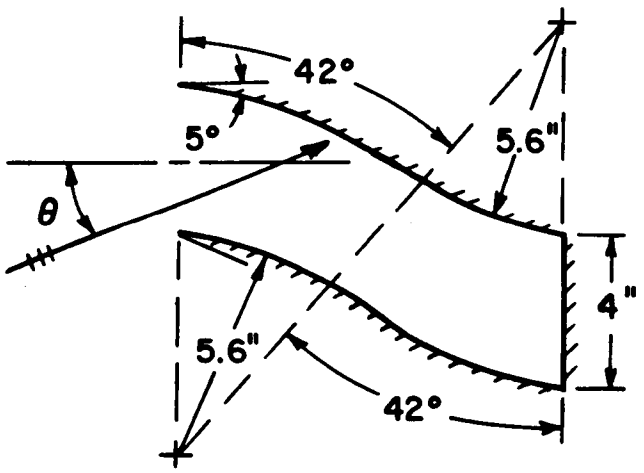

Figure 6.6: Offset inlet geometry.

section are shallower than those of the previous chapters. Their geometries are shown in Figures 6.5 and 6.6; it is seen from those figures that again one inlet is straight and the other is offset or S-shaped in which the offset inlet consists of two curved sections. The parameters of the absorber coating are the same as in (4.52)-(4.57) with an additional case where $t = .005$". This lossier coating causes about 5 dB of loss per reflection at normal incidence compared with 1 dB for the thinner coating ($t = .001$").

Figures 6.7-6.22 show the backscatter pattern vs. aspect angle for the two inlets of Figures 6.5 and 6.6 at 10 and 35 GHz for the two polarizations. The top figure on each page is the hybrid solution for the lossless and 1 dB loss/reflection cases,

included for comparison. The aspect angle is limited to within 20 degrees of the axis and the data points are 2 degrees apart in these calculations because the ray-tracing method takes a large amount of computing time. In general, the more complex the inlet shape, the more ray tubes are needed to converge to the GO based result. Therefore, the offset inlet of Figure 6.6 requires more ray tubes (and hence more computing time) than the simple parallel plate inlet of Figure 6.5.

The plots illustrate that the GO/AI method can roughly predict the average of the backscatter pattern, but details are lacking. This is expected due to the approximate nature of a technique which does not include effects of diffraction. The only advantage of this method, other than its analytic simplicity, is that it is not limited to inlets made up of uniform waveguide sections which a modal method would require. It is noticed from the backscatter patterns that for this shallower inlet, the termination is not as well hidden for near-axial incidence and that the presence of the absorber coating has a substantial effect in consistently reducing the overall backscatter pattern.

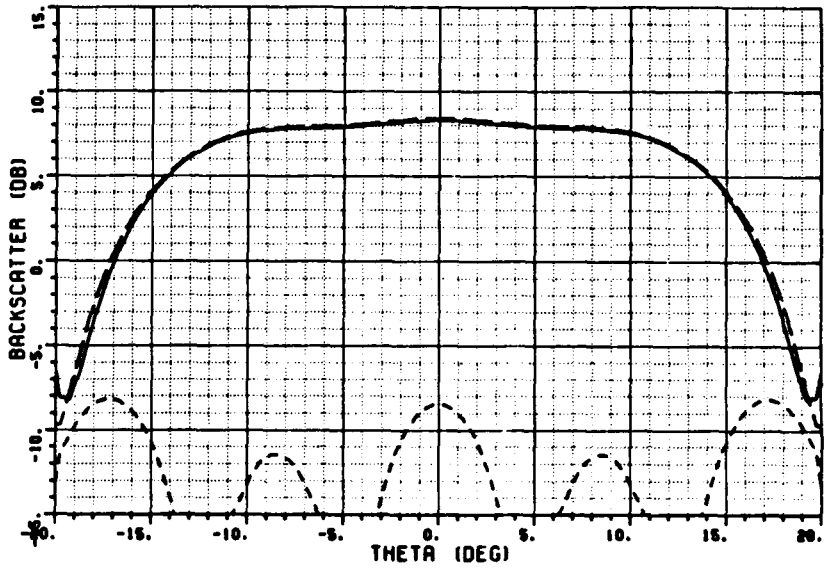

Figure 6.7: TE Backscatter pattern for the straight inlet at 10 GHz, modal solution. —- Lossless, – – 1 dB loss/refl., - - - leading edges only.

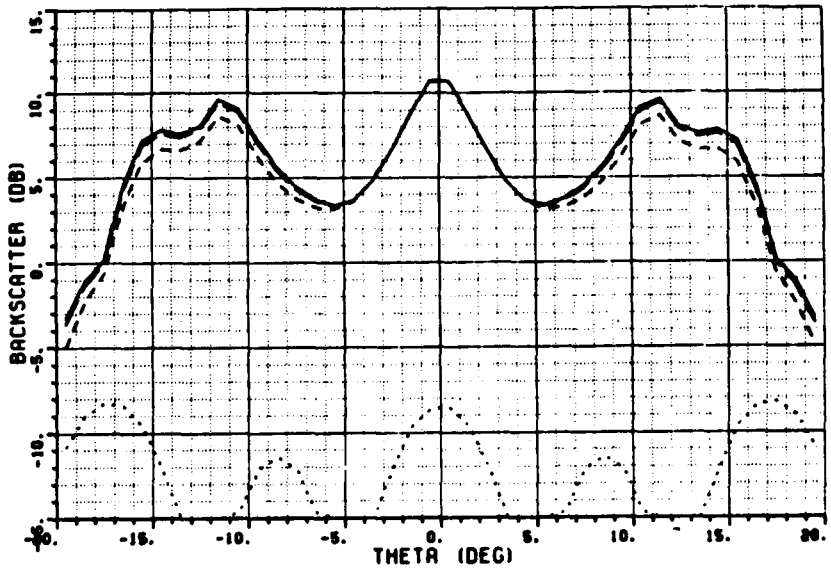

Figure 6.8: TE Backscatter pattern for the straight inlet at 10 GHz, GO/AI solution. —- Lossless, – – 1 dB loss/refl., - - - 5 dB loss/refl., · · · leading edges only.

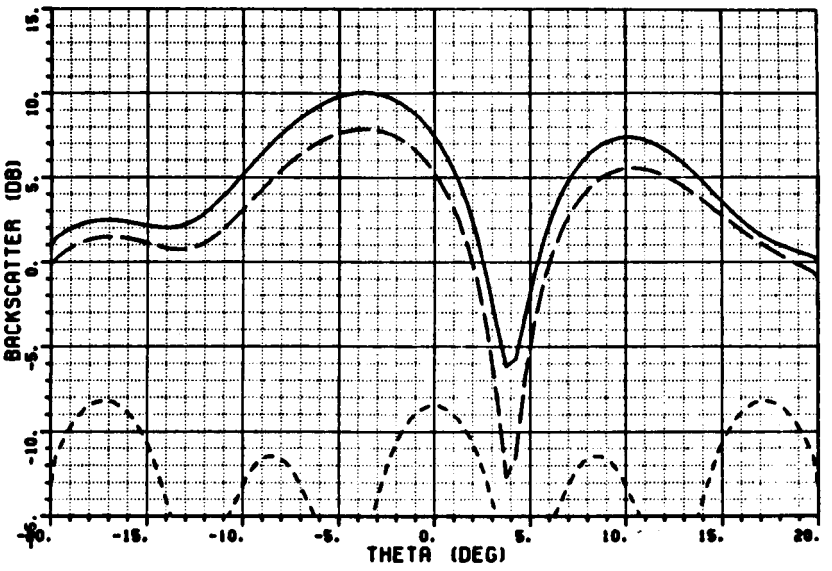

Figure 6.9: TE Backscatter pattern for the S-bend inlet at 10 GHz, modal solution. —- Lossless, – – 1 dB loss/refl., - - - leading edges only.

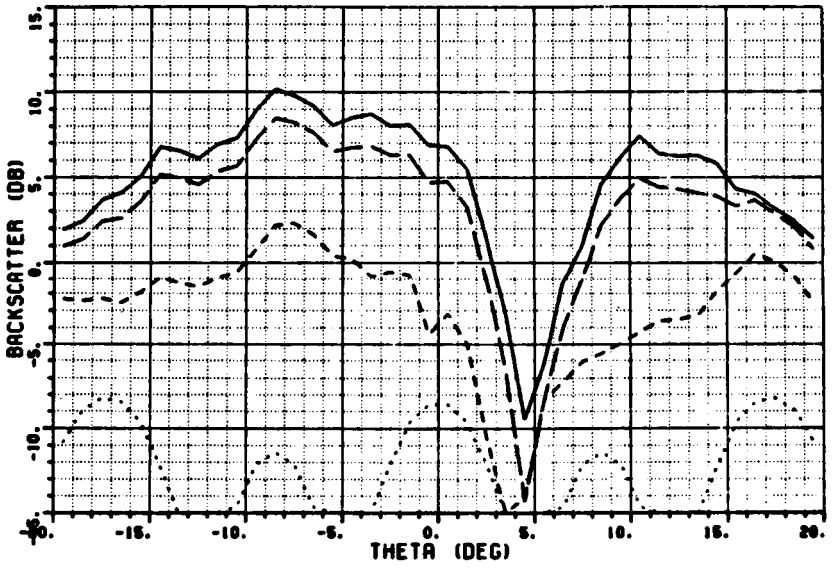

Figure 6.10: TE Backscatter pattern for the S-bend inlet at 10 GHz, GO/AI solution. —- Lossless, – – 1 dB loss/refl., - - - 5 dB loss/refl., · · · leading edges only.

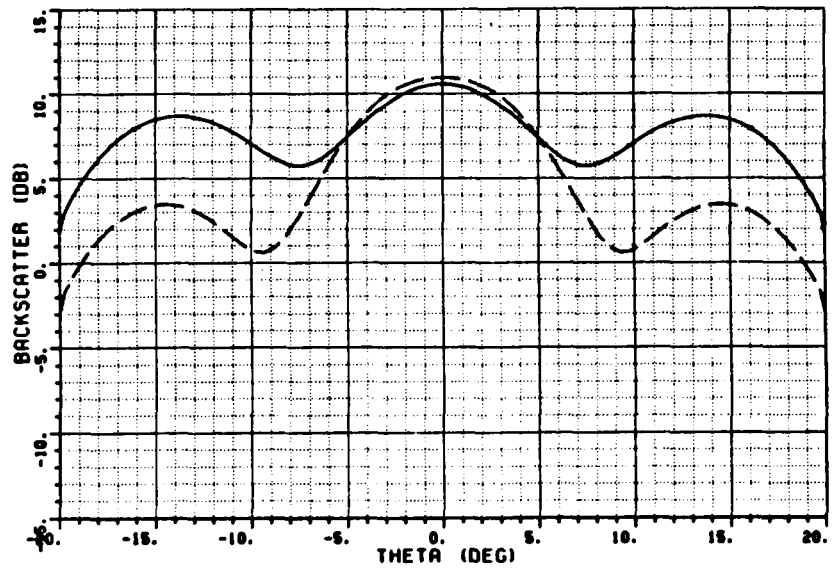

Figure 6.11: TM Backscatter pattern for the straight inlet at 10 GHz, modal solution. —- Lossless, – – 1 dB loss/refl., - - - leading edges only.

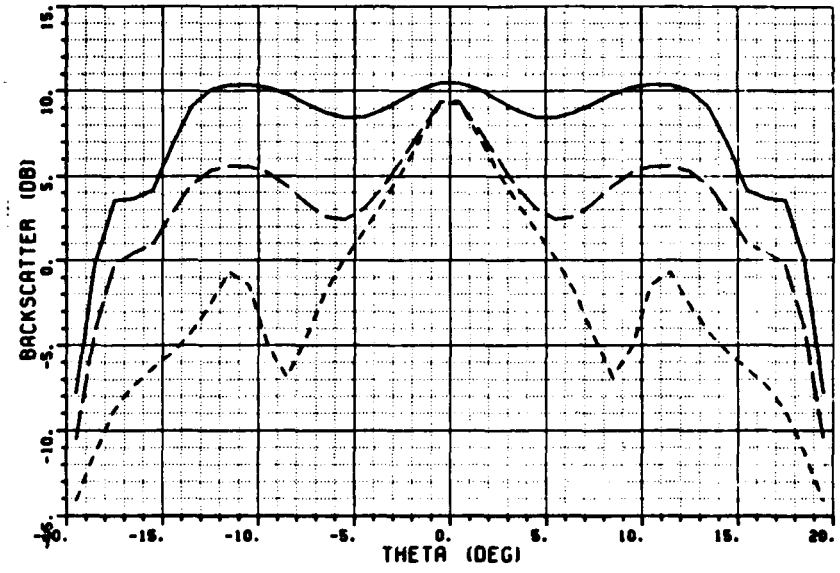

Figure 6.12: TM Backscatter pattern for the straight inlet at 10 GHz, GO/AI solution. —- Lossless, – – 1 dB loss/refl., - - - 5 dB loss/refl., ··· leading edges only.

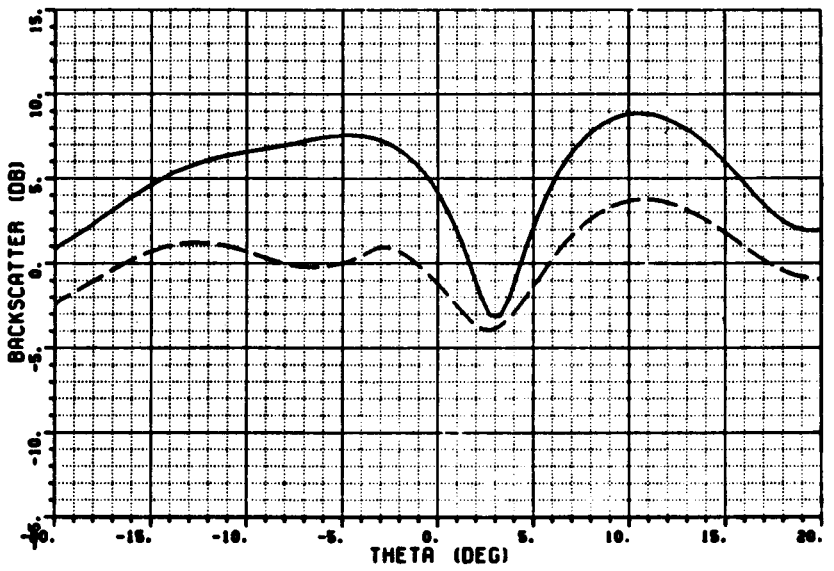

Figure 6.13: TM Backscatter pattern for the S-bend inlet at 10 GHz, modal solution. —- Lossless, – – 1 dB loss/refl., - - - leading edges only.

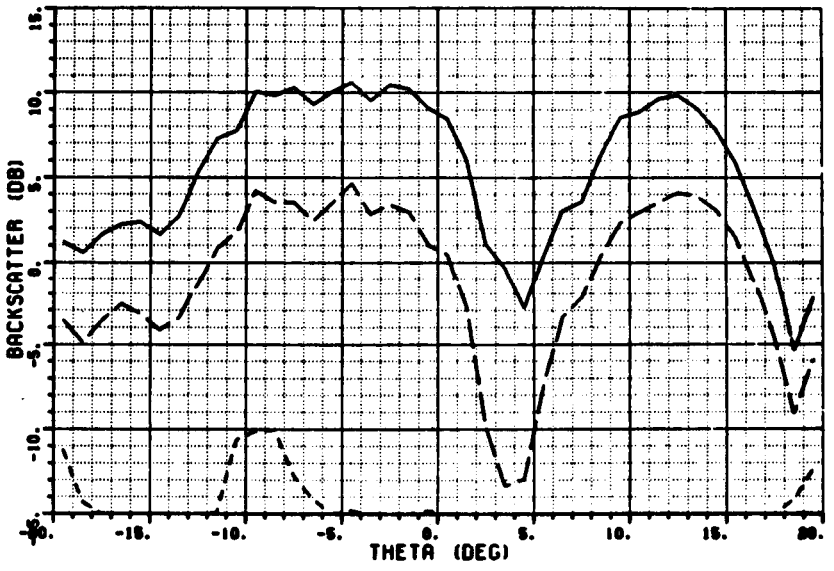

Figure 6.14: TM Backscatter pattern for the S-bend inlet at 10 GHz, GO/AI solution. —- Lossless, – – 1 dB loss/refl., - - - 5 dB loss/refl., · · · leading edges only.

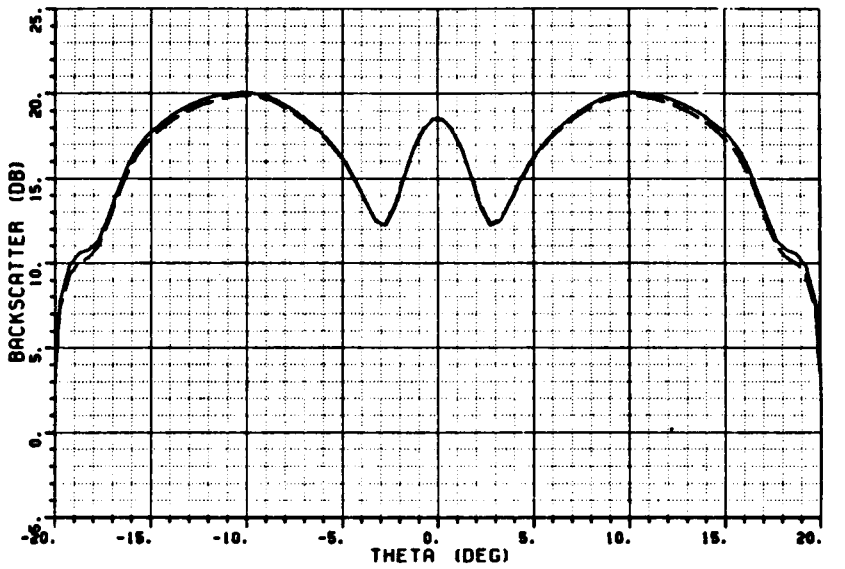

Figure 6.15: TE Backscatter pattern for the straight inlet at 35 GHz, modal solution. —- Lossless, – – 1 dB loss/refl., - - - leading edges only.

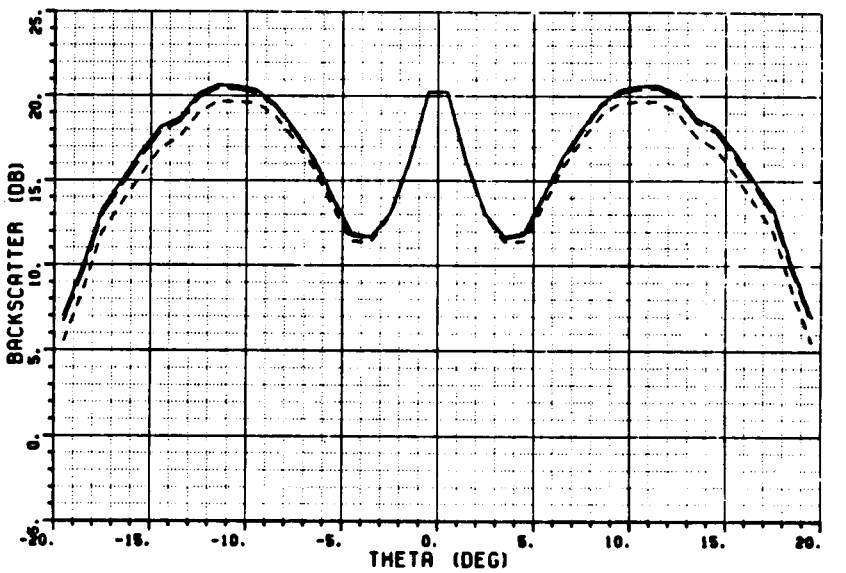

Figure 6.16: TE Backscatter pattern for the straight inlet at 35 GHz, GO/AI solution. —- Lossless, – – 1 dB loss/refl., - - - 5 dB loss/refl., ··· leading edges only.

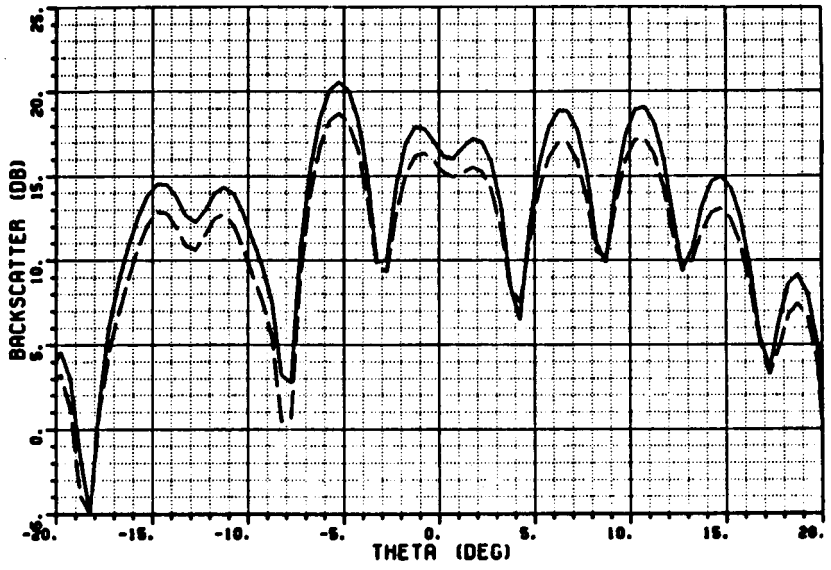

Figure 6.17: TE Backscatter pattern for the S-bend inlet at 35 GHz, modal solution. —- Lossless, – – 1 dB loss/refl., - - - leading edges only.

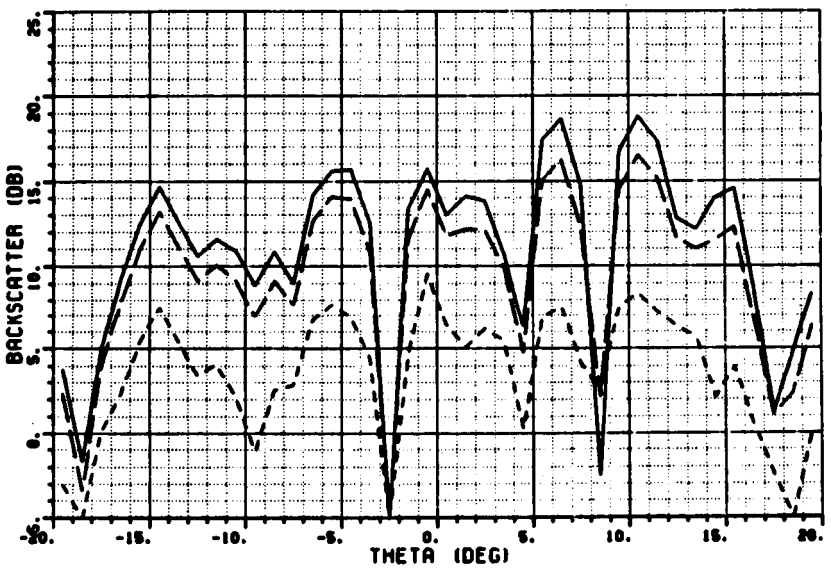

Figure 6.18: TE Backscatter pattern for the S-bend inlet at 35 GHz, GO/AI solution. —- Lossless, – – 1 dB loss/refl., - - - 5 dB loss/refl., · · · leading edges only.

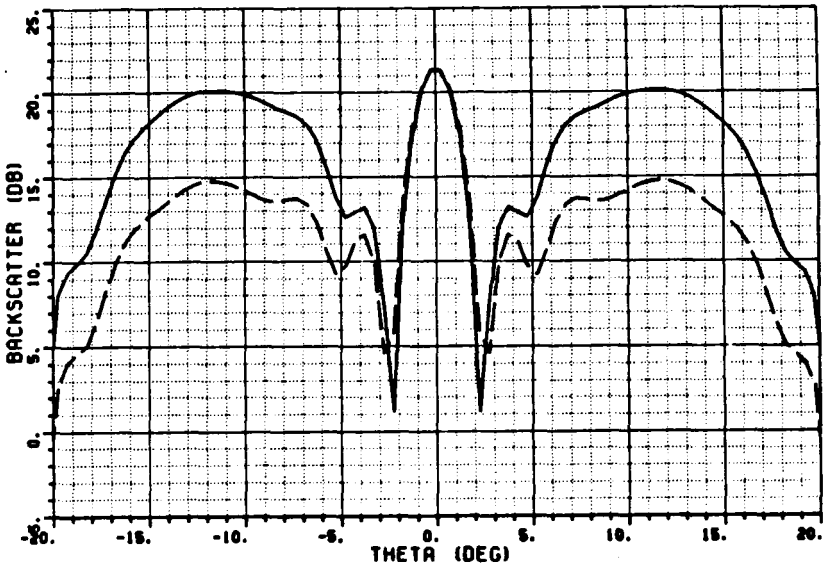

Figure 6.19: TM Backscatter pattern for the straight inlet at 35 GHz, modal solution. —- Lossless, – – 1 dB loss/refl., - - - leading edges only.

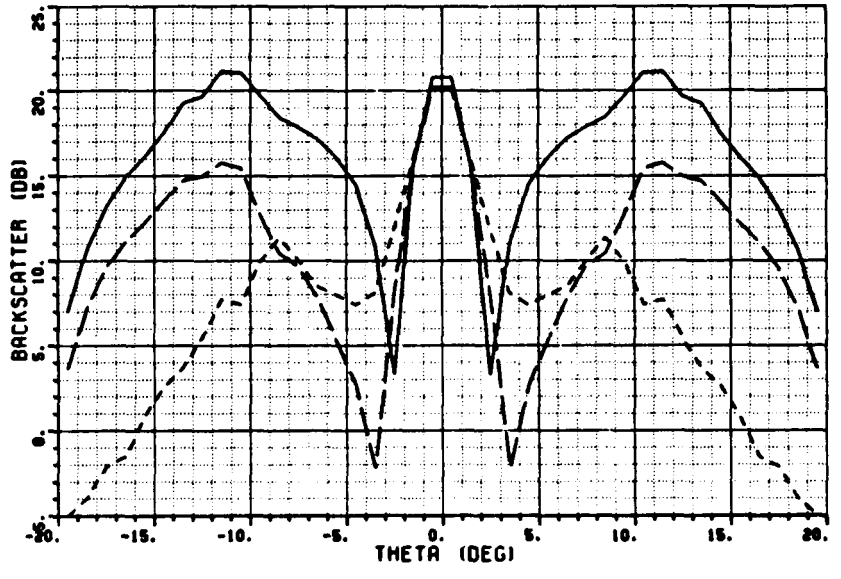

Figure 6.20: TM Backscatter pattern for the straight inlet at 35 GHz, GO/AI solution. —- Lossless, – – 1 dB loss/refl., - - - 5 dB loss/refl., ··· leading edges only.

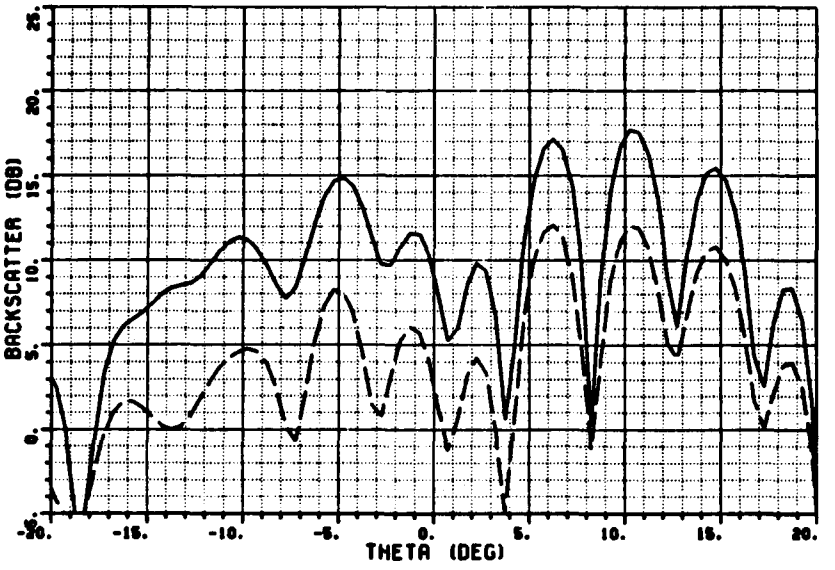

Figure 6.21: TM Backscatter pattern for the S-bend inlet at 35 GHz, modal solution. —- Lossless, – – 1 dB loss/refl., - - - leading edges only.

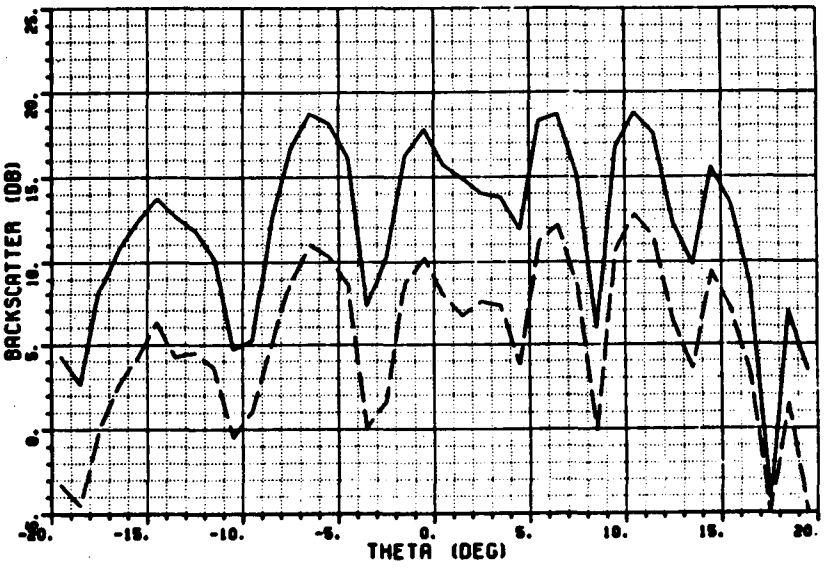

Figure 6.22: TM Backscatter pattern for the S-bend inlet at 35 GHz, GO/AI solution. —- Lossless, – – 1 dB loss/refl., - - - 5 dB loss/refl., · · · leading edges only.

7. Conclusion

It has been shown that the effect of employing an S-shaped inlet for making the termination not directly visible alters the backscattered pattern so that it does not peak near the forward axis of the inlet. Also, the overall pattern envelope flattened out and was reduced by a few dB, especially for longer inlets. Adding the absorber coating to the straight inlet did not effectively remove the peak in the backscatter pattern near the inlet axis. Combining the absorber coating with the S-bend offset effectively and consistently resulted in flattening out and reducing the overall backscatter pattern, even near axial incidence.

The scattering from the interior inlet cavity termination is the dominant contributor to the total scattering by the inlet cavity except when the termination is highly absorbing in which case the scattering from the edges at the opening in front of the inlet dominates. It was also shown that the reflections from the junctions of waveguide sections from which the S-shaped inlet is "built up" are very small and can usually be neglected. The interior reflection from the open end was seen to be on the order of the scattering by the edges so this contribution to the backscatter should be included.

The field expansion/matching technique of chapter 5 gives analytically accurate results and can handle any absorber coating which can be characterized by an equivalent surface impedance. However, the method is largely numerical and therefore gives little insight into the scattering mechanisms of the interior region of the inlet as well as requiring a large amount of computing time. Its main purpose here was as a means of checking the more approximate and efficient hybrid technique.

The GO/AI method of finding the backscattered field was not as accurate as the modal method, especially for smaller guide widths and longer inlets. However, its usefulness becomes apparent when the guide width becomes large so that there are many propagating modes. At higher frequencies, the modal method becomes more

cumbersome but it remains quite accurate. The GO/AI method tends to become more accurate at higher frequencies. It is reasonable to suggest that the modal method be used for guides of width less than about 15 wavelengths (30 propagating modes) and the GO/AI method for larger guide widths.

A. Orthonormal Modes of the Parallel Plate Waveguide

This appendix derives the expressions for the orthonormal modal fields of the uniform parallel plate waveguide. The modal ray form of these modes is also derived.

"Orthonormal" means that each mode carries power independently of all the other modes and they are normalized to carry unit power. Mathematically, this is written

$$\int_S \hat{e}_m(y) \times \hat{h}_n(y) \cdot d\vec{S} \;=\; \delta_{mn} \tag{A.1}$$

where δ_{mn} is the Kroeneker delta function given by

$$\delta \;=\; \begin{cases} 1 & \text{if } m = n \\ 0 & \text{if } m \neq n \end{cases} \tag{A.2}$$

and $\vec{S}$ represents any complete cross-section of the guide.

Figure A.1 shows a parallel plate waveguide of infinite extent. Starting with the TE case, the electric field is in the $\hat{z}$-direction and is a function of x and y

$$\vec{E}(x,y) \;=\; \hat{z}E_z(x,y). \tag{A.3}$$

The E-field is a solution to the wave equation

$$(\nabla^2 + k^2)\vec{E}(x,y) \;=\; 0 \tag{A.4}$$

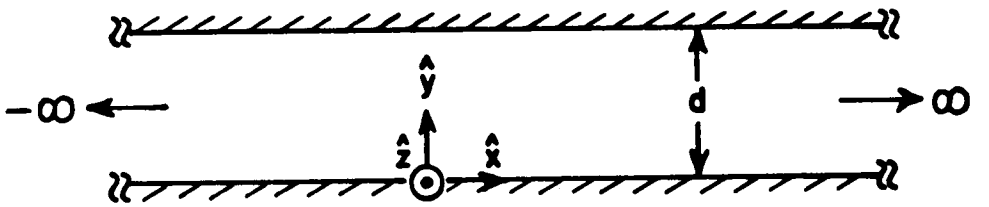

Figure A.1: Parallel plate waveguide geometry.

which in scalar form is

$$\left(\frac{\partial^2}{\partial x^2}+\frac{\partial^2}{\partial y^2}+k^2\right)E_z(x,y) \;=\; 0 \tag{A.5}$$

where k is the free space wave number, $2\pi/\lambda$. The boundary condition is that E_z equals zero on the walls of the guide. Using separation of variables and enforcing the boundary conditions the solution is found to be an infinite summation of modes

$$\vec{E}(x,y) \;=\; \sum_{n=1}^{\infty}\left[A_n^+\hat{e}_n(y)e^{-j\beta_n x}+A_n^-\hat{e}_n(y)e^{j\beta_n x}\right] \tag{A.6}$$

where

$$\hat{e}_n(y) \;=\; \hat{z}P_n\sin(\frac{n\pi}{d}y) \tag{A.7}$$

$$\beta_n \;=\; \sqrt{k^2-(\frac{n\pi}{d})^2}. \tag{A.8}$$

P_n is a constant which normalizes the power of the n^{th} mode and $A_n^{\pm}$ are arbitrary constants. The infinite sum is usually truncated to include only propagating modes. For n greater than some number N, the modes are evanescent in nature and die out exponentially along the axis of the guide. This cutoff number is one less than the the value of n which makes β_n pure imaginary, or

$$N \;=\; \mathrm{int}(\frac{kd}{\pi}) \tag{A.9}$$

(the integer portion of kd/π).

The H-field of the guide is derived directly from the E-field using one of Maxwell's equations

$$\nabla\times\vec{E}(x,y) \;=\; -j\omega\mu\vec{H}(x,y) \tag{A.10}$$

$$\omega\mu \;=\; \frac{k}{Y_0} \tag{A.11}$$

which gives

$$\vec{H}(x,y) \;=\; \frac{Y_0}{jk}\left(\hat{y}\frac{\partial}{\partial x}-\hat{x}\frac{\partial}{\partial y}\right)E_z(x,y)$$

$$= \sum_{n=1}^{\infty} \left[A_n^+ \hat{h}_n^+(y) e^{-j\beta_n x} + A_n^- \hat{h}_n^-(y) e^{j\beta_n x} \right] \tag{A.12}$$

$$\hat{h}_n^{\pm}(y) = P_n Y_0 \left[\mp \hat{y} \frac{\beta_n}{k} \sin(\frac{n\pi}{d} y) - \hat{x} \frac{n\pi}{jkd} \cos(\frac{n\pi}{d} y) \right]. \tag{A.13}$$

P_n is found by normalizing to unity the power carried by the n^{th} mode. This is done by integrating the Pointing vector over a cross-section of the guide and setting this equal to unity,

$$\int_0^d \hat{e}_n(y) \times \hat{h}_n^{\pm}(y) \cdot (\pm \hat{x}) dy = 1. \tag{A.14}$$

Substituting and integrating gives

$$P_n = \sqrt{\frac{2kZ_0}{d\beta_n}}. \tag{A.15}$$

The ray-optical form of these modes is found by writing the sine function of equation (A.6) in its Euler (exponential) form and combining the exponentials,

$$\hat{e}_n(y) e^{\mp j\beta_n x} = \hat{z} \frac{P_n}{2j} \left[e^{j(\frac{n\pi}{d} y \mp \beta_n x)} - e^{j(-\frac{n\pi}{d} y \mp \beta_n x)} \right]. \tag{A.16}$$

By making the substitution

$$\sin\theta_n = \frac{n\pi}{kd} \tag{A.17}$$

equation (A.15) can be written

$$\hat{e}_n(y) e^{\mp j\beta_n x} = \hat{z} \frac{P_n}{2j} \left[e^{jk(y \sin\theta_n \mp x \cos\theta_n)} - e^{jk(-y \sin\theta_n \mp x \cos\theta_n)} \right] \tag{A.18}$$

because

$$\begin{aligned} \beta_n &= \sqrt{k^2 - (\frac{n\pi}{d})^2} \\ &= k\sqrt{1 - (\frac{n\pi}{kd})^2} \\ &= k\sqrt{1 - \sin^2\theta_n} \\ &= k\cos\theta_n. \end{aligned} \tag{A.19}$$

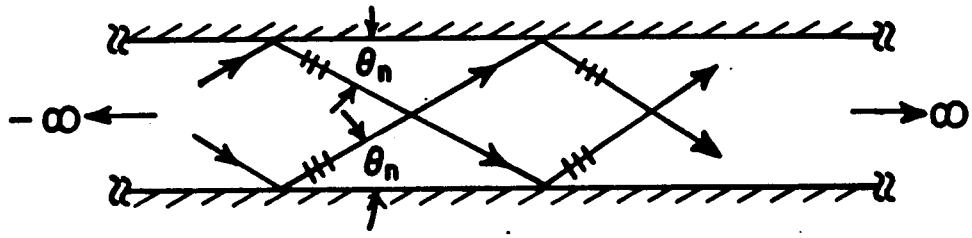

Figure A.2: Modal rays of the parallel plate waveguide.

This form represents two crossing plane waves which make an angle of θ_n with the guide walls as shown in Figure A-2.

The TM case is handled similarly, with the boundary condition being $\partial H_z/\partial y$ equal zero on the walls,

$$\vec{H}(x,y) = \hat{z}H_z(x,y) \tag{A.20}$$

$$(\nabla^2 + k^2)\vec{H}(x,y) = \left(\frac{\partial^2}{\partial x^2} + \frac{\partial^2}{\partial y^2} + k^2\right) H_z(x,y) = 0 \tag{A.21}$$

$$\vec{H}(x,y) = \sum_{n=0}^{\infty} \left[A_n^+ \hat{h}_n(y) e^{-j\beta_n x} + A_n^- \hat{h}_n(y) e^{j\beta_n x}\right] \tag{A.22}$$

$$\hat{h}_n(y) = \hat{z} P_n \cos(\frac{n\pi}{d} y) \tag{A.23}$$

$$\beta_n = \sqrt{k^2 - (\frac{n\pi}{d})^2} \tag{A.24}$$

$$\nabla \times \vec{H}(x,y) = j\omega\varepsilon \vec{E}(x,y) \tag{A.25}$$

$$\omega\varepsilon = \frac{k}{Z_0} \tag{A.26}$$

$$\vec{E} = -\frac{Z_0}{jk}\left(\hat{y}\frac{\partial}{\partial x} - \hat{x}\frac{\partial}{\partial y}\right) H_z(x,y) = \sum_{n=0}^{\infty} \left[A_n^+ \hat{e}_n^+(y) e^{-j\beta_n x} + A_n^- \hat{e}_n^-(y) e^{j\beta_n x}\right] \tag{A.27}$$

$$\hat{e}_n^{\pm}(y) = P_n Z_0 \left[\pm\hat{y}\frac{\beta_n}{k}\cos(\frac{n\pi}{d} y) - \hat{x}\frac{n\pi}{jkd}\sin(\frac{n\pi}{d} y)\right] \tag{A.28}$$

$$P_n = \sqrt{\frac{2kY_0}{d\beta_n\varepsilon_n}} \tag{A.29}$$

$$\varepsilon_n = \begin{cases} 2 & \text{if } n = 0 \\ 1 & \text{otherwise} \end{cases} \tag{A.30}$$

and the ray-optical form of equation (A.22) is given by

$$\hat{h}_n(y)e^{\mp j\beta_n x} = \hat{z}\frac{P_n}{2}\left[e^{jk(y\sin\theta_n \mp x\cos\theta_n)} + e^{jk(-y\sin\theta_n \mp x\cos\theta_n)}\right]. \tag{A.31}$$

Notice that for the TM case, the $n = 0$ term is included in the summation. This corresponds to a TEM mode. Ray-optically this mode is a plane wave traveling down the guide with θ_n equal zero.

B. Orthonormal Modes of the Annular Waveguide

This appendix derives the expressions for the orthonormal modal fields of the uniform annular waveguide. "Orthonormal" means that each mode carries power independently of all the other modes and they are normalized to carry unit power, as described more fully in Appendix A. The asymptotic ray-optical form of these modes is also derived.

Figure B.1 shows an annular waveguide of infinite extent. This makes no sense physically because the guide would join ends to form a ring. However, it is allowable mathmatically to assume that ϕ goes to infinity in both directions. It is necessary to make this assumption to get the correct waveguide modes to describe the fields in small sections of an annular guide, such as the ones used to make up the inlet. Starting with the TE case, the electric field is in the $\hat{z}$-direction and is a function of ρ and ϕ

$$\vec{E}(\rho,\phi) \;=\; \hat{z}E_z(\rho,\phi). \tag{B.1}$$

The E-Field is a solution to the wave equation

$$(\nabla^2 + k^2)\vec{E}(\rho,\phi) \;=\; 0 \tag{B.2}$$

which in scalar form is (using the cylindrical form of the Laplacian)

$$\left[\frac{1}{\rho}\frac{\partial}{\partial\rho}(\rho\frac{\partial}{\partial\rho}) + \frac{1}{\rho^2}\frac{\partial^2}{\partial\phi^2} + k^2\right] E_z(\rho,\phi) \;=\; 0 \tag{B.3}$$

where k is the free space wave number, $2\pi/\lambda$. The boundary condition is that E_z equals zero on the walls of the guide. Separating variables and substituting into equation (B.3), multiplying by ρ^2 and dividing out $E_z(\rho,\phi)$ gives

$$\frac{\rho}{R(\rho)}\frac{d}{d\rho}\left[\rho\frac{dR(\rho)}{d\rho}\right] + \frac{1}{\Phi(\phi)}\frac{d^2\Phi(\phi)}{d\phi^2} + (k\rho)^2 \;=\; 0 \tag{B.4}$$

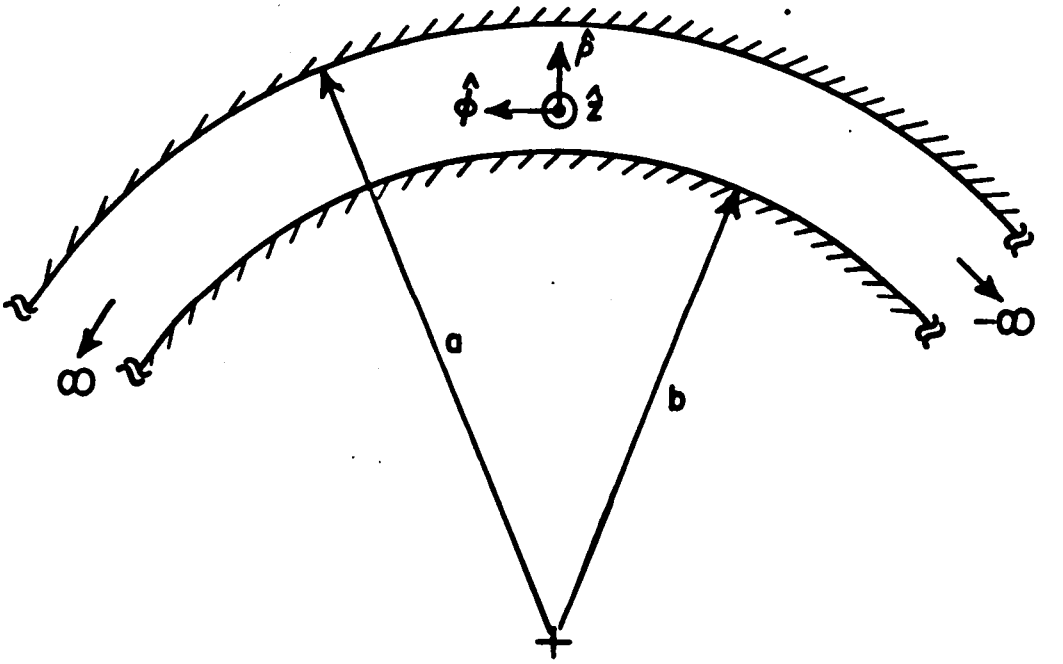

Figure B.1: Annular waveguide geometry.

where the separation equation is

$$E_z(\rho,\phi) = R(\rho)\Phi(\phi). \tag{B.5}$$

Introducing the separation constant ν gives the two independent differential equations

$$\frac{1}{\Phi(\phi)}\frac{d^2\Phi(\phi)}{d\phi^2} = -\nu^2 \tag{B.6}$$

$$\rho\frac{d}{d\rho}\left[\rho\frac{dR(\rho)}{d\rho}\right] + [(k\rho)^2 - \nu^2]R(\rho) = 0. \tag{B.7}$$

The solutions to equation (B.6) are

$$\Phi(\phi) = e^{j\nu\phi} \text{ and } e^{-j\nu\phi}. \tag{B.8}$$

(B.7) is Bessel's equation and has solutions

$$R(\rho) = H_\nu^{(1)}(k\rho) \text{ and } H_\nu^{(2)}(k\rho) \tag{B.9}$$

where $H_\nu^{(1)}(k\rho)$ and $H_\nu^{(2)}(k\rho)$ are the Hankel functions of the first and second kinds, respectively, of order ν and argument $k\rho$. Using linear combinations of these solutions and enforcing the boundary conditions gives the complete solution for the E-field

$$\vec{E}(\rho,\phi) = \sum_{n=1}^{\infty}\left[B_n^+\hat{e}_n(\rho)e^{-j\nu_n\phi} + B_n^-\hat{e}_n(\rho)e^{j\nu_n\phi}\right] \tag{B.10}$$

where

$$\hat{e}_n(\rho) = \hat{z}A_nR_n(k\rho) \tag{B.11}$$

$$R_n(k\rho) = \frac{1}{2j}\left[H_{\nu_n}^{(2)}(kb)H_{\nu n}^{(1)}(k\rho) - H_{\nu_n}^{(1)}(kb)H_{\nu_n}^{(2)}(k\rho)\right] \tag{B.12}$$

in which $R_n(kb) = 0$ has been employed and where A_n is the normalization constant of the n^{th} mode and $B_n^{\pm}$ are arbitrary constants. If ϕ had a periodic boundary condition corresponding to a 360 degree annular ring, the eigenvalues ν_n would be

completely determined. However, for the annular guide of infinite extent, the eigenvalues must be found using the remaining radially ρ dependent boundary condition. Thus, they are found from the transcendental equation

$$R_n(ka) = 0 \tag{B.13}$$

which usually must be solved numerically.

As in a parallel plate guide, the summation generally only includes values of n for which ν_n is real. This is because for some values of n, ν_n will be purely imaginary and the mode will die out exponentially along the axis of the guide.

The H-field of the guide is derived directly from the E-field using one of Maxwell's equations

$$\nabla \times \vec{E}(\rho,\phi) = -j\omega\mu\vec{H}(\rho,\phi) \tag{B.14}$$

$$\omega\mu = \frac{k}{Y_0} \tag{B.15}$$

which gives

$$\begin{aligned}\vec{H}(\rho,\phi) &= -\frac{Y_0}{jk}\left(\hat{\rho}\frac{1}{\rho}\frac{\partial}{\partial\phi} - \hat{\phi}\frac{\partial}{\partial\rho}\right)E_z(\rho,\phi) \\ &= \sum_{n=1}^{\infty}\left[B_n^+\hat{h}_n^+(\rho)e^{-j\nu_n\phi} + B_n^-\hat{h}_n^-(\rho)e^{j\nu_n\phi}\right] \qquad \text{(B.16)}\end{aligned}$$

$$\hat{h}_n^{\pm}(\rho) = A_nY_0\left[\pm\hat{\rho}\frac{\nu_n}{k\rho}R_n(k\rho) - \hat{\phi}jR_n'(k\rho)\right]. \tag{B.17}$$

A_n is found by normalizing to unity the power carried by the n^{th} mode. This done by integrating the Poynting vector over a cross-section of the guide and setting this equal to unity,

$$\int_b^a \hat{e}_n(\rho)\times\hat{h}_n^{\pm}(\rho)\cdot(\pm\hat{\phi})d\rho = 1. \tag{B.18}$$

Substituting and changing the variable of integration to $u = k\rho$ gives the normal-

ization coefficient

$$A_n = \left[\frac{\nu_n}{kZ_0}\int_{kb}^{ka} R_n^2(u)\frac{du}{u}\right]^{-\frac{1}{2}}. \tag{B.19}$$

The integral of equation (B.19) can be written in closed form using a property of Hankel functions. However, the resulting equation is quite long and cumbersome and contains derivatives with respect to the order ν_n of the Hankel functions. It was found that it is easier to just do the integration numerically.

The ray-optical form of the waveguide modes in the annular guide is obtained using the large argument approximation to the Hankel functions (also known as the Debye Tangent approximation). For the Hankel function of the second kind, it is given by

$$H_\nu^{(2)}(x) \approx \sqrt{\frac{j2}{\pi x \sin\gamma}}e^{-j(x\sin\gamma-\nu\gamma)} \tag{B.20}$$

where

$$\cos\gamma = \frac{\nu}{x}. \tag{B.21}$$

Using this approximation, the $H_{\nu_n}^{(2)}$ term of a mode with the ϕ variation included can be written as

$$H_{\nu_n}^{(2)}(k\rho)e^{-j\nu_n\phi} \approx \sqrt{\frac{j2}{\pi k\rho\sin\gamma}}e^{-j[k\rho\sin\gamma+\nu_n(\phi-\gamma)]} \tag{B.22}$$

$$\cos\gamma = \frac{\nu_n}{k\rho}. \tag{B.23}$$

Changing variables gives the ray-optical form

$$H_{\nu_n}^{(2)}(k\rho)e^{-j\nu_n\phi} \approx \sqrt{\frac{j2}{\pi ku}}e^{-j(ku+\nu_n\phi_0)} \tag{B.24}$$

$$u = \rho\sin\gamma \tag{B.25}$$

$$\phi = \gamma+\phi_0 \tag{B.26}$$

where ϕ_0 is a constant. This is the form of an outward traveling cylindrical wave. Figure B.2 shows the geometrical significance of this derivation. Notice that u is the

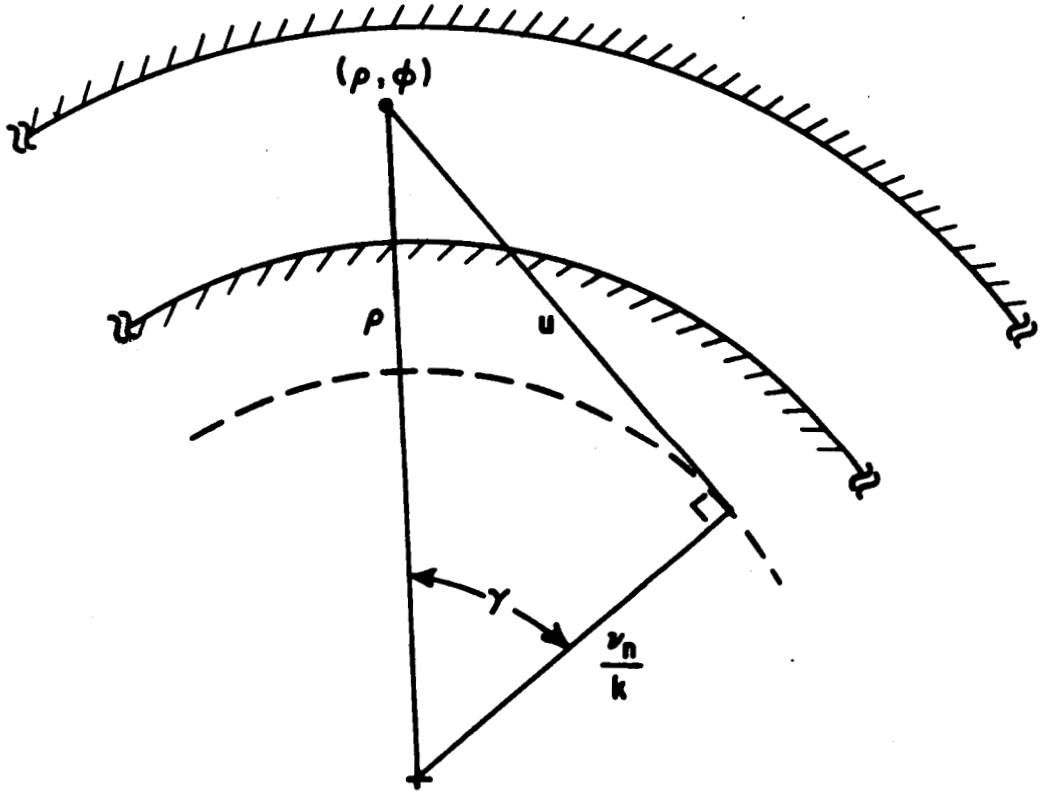

Figure B.2: Geometrical significance of the asymptotic form of the modes in an annular waveguide.

distance from a concentric caustic of radius ν_n/k and γ is the angular displacement from this caustic. The $H^{(1)}_{\nu_n}$ term is handled the same way,

$$H^{(1)}_{\nu}(x) \approx \sqrt{\frac{-j2}{\pi x \sin\gamma}} e^{j(x\sin\gamma - \nu\gamma)} \tag{B.27}$$

$$H^{(1)}_{\nu_n}(k\rho)e^{-j\nu_n\phi} \approx \sqrt{\frac{-j2}{\pi k u}} e^{j(ku+\nu_n\phi_0)} \tag{B.28}$$

which is the form of the corresponding inward traveling (convergent) cylindrical wave.

Figure B.3 illustrates the modal ray form of the modes of the annular waveguide. It consists of crossing cylindrical waves which share a concentric caustic of radius ν_n/k. The angles the rays make with the walls of the guide are obtained easily from the ray-optic geometry,

$$\theta_{an} = \cos^{-1}(\frac{\nu_n}{ka}) \tag{B.29}$$

$$\theta_{bn} = \cos^{-1}(\frac{\nu_n}{kb}). \tag{B.30}$$

It happens that the modal ray caustic can lie inside the guide, as shown in figure B.4. This special case is referred to as a "Whispering Gallery" (WG) mode []. The significance of this type of mode is that almost all of the power in the mode is confined between the modal caustic and the outer wall of the guide. The propagating portion of the fields never "see" the inner wall (although the modal caustic radius ν_n/k depends on it) because the fields are evanescent between the caustic and the inner wall, as shown in figure B.5.

The TM case is handled similarly, with the boundary condition being $\partial H_z/\partial y$ equal zero on the walls,

$$\vec{H}(\rho,\phi) = \hat{z}H_z(\rho,\phi) \tag{B.31}$$

$$(\nabla^2 + k^2)\vec{H}(\rho,\phi) = \left[\frac{1}{\rho}\frac{\partial}{\partial\rho}(\rho\frac{\partial}{\partial\rho}) + \frac{1}{\rho^2}\frac{\partial^2}{\partial\phi^2} + k^2\right] H_z(\rho,\phi)$$

$$= 0 \tag{B.32}$$

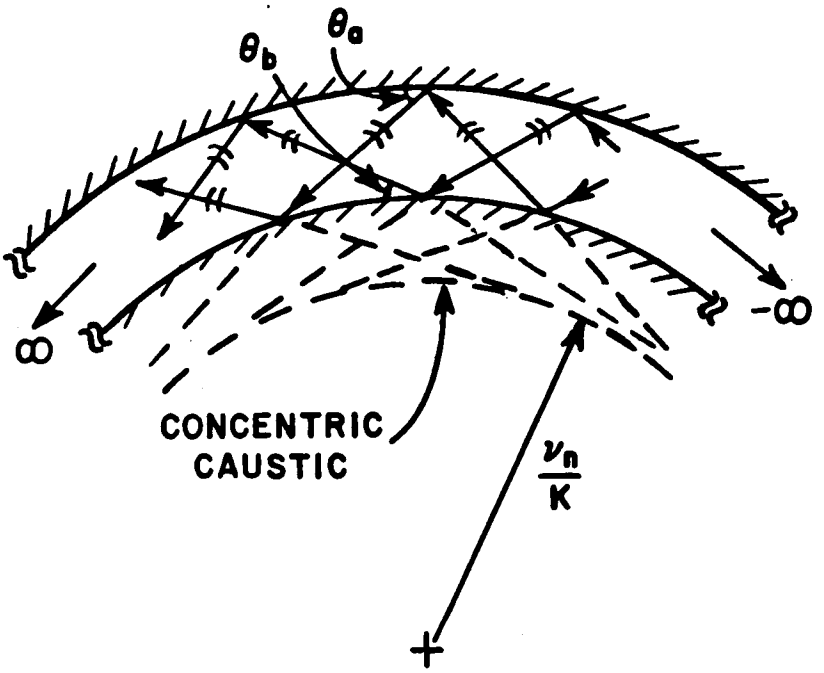

Figure B.3: Modal rays of the annular waveguide.

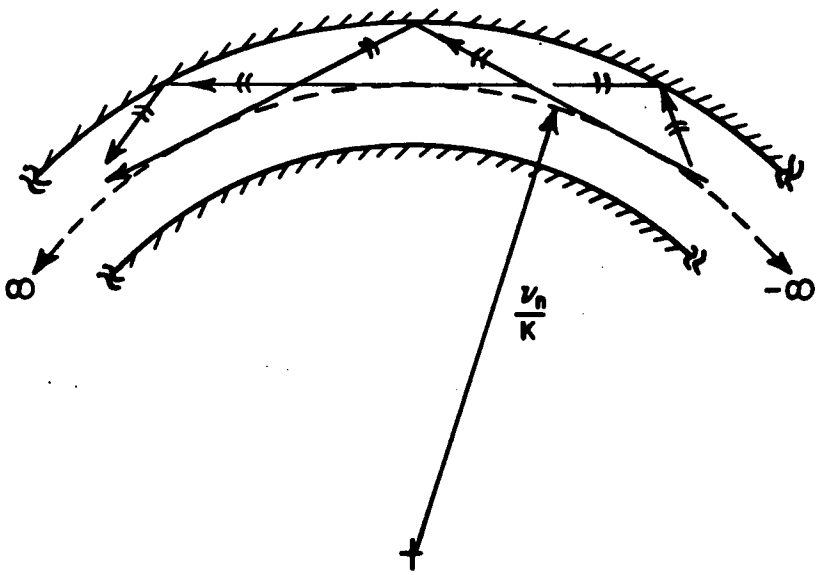

Figure B.4: Whispering gallery modal rays of the annular waveguide.

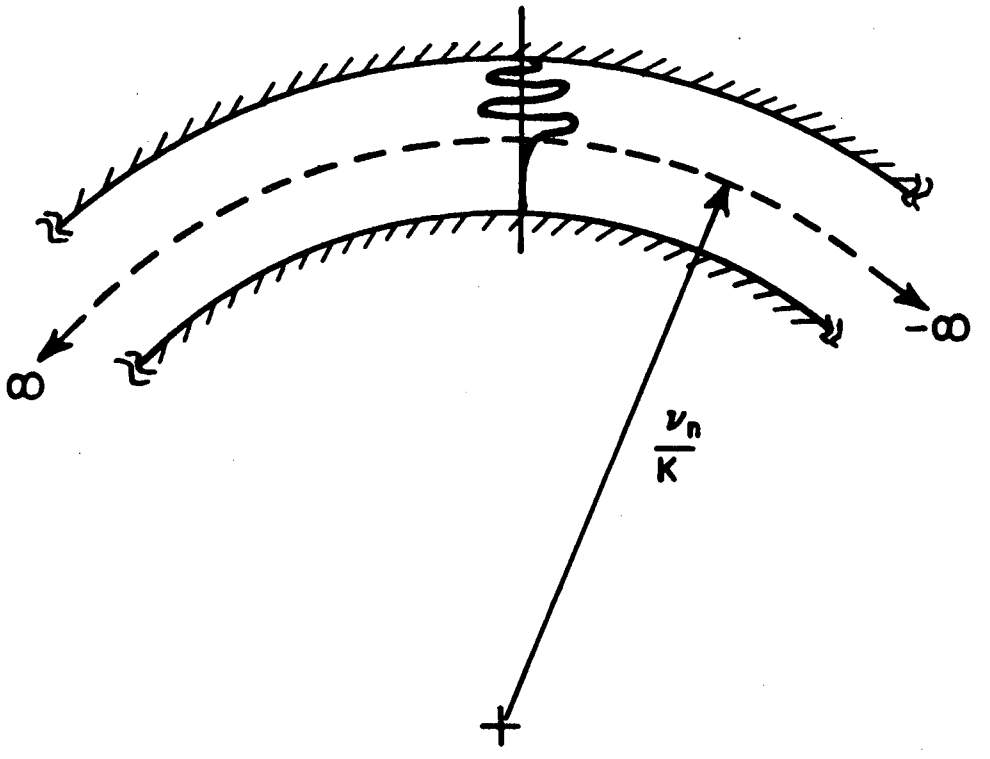

Figure B.5: Field of a whispering gallery mode.

$$\vec{H}(\rho,\phi) = \sum_{n=1}^{\infty}\left[B_n^+\hat{h}_n(\rho)e^{-j\nu_n\phi} + B_n^-\hat{h}_n(\rho)e^{j\nu_n\phi}\right] \tag{B.33}$$

$$\hat{h}_n(\rho) = \hat{z}A_nR_n(k\rho) \tag{B.34}$$

$$R_n(k\rho) = \frac{1}{2j}\left[H_{\nu_n}^{(2)\prime}(kb)H_{\nu n}^{(1)}(k\rho) - H_{\nu_n}^{(1)\prime}(kb)H_{\nu_n}^{(2)}(k\rho)\right] \tag{B.35}$$

$$R_n'(ka) = 0 \tag{B.36}$$

$$\nabla\times\vec{H}(\rho,\phi) = j\omega\varepsilon\vec{E}(\rho,\phi) \tag{B.37}$$

$$\omega\varepsilon = \frac{k}{Z_0} \tag{B.38}$$

$$\vec{E}(\rho,\phi) = -\frac{Z_0}{jk}\left(-\hat{\rho}\frac{1}{\rho}\frac{\partial}{\partial\phi} - \hat{\phi}\frac{\partial}{\partial\rho}\right)H_z(\rho,\phi)$$

$$= \sum_{n=1}^{\infty}\left[B_n^+\hat{e}_n^+(\rho)e^{-j\nu_n\phi} + B_n^-\hat{e}_n^-(\rho)e^{j\nu_n\phi}\right] \tag{B.39}$$

$$\hat{e}_n^{\pm}(\rho) = A_nZ_0\left[\mp\hat{\rho}\frac{\nu_n}{k\rho}R_n(k\rho) - \hat{\phi}jR_n'(k\rho)\right] \tag{B.40}$$

$$A_n = \left[\frac{\nu_n}{kY_0}\int_{kb}^{ka}R_n^2(u)\frac{du}{u}\right]^{-\frac{1}{2}}. \tag{B.41}$$

Notice that the eigenvalues ν_n for this case are found from the transcendental equation (B.36). The ray optical form for the TM case is the same as the TE case with the appropriate change of constants.

C. Diffraction Coefficients

The two types of diffraction effects considered in this report are from a wedge and from a discontinuity in curvature. The geometry for the wedge diffraction coefficient is shown in Figure C.1. The non-uniform GTD diffraction coefficient (Keller's form) is given by [6]

$$D_{s,h}(\phi,\phi') = \frac{\sin\frac{\pi}{n}}{n\sqrt{j2\pi k}}\left[\frac{1}{\cos\frac{\pi}{n}-\cos(\frac{\phi-\phi'}{n})}+R_{s,h}\frac{1}{\cos\frac{\pi}{n}-\cos(\frac{\phi+\phi'}{n})}\right] \quad \text{(C.1)}$$

$$n = 2-\frac{WA}{\pi} \quad \text{(C.2)}$$

where "s" designates the "soft" (TE) case and "h" designates the "hard" (TM) case and $R_{s,h}$ is the appropriate plane wave reflection coefficient for the surface. For a perfectly conducting surface, R_s is -1 and R_h is 1. For an absorber coated surface, $R_{s,h}$ is given by equations (4.44) and (4.48) where $\Gamma_{s,h}$ is $R_{s,h}$.

The geometry for the diffraction coefficient of a discontinuity in curvature is shown in Figure C.2. The non-uniform GTD diffraction coefficient is given by [7]

$$D_{s,h}(\phi,\phi') = \frac{a_2-a_1}{k\sqrt{j2\pi k}}\left[\frac{1+\cos(\phi+\phi')}{(\cos\phi+\cos\phi')^3}+R_{s,h}\frac{1+\cos(\phi-\phi')}{(\cos\phi+\cos\phi')^3}\right]. \quad \text{(C.3)}$$

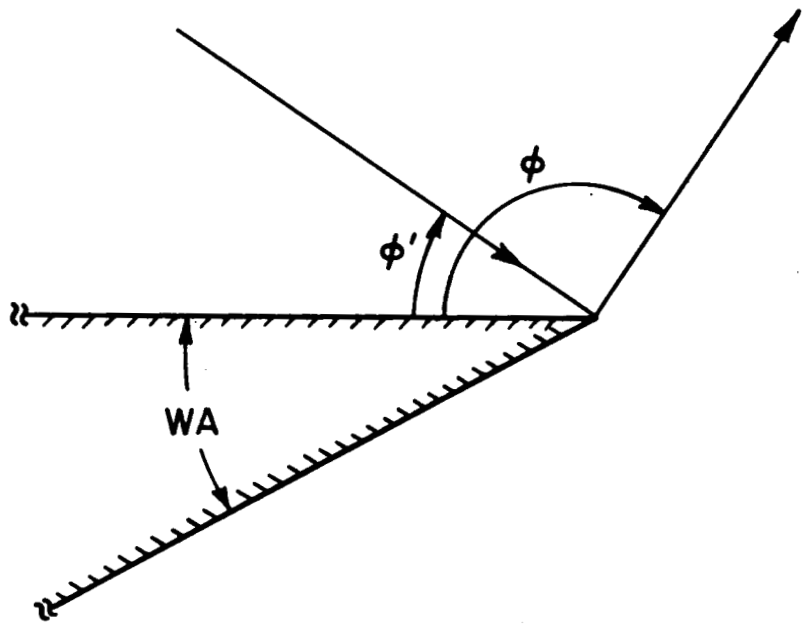

Figure C.1: Wedge diffraction geometry.

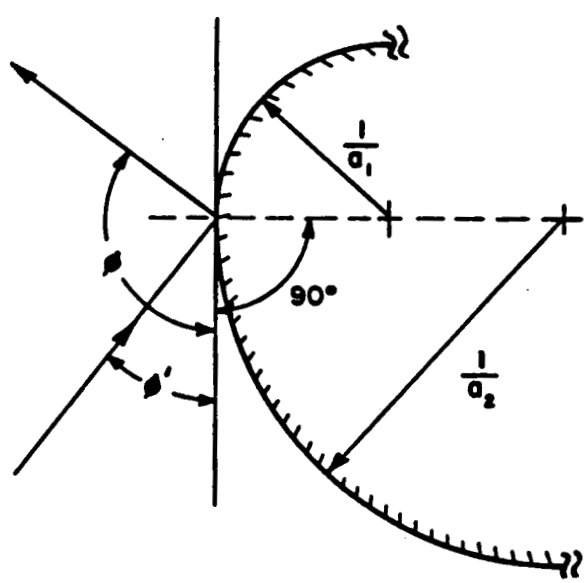

Figure C.2: Discontinuity in curvature diffraction geometry.

D. Symmetry Relations of Matrices

Refering to Figure D.1, it is seen that some of the junction matrices are equal due to symmetry. These relations are as follows,

$$[R_{32}] = [R_{12}] \tag{D.1}$$

$$[R_{23}] = [R_{21}] \tag{D.2}$$

$$[R_{54}] = [R_{34}] \tag{D.3}$$

$$[R_{45}] = [R_{43}] \tag{D.4}$$

$$[T_{23}] = [T_{21}] \tag{D.5}$$

$$[T_{32}] = [T_{12}] \tag{D.6}$$

There is a reversal of coordinate systems at the junction between sections 3 and 4. Therefore, $[T_{45}] \neq [T_{43}]$ and $[T_{54}] \neq [T_{34}]$ contrary to the symmetry relations of (D.5) and (D.6) for the other two junctions. However, it can be shown that there is a simple relationship between the elements of the matrices $[T_{34}]$ and $[T_{54}]$. For the TE case it is given by

$$T_{34}^{mn} = -(-1)^n T_{54}^{mn} \tag{D.7}$$

and for the TM case by

$$T_{34}^{mn} = (-1)^n T_{54}^{mn} \tag{D.8}$$

where T_{pq}^{mn} is the mn^{th} element of matrix $[T_{pq}]$.

As shown in section 3.2.1, the two transmission matrices at a junction are reciprocal,

$$[T_{21}] = [T_{12}]^T \tag{D.9}$$

$$[T_{32}] = [T_{23}]^T \tag{D.10}$$

$$[T_{43}] = [T_{34}]^T \tag{D.11}$$

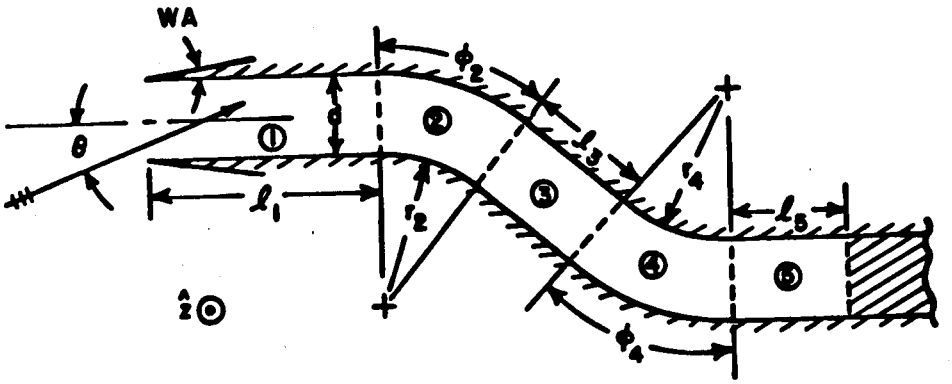

Figure D.1: Geometry of the S-shaped inlet.

$$[T_{54}] = [T_{45}]^T. \tag{D.12}$$

With these simplifications, only six of the original sixteen junction matrices need to be evaluated explicitly. They are $[R_{12}]$, $[R_{21}]$, $[R_{34}]$, $[R_{43}]$, $[T_{12}]$, and $[T_{54}]$. If the inner radii of the curved sections are equal, i.e., $r_2 = r_4$, then

$$[R_{34}] = [R_{12}] \tag{D.13}$$

$$[R_{43}] = [R_{21}] \tag{D.14}$$

$$[T_{54}] = [T_{12}] \tag{D.15}$$

leaving only $[R_{12}]$, $[R_{21}]$, and $[T_{12}]$ to be evaluated.

E. Aperture Integration

Figure E.1 shows the relevant geometry for the Aperture Integration (AI). The aperture field is replaced by equivalent Kirchhoff electric and/or magnetic surface currents which radiate a far field pattern.

For the TE case, the E-field is found from the electric and magnetic vector potentials $\vec{F}$ and $\vec{A}$ respectively, as [9]

$$\vec{E}(\rho,\theta) = -\nabla \times \vec{F}(\rho,\theta) - jkZ_0\vec{A}(\rho,\theta) + \frac{1}{jkY_0}\nabla\left[\nabla \cdot \vec{A}(\rho,\theta)\right] \tag{E.1}$$

where

$$\vec{F}(\rho,\theta) = \frac{e^{-jk\rho}}{\sqrt{j8\pi k\rho}}\int_0^d \vec{M}(y)e^{-jky\sin\theta}dy \tag{E.2}$$

$$\vec{A}(\rho,\theta) = \frac{e^{-jk\rho}}{\sqrt{j8\pi k\rho}}\int_0^d \vec{J}(y)e^{-jky\sin\theta}dy. \tag{E.3}$$

Z_0 is free space impedance and $Y_0 = 1/Z_0$ is free space admittance. The equivalent surface currents for the TE case are given by

$$\begin{aligned}\vec{M}(y) &= \vec{E}^{ap}(y) \times (-\hat{x}) \\ &= \hat{z}E_z^{ap}(y) \times (-\hat{x}) \\ &= -\hat{y}E_z^{ap}(y) \qquad \text{(E.4)}\\ \vec{J}(y) &= -\hat{x} \times \vec{H}^{ap}(y) \\ &= -\hat{x} \times \left[\hat{x}H_x^{ap}(y) + \hat{y}H_y^{ap}(y)\right] \\ &= -\hat{z}H_y^{ap}(y). \qquad \text{(E.5)}\end{aligned}$$

Substituting (E.2), (E.3), (E.4) and (E.5) into (E.1), doing the vector operations and keeping only the terms of order $1/\sqrt{\rho}$ gives the final AI formulation for the TE case as

$$\vec{E}(\rho,\theta) = \hat{z}\sqrt{\frac{jk}{8\pi}}\frac{e^{-jk\rho}}{\sqrt{\rho}}\int_0^d \left[\cos\theta E_z^{ap}(y) + Z_0H_y^{ap}(y)\right]e^{-jky\sin\theta}dy. \tag{E.6}$$

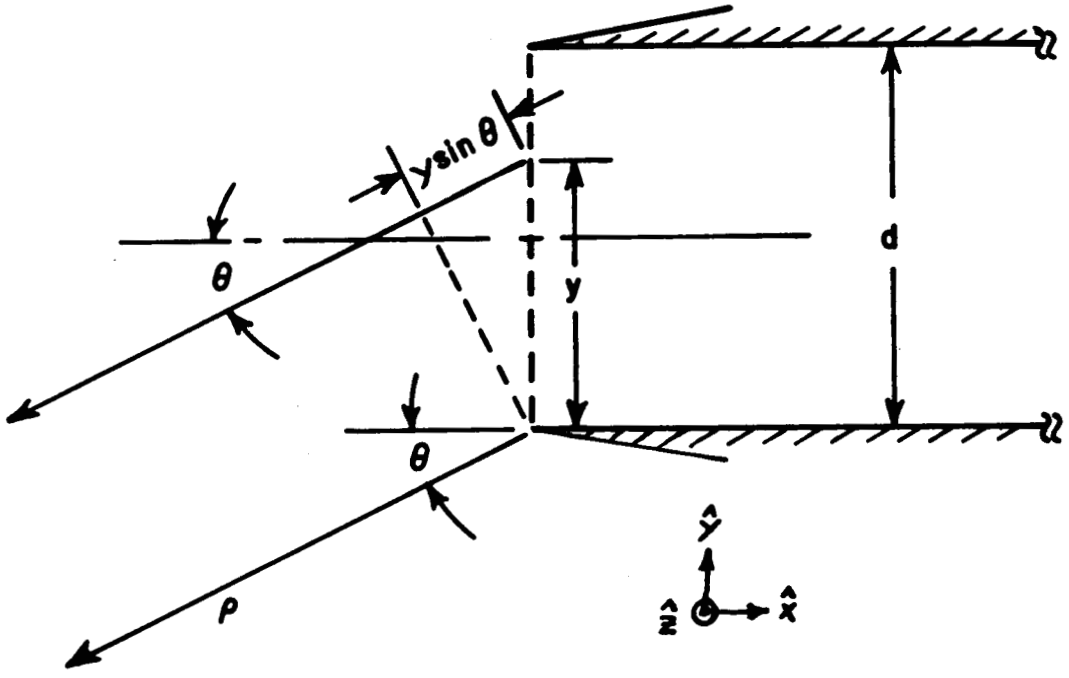

Figure E.1: Geometry for Aperture Integration

The TM case is found analogously as follows:

$$\vec{H}(\rho,\theta) = \nabla \times \vec{A}(\rho,\theta) - jkY_0\vec{F}(\rho,\theta) + \frac{1}{jkZ_0}\nabla\left[\nabla\cdot\vec{F}(\rho,\theta)\right] \tag{E.7}$$

$$\vec{F}(\rho,\theta) = \frac{e^{-jk\rho}}{\sqrt{j8\pi k\rho}}\int_0^d \vec{M}(y)e^{-jky\sin\theta}dy \tag{E.8}$$

$$\vec{A}(\rho,\theta) = \frac{e^{-jk\rho}}{\sqrt{j8\pi k\rho}}\int_0^d \vec{J}(y)e^{-jky\sin\theta}dy \tag{E.9}$$

$$\begin{aligned}\vec{J}(y) &= -\hat{x}\times\vec{H}^{ap}(y)\\ &= -\hat{x}\times\hat{z}H_z^{ap}(y)\\ &= \hat{y}H_z^{ap}(y)\end{aligned} \tag{E.10}$$

$$\begin{aligned}\vec{M}(y) &= \vec{E}^{ap}(y)\times(-\hat{x})\\ &= \left[\hat{x}E_x^{ap}(y)+\hat{y}E_y^{ap}(y)\right]\times(-\hat{x})\\ &= \hat{z}E_y^{ap}(y)\end{aligned} \tag{E.11}$$

$$\vec{H}(\rho,\theta) = \hat{z}\sqrt{\frac{jk}{8\pi}}\frac{e^{-jk\rho}}{\sqrt{\rho}}\int_0^d\left[\cos\theta H_z^{ap}(y) - Y_0E_y^{ap}(y)\right]e^{-jky\sin\theta}dy. \tag{E.12}$$

Bibliography

[1] A. Altintas, P.H. Pathak, W.D. Burnside, "Electromagnetic Scattering from a Class of Open-Ended Waveguide Discontinuities," Technical Report 716148-9, NASA/Langley Research Center, Hampton,VA, Grant No. NSG 1613, Mar '86.

[2] R. Mittra, S.W. Lee, Analytical Techniques in the Theory of Guided Waves, The Macmillan Company, New York, 1971.

[3] P. Ya Ufimtsev, "Method of Edge Waves in the Physical Theory of Diffraction," (from the Russian "Method Krayevykh voin v frizicheskoy teorii diffraksii," Izd-Vo Sov. Radio, pp. 1-243, 1962), translation prepared by the U.S. Air Force Foreign Technology Division, Wright-Patterson AFB, Ohio; released for public distribution, Sept. 7, 1971.

[4] P.H. Pathak, C.W. Chuang, and M.C. Liang, "Inlet Modeling Studies," Technical Report 717674-1, The Ohio State University, ElectroScience Laboratory, prepared under contract No. N60530-85-C-0249 for Naval Weapons Center, China Lake, CA, October 1986.

[5] P.H. Pathak, "Techniques for High Frequency Problems," Chapter 4 in Handbook of Antenna Theory and Design, eds. Y.T. Lo and S.W. Lee, to be published by Van Nostrand Rheinhold.

[6] J.B. Keller, "Geometrical Theory of Diffraction," J. Opt. Soc. Am., Vol.52, pp. 116-130, 1962.

[7] T.B.A. Senior, "The Diffraction Matrix for a Discontinuity in Curvature," IEEE AP, Vol. AP-20, No. 3, pp. 326-333, May 1972.

[8] P.H. Pathak, R.G. Rojas, "UTD Analysis of the EM Diffraction by an Impedance Discontinuity in a Planar Surface," Journal of Wave-Material Interaction, January 1986.

[9] R.F. Harrington, Time Harmonic Electromagnetic Fields, McGraw Hill, New York, 1961.

[10] R.J. Burkholder, P.H. Pathak, "Electromagnetic Fields Backscattered from an S-shaped Inlet Cavity," Technical Report 716611-4, The Ohio State University, ElectroScience Laboratory, prepared under contract No. F33615-84-k-1550 for USAF/AFSC, ASD, Wright-Patterson AFB, Ohio 45633, July 1987.

[11] R.J. Burkholder, "Backscatter Analysis of Two Conducting Inlets," Master's thesis, The Ohio State University, Department of Electrical Engineering, Columbus, Ohio, August 1985.

[12] N.H. Myung, P.H. Pathak, "A High Frequency Analysis of Electromagnetic Plane Wave Scattering by Perfectly Conducting Semi-Infinite Parallel Plate and Rectangular Waveguides with Absorber coated Inner Walls," Technical Report 715723-1, The Ohio State University ElectroScience Laboratory, prepared under Grant NAG 3-476, for NASA/Lewis Research Center, Cleveland, Ohio, September 1986.